8-6-2007

Semiconductor Quantum Structures for Ultraviolet-to-Infrared Multi-Band Radiation Detection

Gamini Ariyawansa

SEMICONDUCTOR QUANTUM STRUCTURES for ULTRAVIOLET-to-INFRARED MULTI-BAND RADIATION DETECTION

by

GAMINI ARIYAWANSA

Under the direction of Unil Perera

ABSTRACT

In this work, multi-band (multi-color) detector structures considering different semiconductor device concepts and architectures are presented. Results on detectors operating in ultraviolet-to-infrared regions (UV-to-IR) are discussed. Multi-band detectors are based on quantum dot (QD) structures; which include quantum-dots-in-a-well (DWELL), tunneling quantum dot infrared photodetectors (T-QDIPs), and bi-layer quantum dot infrared photodetectors (Bi-QDIPs); and homo-/heterojunction interfacial workfunction internal photoemission (HIWIP/HEIWIP) structures. QD-based detectors show multi-color characteristics in mid- and far-infrared (MIR/FIR) regions, where as HIWIP/HEIWIP detectors show responses in UV or near-infrared (NIR) regions, and MIR-to-FIR regions.

In DWELL structures, InAs QDs are placed in an InGaAs/GaAs quantum well (QW) to introduce photon induced electronic transitions from energy states in the QD to that in QW, leading to multi-color response peaks. One of the DWELL detectors shows response peaks at ~ 6.25 μm, ~ 10.5 μm and ~ 23.3 μm. In T-QDIP structures, photoexcited carriers are selectively collected from InGaAs QDs through resonant tunneling, while the dark current is blocked using AlGaAs/InGaAsAlGaAs/ blocking barriers placed in the

structure. A two-color T-QDIP with photoresponse peaks at 6 and 17 μm operating at room temperature and a 6 THz detector operating at 150 K are presented. Bi-QDIPs consist of two layers of InAs QDs with different QD sizes. The detector exhibits three distinct peaks at 5.6, 8.0, and 23.0 μm.

A typical HIWIP/HEIWIP detector structure consists of a single (or series of) doped emitter(s) and undoped barrier(s), which are placed between two highly doped contact layers. The dual-band response arises from interband transitions of carriers in the undoped barrier and intraband transitions in the doped emitter. Two HIWIP detectors, p-GaAs/GaAs and p-Si/Si, showing interband responses with wavelength thresholds at 0.82 and 1.05 μm, and intraband responses with zero response thresholds at 70 and 32 μm, respectively, are presented. HEIWIP detectors based on n-GaN/AlGaN show an interband response in the UV region and intraband response in the 2-14 μm region. A GaN/AlGaN detector structure consisting of three electrical contacts for separate UV and IR active regions is proposed for simultaneous measurements of the two components of the photocurrent generated by UV and IR radiation.

INDEX WORDS: Infrared Detectors, Multi-Color Detectors, Multi-Spectral, Dual-Band, Ultraviolet Detectors, Terahertz Detectors, Quantum Dot, Quantum Well, Resonant Tunneling, Double-Barrier, Dark Current Blocking, III-V Material, InAs, InGaAs, InAlAs, GaAs, AlGaAs, GaN, AlGaN, Si, Homojunction, Heterojunction, Workfunction, Photoemission, Impurity States.

SEMICONDUCTOR QUANTUM STRUCTURES for ULTRAVIOLET-to-INFRARED MULTI-BAND RADIATION DETECTION

by

Gamini Ariyawansa

A Dissertation Submitted in Partial Fulfillment of the Requirements for the Degree of

Doctor of Philosophy

in the College of Arts and Sciences

Georgia State University

2007

SEMICONDUCTOR QUANTUM STRUCTURES for ULTRAVIOLET-to-INFRARED MULTI-BAND RADIATION DETECTION

by

Gamini Ariyawansa

Major Professor: Dr. Unil Perera

Committee: Dr. Vadym Apalkov

Dr. Nikolaus Dietz

Dr. Douglas Gies

Dr. Brian Thoms

Electronic Version Approved:

Office of Graduate Studies

College of Arts and Sciences

Georgia State University

August 2007

To my parents, grandmother, sisters,

daughter, and of course, my wife.

Acknowledgments

I would like to express my deep and sincere gratitude to my advisor, Prof. Unil Perera, for his advisement, guidance, and support throughout this work. With his inspiration and enthusiasm, he led me to make this a success. He offered me exceptional insight and prepared me for future challenges. The professional research skills and personal lessons that I have learnt from him are invaluable for future endeavors. I would like to thank the other members of my committee: Dr. Brian Thoms, Dr. Nikolaus Dietz, Dr. Vadym Apalkov, and Dr. Douglas Gies for fruitful discussions, technical assistance, and effort in reading and providing me with valuable comments on this thesis. I convey special acknowledgement to Dr. Steven Matsik, who was always open for questions and discussions relating to research, and I thank him for his scientific advice. I must thank one of our former members in the group Dr. Mohamed Rinzan for valuable discussions on the subject matter and technical assistance.

Among the many collaborators who contributed towards the research, I would like to acknowledge Prof. Pallab Bhattacharya at University of Michigan, Prof. Sanjay Krishna at University of New Mexico, Dr. H. C. Liu at NRC Canada, and Prof. Ian Ferguson at Georgia Institute of Technology. I would also like to thank past and present colleagues in the group: Dr. Dmitriy Esaev, Dr. Hu Zhigao, Dr. Satyabrata Jit, Aruna Weerasekara, Mustafa Alevli, Viraj Jayaweera, Ranga Jayasinghe, and Laura Byrum. I wish to thank all the individuals of the Department of Physics and Astronomy including the Physics Workshop, and my colleagues and friends for their contribution, friendship, and love.

Finally, I would like to thank my wife Manori for her unconditional love, support,

and patience throughout my academic carrier. Her dedication and courage enabled this work. I express my deepet gratitude to my mother, late father, and late grandmother for their love, support, and confidence in me. I am also thankful to my little daughter Methni, a continuing source of happiness in my life.

Table of Contents

List of Tables

List of Figures

Acronyms

2D two dimensional

3D three dimensional

Be berillium

BIB blocked-impurity-band

Bi-QDIP bi-layer quantum dot infrared photodetector

BLIP background limited infrared performance

C carbon

CB conduction band

C-V-T capacitance voltage temperature

D* detectivity

DWELL quantum dots-in-a-well

FIR far infrared (30-100 μm)

FOV field of view

FPA focal plane array

FTIR Fourier Transform Infrared

g photoconductive gain

Ga gallium

Ge germanium

HEIWIP Homojunction Interfacial Workfunction Internal Photoemission

IR infrared

I-V-T current voltage temperature

IWIP Interfacial Workfunction Internal Photoemission

HIWIP Heterojunction Interfacial Workfunction Internal Photoemission

λ_0 threshold wavelength

LWIR long-wavelength infrared (5-14 μm)

MBE molecular beam epitaxy

MCT mercury cadmium telluride

MIR mid infrared (5-30μm)

ML monolayer

MWIR mid-wavelength infrared (3-5 μm)

NIR near infrared (0.8-5 μm)

OMCVD OrganoMetallic Chemical Vapor Deposition

QD quantum dot

QDIP quantum dot infrared photodetector

η quantum efficiency

QW quantum well

QWIP quantum well infrared photodetector

RCA resonant cavity architecture

SI semi-insulating

Si silicon

SIMS Secondary Ion Mass Spectroscopy

SWIR short-wavelength infrared (1-3 μm)

T operating temperature

THz terahertz (1-3 THz)

T-QDIP tunneling quantum dot infrared photodetector

UV ultraviolet

VB valence band

VIS visible

VLWIR very-long-wavelength infrared (14-30 μm)

Chapter 1

Introduction

The rapid development of infrared (IR) detector technology, which primarily includes device physics, semiconductor material growth and characterization, and microelectronics, has led to new concepts like target recognition and tracking systems.[1, 2] Among these concepts, multi-band radiation detection is being developed as an important tool to be employed in many practical applications. Detecting an object's infrared emission at multiple wavelengths can be used to eliminate background effects,[3] and reconstruct the object's absolute temperature[4] and unique features. This plays an important role in differentiating and identifying an object from its background. However, measuring multiple wavelength bands typically requires either multiple detectors or a single broad-band detector with a filter wheel coupled to it in order to filter incident radiation from different wavelength regions. Both of these techniques are associated with complicated detector assemblies, separate cooling systems, electronic components, and optical elements such as lenses, filters, and beam splitters. Consequently, such sensor systems (or imaging systems) involve fine optical alignments, which in turn require a sophisticated control mechanism hardware. These

complications naturally increase the cost and the load of the sensor system, a problem which can be overcome by a single detector responding in multiple bands. The multi-spectral features obtained with multi-band detectors are processed using color fusion algorithms[1] in order to extract signatures of the object with a maximum contrast. With the development of multi-band detector systems, there is an increased research[1, 5] effort to develop image fusion techniques. Fay et al.[1] have reported a color-fusion technique using a multi-sensor imagery system, which assembled four separate detectors operating in different wavelength regions. The major goal of my study is to investigate multi-band detection concepts and develop high performance multi-band detectors.

At present, there are many applications where multi-band detectors are required. In land-mine detection[3] the number of false positives can be reduced using multi-spectral approaches, allowing the the identification of real land-mine sites. Military applications include the use of multi-band detectors to detect muzzle flashes, which emit radiation in different wavelength regions,[6] to locate the position of enemy troops and operating combat vehicles. Multi-band focal plane arrays (FPAs) responding in very-long-wavelength infrared (VLWIR) region (14-30 μm) can be used for space surveillance and space situational awareness,[2] where observations of extremely faint objects against a dark background are required. Present missile-warning sensors are built focusing on the detection of ultraviolet (UV) emission by missile plume. However, with modern missiles, attempting to detect the plume is impractical due to its low UV emission. As a solution, IR emission[7] of the plume can be used instead of UV. Then the detector system should be able to distinguish the missile plume against its complex background, avoiding possible false-alarms.

Thus, a single band detector would not be a choice to achieve this. Using a two-color (or multi-color) detector, which operates in two IR bands where the missile plume emits radiation, the contrast between the missile plume and the background can be maximized. Moreover, a multi-band detector can be used as a remote thermometer[4] where the object's radiation emission in the two wavelength bands is detected by a multi-band detector and the resulting two components of the photocurrent can be solved to extract the object's temperature.

In addition to multi-band detector development, this study focused also on the investigation of terahertz detectors. The use of terahertz radiation as a tool for characterization of materials has been widely demonstrated. Applications can be found in various fields such as medicine, industry, security, astronomy, and atmospheric studies. Some examples include cancer/tumor detection, non-destructive testing[8], toxic/chemical detection, and gas sensing. The key advantage of terahertz radiation in these areas is the ability to penetrate and distinguish between different non-metallic materials. The terahertz range is especially useful in gas sensing. A terahertz detector can be coupled with a laser tuned to the frequency of the absorption line of the gas to be detected (fingerprint of the gas). The fingerprints of a large number of gases fall in the range of 0.5-3 THz.

In this dissertation, multi-band detectors were investigated based on three Quantum Dot (QD) based device structures: (i) Quantum Dots-in-a-Well (DWELL), (ii) Tunneling Quantum Dot Infrared Photodetector (T-QDIP), and (iii) Bi-Layer Quantum Dot Photodetector (Bi-QDIP); and dual-band detectors were developed based on Homo-Heterojunction Interfacial Workfunction Internal Photoemission (HIWIP/HEIWIP) detector structures. In

Chapters 2, 3, and 4, QD-based detector structures are presented discussing device design aspects and figures of merit of the detectors. A characteristic feature of any quantum dot infrared photodetector (QDIP), where the quantum dots (QDs) have a well controlled size distribution, is that they result in narrow spectral response peaks. The detection mechanism is based on intersubband transitions of carriers between the energy states in the structure. Depending on the design, there can be more than one bound state in the system. As a result, QDIPs can yield several response peaks, which can then be called a "multi-color" detector. In Chapter 2, three-color DWELL detectors having different well widths are presented. Three DWELL detectors (1388, 1373, and 1299) with different quantum well (QW) widths have been characterized, showing response peaks at three distinct wavelengths in mid-wavelength infrared (MWIR), long-wavelength infrared (LWIR), and VLWIR regions. For example, the detector 1388 has peak wavelengths at 6.25, 10.5, and 23.3 μm. The operating wavelength of these detectors in the short wavelength region can be tailored by changing the width of the QW. Results on a two-color T-QDIP with photoresponse peaks at 6 and 17 μm operating at room temperature, and a terahertz T-QDIP responding at 6 THz (50 μm) and operating up to 150 K are presented in Chapter 3. A Bi-QDIP detector structure, in which there are two sizes of quantum dots, is presented in Chapter 4. Each QD layer in Bi-QDIP structure yields one or two response peaks, showing multi-color detection.

Dual-band HIWIP structures based on GaAs and Si material systems, which respond in the NIR and far infrared (FIR) regions, are discussed in Chapter 5. A typical HIWIP/HEIWIP detector structure consists of a single (or series of) doped emitter(s) followed by an undoped barrier(s) between two highly doped contact layers. The primary difference

between HIWIP and HEIWIP comes in the emitter and barrier material. HIWIPs have the same material in the emitter and the barrier, while HEIWIPs have materials with different bandgaps in the emitter and the barrier. In Chapter 6, HEIWIP UV/IR dual-band detector structures with n-doped GaN emitters and undoped $Al_xGa_{1-x}N$ barriers are presented. In both HIWIP and HEIWIP dual-band detectors, there are two detection mechanisms leading to dual-band response: (i) interband (valence-to-conduction) transitions of carriers in the undoped barrier leading to NIR or UV response, and (ii) intraband transitions in the doped emitter resulting in a response in mid infrared (MIR)-to-FIR region. The wavelength threshold of the interband response depends on the band gap of the barrier material, and the MIR/FIR response due to intraband transitions in the emitter can be tailored by adjusting the workfunction in emitter/barrier junction. The p-GaAs/GaAs HIWIP detector has wavelength thresholds in the NIR and FIR regions at 0.82 and 70 μm. For a p-Si/Si HIWIP detector, the NIR and FIR wavelength thresholds were observed at 1.05 and 32 μm, respectively. Preliminary n-GaN/$Al_xGa_{1-x}N$ HIWIP detectors with $x = 0.026$, and 0.1, were successfully demonstrated with a $\sim$ 360 nm threshold UV response at temperatures up to 300 K and 8-14, 3-13 μm IR responses at 80 K. In addition to the photoresponse due to the primary mechanism in the structure, impurity-related response peaks, which are superimposed on the primary response, were also observed. These features are discussed in detail in each chapter.

The predominant drawback of multi-band detectors is their inability to separate the photocurrent components corresponding to different wavelength bands without using external optical filters. Detector structures with multi-stack active regions[9] and bias se-

lective response peaks[10] allow simultaneous measurements of the photocurrent components generated by each detection mechanism without the use of external filters. In order to separate the UV and IR photocurrent components without using external filters and measure the two components simultaneously, a GaN/AlGaN device structure having separate UV and IR active regions with three contacts (one contact specific to each region and one contact common for both regions) is proposed in Chapter 6. In this approach, no significant IR photocurrent from the UV active region or UV photocurrent from the IR active region is expected. Preliminary experimental results are in good agreement with the predicted results.

In addition to the afore mentioned multi-spectral detection and terahertz applications, these detectors are also useful in numerous applications such as night vision, spectroscopy, environmental monitoring, medical diagnostics, battlefield-imaging, space astronomy, and fire detection. In astronomy, where infrared technology plays a dominant role in observing celestial objects, the NIR response of the detector can be used to observe cooler red objects and FIR can detect cold objects such as comets, planets, and interstellar dust.

Chapter 2

Multi-Band Quantum Dots-in-a-Well (DWELL) Infrared Photodetectors

2.1 Introduction

In the field of IR detector technology, quantum dot infrared photodetectors (QDIPs) have attracted the attention of researchers looking to develop infrared optoelectronic devices with improved performance. Compared to quantum well infrared photodetectors (QWIPs), QDIPs have additional degrees of confinement, leading to three major advantages[11]: (i) QDIPs are sensitive to normal-incidence IR radiation, which is forbidden in n-type QWIPs due to polarization selection rules, (ii) QDIPs exhibit long effective carrier lifetime, ∼100's of picoseconds, which has been predicted by theory[12] and confirmed by experiments[13], and (iii) QDIPs exhibit low dark current. Theoretically, QDIPs should show improved performance characteristics such as high responsivity, high detectivity, and high operating temperatures. However, such dramatic improvement in the performance of QDIPs has not

been demonstrated as of yet due to the fact that the detection in most QDIPs is based on bound-to-continuum transitions, as opposed to transitions between the ground-state and the first excited-state in a QD.

QDIPs ranging from single element detectors[14, 15, 16, 17, 18, 19] to FPAs[10, 20, 21] have previously been developed. In addition to the afore mentioned advantages, QDIPs show improved radiation hardness[22, 23] and polarization sensitive spectral responses.[24, 25] QDIPs operating at temperatures above 77 K [26, 27, 28, 29, 30, 15, 31] justify investing in development of uncooled IR imaging systems. In a recent work, Matthews et al.[32] reported extremely long carrier lifetime in a DWELL detector, which also exhibits a photoconductive gain of 10^4-10^5 in the 20-100 K temperature range. In addition to InAs/GaAs (or InGaAs/GaAs) system, QDIPs are developed using SiGe/Si[33, 34, 35] and GaN/AlN[36] material systems. The behaviour of QDs under an applied magnetic field[37, 38] has recently become a point of interest for understanding the physics of QDs as well as future magnetic devices.

In a quantum dots-in-a-well (DWELL) structure, InAs QDs are placed in a thin InGaAs QW, which in turn is positioned in a GaAs matrix[18]. The DWELL heterostructure provides better confinement for carriers trapped in the QD by lowering the ground-state of the QD with respect to the GaAs band edge, resulting in low thermionic emission. There can be one or more confined energy states in the QD, with the position and separation of energy states dependent on the size of the QD as well as the confinement potential. The detection mechanism of a DWELL detector involves the photoexcitation of electrons from the QD ground-state to an excited-state in either the QD or QW. Energy states associated with the QW can be bound, quasi-bound, or part of the continuum. These different possible

transitions lead to the multi-color characteristic in the spectral response of detectors. A schematic diagram of a DWELL conduction band profile is shown in Fig. 2.1, along with different transitions between energy states as indicated by the arrows. The photocurrent, a result of photoexcited carriers, is proportional to the product of the oscillator strength and the carrier escape probability. Escape probability can be increased by applying an external electric field. A response peak resulting from a bound-to-bound transition has a larger oscillator strength and a smaller escape probability than a response peak resulting from a bound-to-continuum transition. Hence, a bound-to-continuum peak can be observed even at low biases, whereas, a bound-to-bound peak dominates at high applied fields due to the enhanced escape probability by field-assisted tunneling. The states in the QD and the QW can be adjusted independently by changing the parameters associated with each. As a result, DWELL structures open up the possibility of different device architecture, leading to optimized multi-band IR detectors.

In this section, three-color InAs/InGaAs DWELL detectors,[39] with different well widths, are discussed. Three DWELL detectors (labeled as 1388, 1373 and 1299) with different well widths (120 Å , 110 Å and 90 Å respectively) were characterized showing response peaks at three distinct wavelengths in the MWIR, LWIR, and VLWIR regions. Detector 1388 has peak wavelengths at ~ 6.25 μm, ~ 10.5 μm and ~ 23.3 μm. All observed peaks correspond to the energy difference of the intersubband transitions in the DWELL heterostructure. The two peaks at 6.25 μm and 10.5 μm are correspond to bound-to-bound transitions from the ground-state in the QD to a state in the QW, whereas the longer wavelength peak (~ 23.3 μm) is due to an intersubband transition between QD levels. The

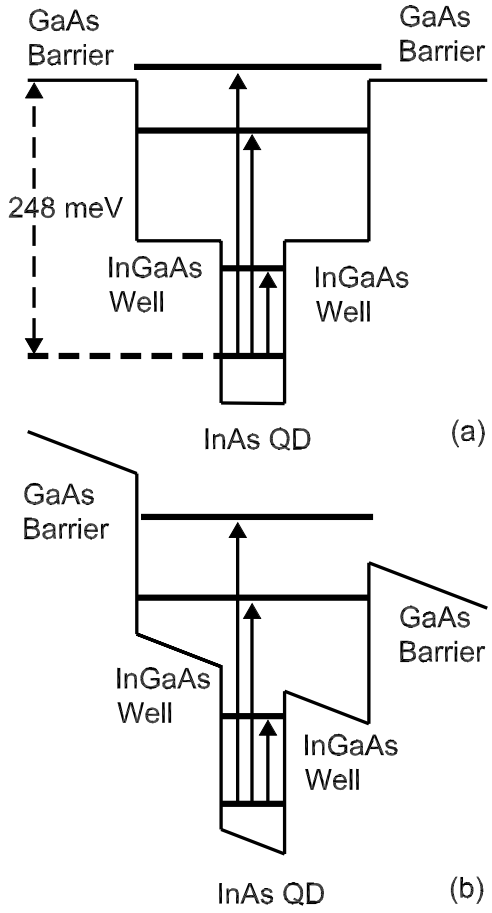

Figure 2.1: IR Conduction band profile of the DWELL structure (a) under zero bias and (b) under a negative bias (top-contact is negative). The energy states corresponding to possible transitions leading to spectral response peaks are indicated by arrows.

23.3 μm peak has a detectivity of 7.9×10^{10} $cm\sqrt{Hz}/W$ at 4.6 K under -2.2 V bias. Spectral response in detector 1388 has been observed up to 80 K. The operating wavelength of these detectors in the MWIR and LWIR regions can be tailored by changing the width of the QW. When the width of the QW is increased, the two peaks in MWIR and LWIR regions show a red-shift, while the VLWIR peak remains around $\sim$ 23.3 μm. This observation confirms the origin of each response peak.

2.2 DWELL Device Structure

The DWELL detectors were grown[40] in a VG-80 solid source molecular beam epitaxy (MBE) system with a cracked As_2 source at the University of New Mexico. The GaAs layers were grown at a substrate temperature T_{sub} = 580 °C, whereas the $In_{0.15}Ga_{0.85}As$ QW and the InAs QDs were grown at T_{sub} = 480 °C as measured by an optical pyrometer. Using standard lithography, metal evaporation and wet etching techniques, $n-i-n$ detector mesas were fabricated for top-side illumination. Mesas with various circular optically active areas (diameter ranging from 25-300 μm) were fabricated to test for leakage current and uniformity. More details of the growth process are described in Ref.[40].

The design for the detector structure 1388 is shown in Fig. 2.2. The QDs were doped n-type with Silicon to a sheet density of 5×10^{11} cm^{-2}, which corresponds to about 1 electron per QD. The QW was not intentionally doped. It has been found[41] that the optimal doping concentration for DWELL detectors, which is the doping when the detector performance is optimum, corresponds to about one electron per QD. The size of the QDs, which is a critical parameter in the detector design, is controlled by the growth conditions,

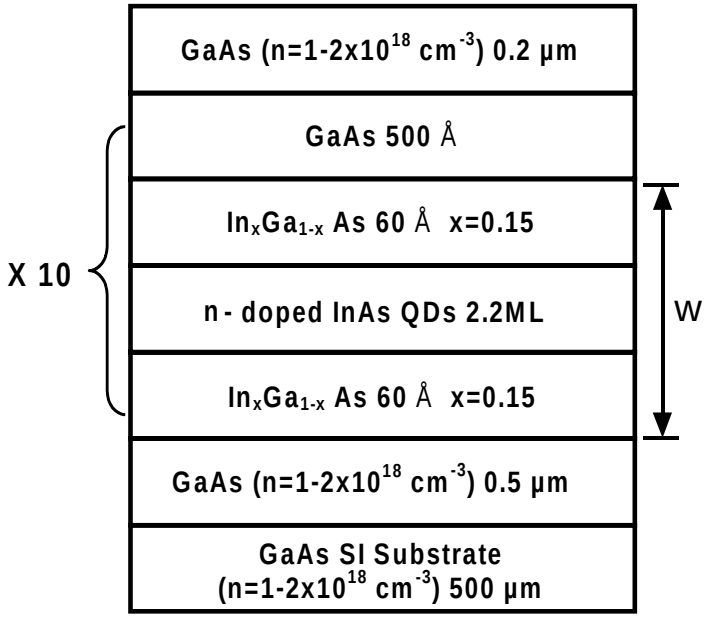

Figure 2.2: Schematics of the dot-in-a-well detector structure. The width of the QW, i.e. the combined thickness of $In_{0.15}Ga_{0.85}As$ layers (indicated as "w" in the figure), is different for each detector. Structures 1299,1373 and 1388 have well widths of 90, 110, and 120 Å respectively, while all other parameters are the same.

especially the temperature and growth rate (controlled by the flow rate). Any inhomogeneous QD size fluctuation would result in a broadening of the corresponding spectral band. There is a 2-D distribution of QDs on a plane perpendicular to the growth direction; the formation of QDs on top of another QD is not possible since there is no barrier to separate two QD layers. The width of the QW, i.e. the combined thickness of $In_{0.15}Ga_{0.85}As$ layers, is denoted by "w". The other two detectors (1373 and 1299) are identical to the 1388 detector except for the width of the QW. In 1373 and 1299 structures, the thickness of the bottom $In_{0.15}Ga_{0.85}As$ layer is 50 Å and 30 Å, while the top $In_{0.15}Ga_{0.85}As$ layer thickness stays the same (60 Å); thus providing 110 and 90 Å well width, respectively. There are ten periods of $In_{0.15}Ga_{0.85}As$/n-InAs/$In_{0.15}Ga_{0.85}As$ in each of the detector structures. Square mesa devices with 400×400 μm dimensions were processed; and a 300 μm diameter opening was left in the top-contact for front-side illumination. Photoluminescence measurements of ground-state transition of the QD (1.25 μm at T = 300 K) with a 60 : 40 conduction to valence band ratio, were used to estimate that the ground-state of the QD is approximately 250 meV below the GaAs band edge. There can be at least two bound states in the QD and one confined state in the QW[19], as shown in Fig. 2.1. Possible transitions of carriers leading to the spectral response peaks are also indicated by arrows. The detectors were processed and contacts were wire-bonded to chip carriers, and the spectral response was obtained for normal incidence radiation using a Perkin Elmer System 2000 Fourier Transform Infrared (FTIR) spectrometer, and calibrated by a reference spectrum obtained with a Si composite bolometer with the same set of optical components. For more details, see Appendix A: Device Characterization.

A model for energy level calculations of a DWELL system is proposed by Amtout et al.[42] DWELL structures with different QDs have been tested experimentally and electronic spectra obtained by the model are in good agreement with the experimental results. Transmission electron microscopy showed pyramidal shaped QDs. The Hamiltonian for a system with a quasi-zero-dimensional QD placed in a two-dimensional QW is defined with a potential energy consisting of four components: the potential energy in the QD region, the potential energy in the QW region, the potential energy in the barrier region, and the potential arising from the applied electric field. The eigenfunctions of the Hamiltonian are derived using a Bessel function expansion. The model was applied to two DWELL detectors. The DWELL detectors have QDs with base dimensions of 110 and 140 Å and heights of 65 and 50 Å, respectively. The spacing between the first and second energy levels obtained from the model are 132 and 150 meV, whereas experimental analysis showed the energy spacing to be 123 and 140 meV, respectively. Although the energy states are shifted by the electrostatic potential from the bias field, the energy spacing between the first two energy states does not change on the applied electric field. This was observed in spectral responsivity of many DWELL detectors.

2.3 Experimental Results and Effects of the Well Width on Response Peaks

In order to understand the DWELL device architecture, electronic spectrum, and photoexcitations leading to response peaks, the three detectors were characterized and results were compared.[39] First, the dark current-voltage (I-V) characteristics of all three

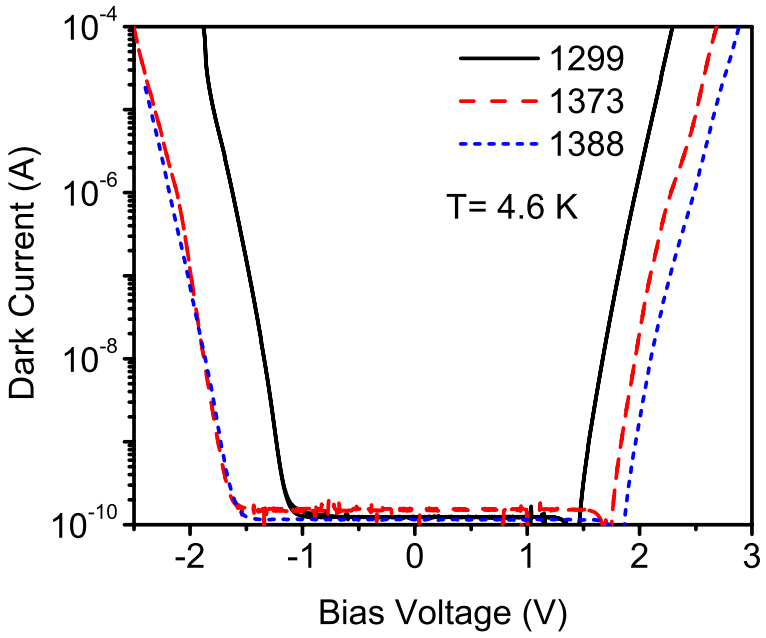

Figure 2.3: A comparison of dark current-voltage (I-V) characteristics of all three structures at 4.6 K. The mesas tested have the same electrical area. The 1388 detector showed the lowest dark current, and a decrease of dark current is observed as the width of the QW increases.

structures were obtained and compared, as shown in Fig. 2.3 (the measurement technique is explained in Appendix A). The 1388 detector shows the lowest dark current, and it increases when the width of the QW increases. All three detectors exhibit three distinct peaks (three colors). The results for 1388 detector under different bias voltages are shown in Fig. 2.4. A band diagram with corresponding transitions, indicated by arrows, is shown in the inset to Fig. 2.4. The origin of each peak is explained in detail in the following sections.

The spectral response of the three detectors in the range 3-15 μm is shown in Fig. 2.5. The two curves presented for each detector correspond to -0.5 V and -1.4 V bias values. All three detectors have two distinct peaks in this wavelength range. The 1299 detector exhibits its first peak at $\sim$4.2 μm and the second peak at $\sim$8.1 μm. A semi-empirical estimate, based on the photoluminescence spectra with a 60:40 split of the bandgap difference, gives the energy separation between the ground-state of the QD and the conduction band edge of GaAs to be 225-250 meV ($\sim$4.9-5.5 μm). Hence, the 4.2 μm peak is probably due to transitions from the ground-state of the QD to the continuum state of the QW and the second peak is due to transitions from the ground-state of the QD to a bound state in the QW as shown in Fig. 2.1. Moreover, it has been shown[43] that the line width ($\triangle\lambda/\lambda$) of a peak due to transitions from bound-to-bound states is narrower than that of transitions from bound-to-continuum states. The line width of the 4.2 μm peak is about 42%, whereas the line width of the 8.1 μm peak is about 28%; and this observation is consistent with the above description. Also, the bound-to-continuum peak (at 4.2 μm) is seen even at low bias values, whereas the bound-to-bound peak (at 8.1 μm) dominates at high bias voltages due to increased escape probability by field assisted tunneling.

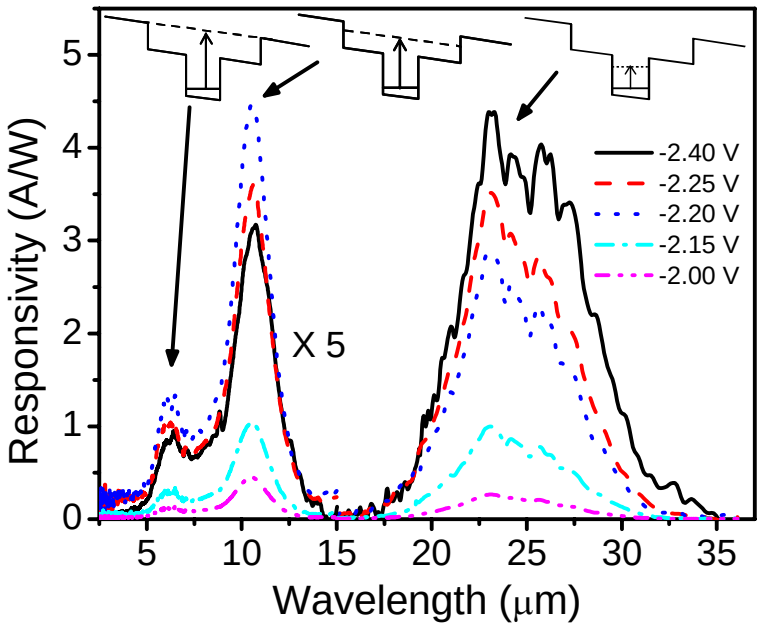

Figure 2.4: Three color response of 1388 detector under different bias voltages at 4.6 K. The band diagram with the corresponding transitions indicated by arrows are shown in the inset.

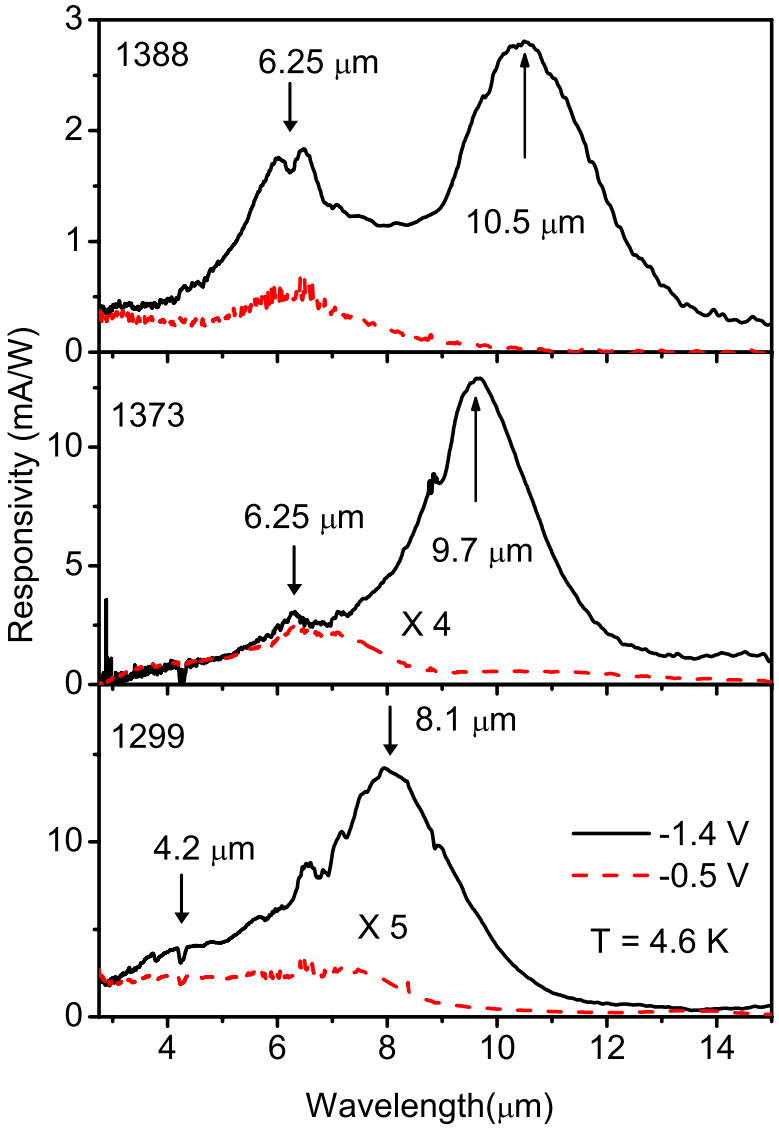

Figure 2.5: The first two peaks of the three detectors biased with -1.4 V and -0.5 V at 4.6 K. Arrows indicate the peak positions and × sign implies that the curve has been multiplied by the number indicated.

When the width of the QW is increased, the energy spacing between the levels in the QW decreases causing a red-shift of the first two peaks. The results for detectors 1299 and 1388 support this idea. The 1388 detector exhibits a quasi-bound state close to the band edge of the GaAs barrier, and hence, the first peak of 1388 is due to transitions from the ground-state of the QD to a quasi-bound state in the QW. This can be confirmed by the red-shift and narrower line width of the first peak of 1388 as compared to the first peak of 1299. Based on width of the QW in detector 1373, its peaks are expected to be located in between the peaks of detectors 1299 and 1388. However, the experiment showed a longer red-shift than expected in both first and second peaks of detector 1373 with respect to detector 1299. This discrepancy in the result for detector 1373 could be explained by an unintentional change in the QD size during the growth process. Furthermore, several unexplained features in the responsivity spectra, such as line-splitting, were also observed. Based on doping concentration and sheet density of QDs, it has been found that a single QD consists of one electron[18]. Multiple electrons within a QD could lead to a splitting of photo response peaks due to intralevel and interlevel Coulomb interactions[44]. Therefore, the secondary peaks superimposed on the primary peaks may result from either different QD sizes in the same DWELL structure or Coulomb interactions between multiple electrons in the QD. The expected red-shift due to Coulomb interaction with an applied electric field could be compensated by the blue-shift due to the Stark effect.[44] Splitting of absorption peaks is also possible through inter-dot coupling,[45] which depends on the random distribution of QDs.

The spectral responsivity of the third peak of 1388 in the VLWIR region under different applied bias fields is shown in Fig. 2.6. From 8-band **k.p** modeling[46], it is found

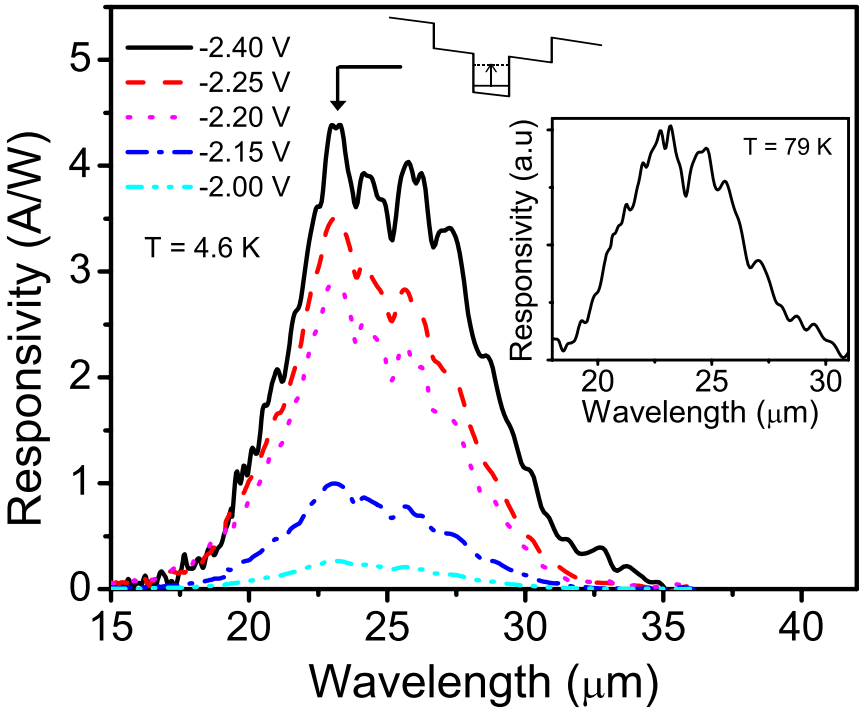

Figure 2.6: VLWIR response of 1388 at different bias values (negative indicates that the top-contact is negative). The band diagram represents the transition leading to the response. The inset shows the responsivity at high temperature (79 K).

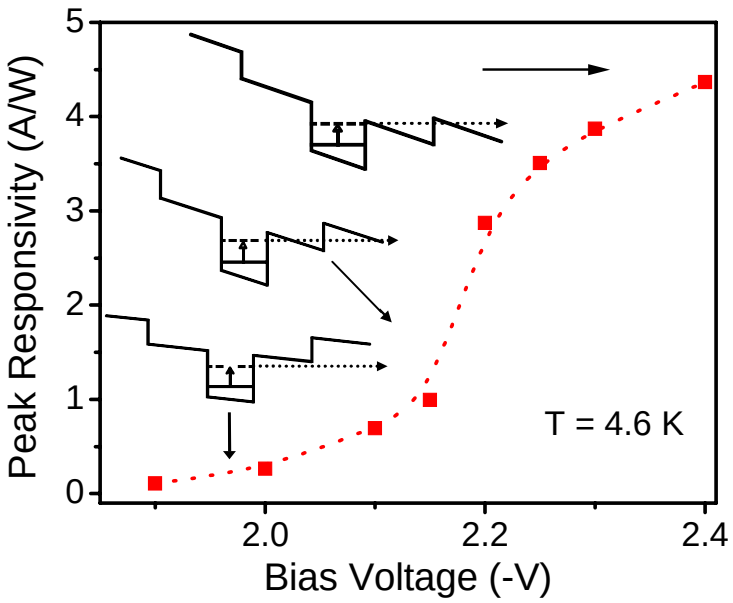

Figure 2.7: Variation of the peak responsivity of 1388 detector with applied bias. Variation of the conduction band profile with applied bias (electric field) shows that excited electrons escape through the barrier by field-assistant tunneling.

that the energy separation between states in the QDs, with a base diameter of 20 nm and a height of 7-8 nm, is about 50-60 meV. Thus, the VLWIR peak at $\sim$ 23.3 μm is probably due to transitions between two bound states within the QD. The energy level diagram corresponding to this transition is shown in the inset to Fig. 2.6. The variation of peak responsivity of the 23.3 μm peak with the bias voltage is given in Fig. 2.7. As shown in the energy band diagrams in the inset, carriers excited from the ground-state to the first excited-state in the QD have to tunnel through the QW first and then through the barrier into the continuum, in order to be collected by the external circuit. With increasing field strength, the barrier is pulled down strongly allowing the excited carriers to tunnel through a thinner barrier. This leads to field-assisted tunneling, where the applied field increases the escape probability of excited carriers. As a result, the experimental response curves show a drastic increase in response when the reverse bias is increased from -1.0 V to -2.4 V. Moreover, the peak at 23.3 μm is broader than that expected for a bound-to-bound transition in the QD. This is attributed to the 10% size fluctuation of the QDs during self assemble growth process.

Figures of merit of the three detectors (1299, 1373, and 1388) under the optimum operating conditions are given in Table 2.1. The VLWIR peak of 1373 could be obtained up to 60 K, while the VLWIR peaks of 1299 and 1388 were observed up to 80 K. The highest detectivity at 23.3 μm, $\sim 7.9 \times 10^{10}\ cm\sqrt{Hz}/W$, was obtained for 1388 at 4.6 K under a -2.2 V bias. At 80 K, the maximum detectivity was $3.2 \times 10^{8}\ cm\sqrt{Hz}/W$ at 80 K under a -1.4 V bias. At 23.3 μm, the 1388 detector exhibits lower responsivity and a lower noise current than those of 1299 (a comparison of dark current is given in Fig. 2.3), resulting in

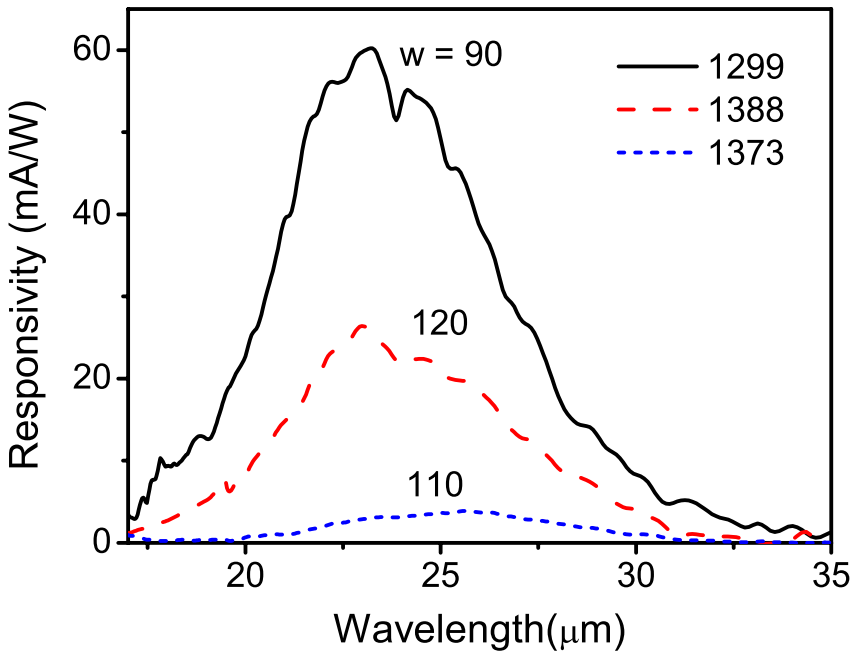

Figure 2.8: Spectral response of the VLWIR peak for all three detectors at 4.6 K under -1.4 V bias (-23.7, -22.9, and -22.5 kVcm^{-1} field for 1299, 1373, and 1388, respectively). The peak occurs at approximately the same wavelength (23.3 μm) for both the 1299 and 1388 detectors. Changing the width of the QW does not affect the energy states in the QD, thus confirming that the VLWIR peak is due to transitions between QD states.

Detector Number	Well Width ($\mathring{A}$)	λ_{peak} (μm)	Responsivity (mA/W)	Detectivity ($cm\sqrt{Hz}/W$)
1299	90	4.2	3.9	1.1×10^9
		8.1	14.0	3.9×10^9
		23.3	60.2	1.9×10^{10}
1373	110	6.25	3.0	5.4×10^9
		9.7	12.9	2.3×10^{10}
		25.5	3.8	6.9×10^9
1388	120	6.25	1.8	6.2×10^9
		10.5	2.8	1.7×10^{10}
		23.3	25.6	6.6×10^{10}

Table 2.1: Responsivity and detectivity of each peak of 1299, 1373, and 1388 detectors at 4.6 K with -1.4 V bias (~ -22.5 kVcm^{-1} field). The MWIR and LWIR peaks for all detectors were observed up to 80 K, whereas the VLWIR peak of 1373 could be obtained up to 60 K, while the VLWIR peaks of 1299 and 1388 were observed up to 80 K.

a higher detectivity for 1388 than for 1299. The improvement in operating temperature of VLWIR response (up to 80 K), compared with a typical VLWIR QWIP[47] operating at $\sim$ 10-20 K, demonstrates the benefit of having a quasi-zero dimensional QD confinement.

As shown in Fig. 2.8, the VLWIR peaks occur approximately at the same wavelength (23.3 μm) for both the 1299 and 1388 detectors. Changing the width of the QW does not affect the energy states in the QD, thus confirming that the FIR peak is due to transitions between QD states. However, the VLWIR peak of 1373 appears at 25.5 μm, as shown in Fig. 2.8, showing a red-shift with respect to the VLWIR peaks of 1299 and 1388. This observation was attributed to the unintentional increase of QD size in detector 1373 during the growth process, resulting in a decreased energy spacing between the ground and the first excited-states in the QD. In addition, this would also decrease the energy spacing between the ground-state in the QD and the bound state in the QW. As a result, the first two peaks will appear at longer wavelengths than expected. This was observed in the spectral response curves of the 1373 detector (see Fig. 2.5).

2.4 Conclusion

All the peaks of DWELL detectors are based on transitions between energy states in the QD and the QW. The operating wavelength in the MWIR and LWIR ranges can be tailored by varying the applied bias. Detectors can be designed by changing the well width or the size of the QD so that they can be operated at different wavelengths depending on the applications. Normal incidence and high temperature operation in the VLWIR region are advantages of DWELL detectors over n-type QWIPs.

Chapter 3

Tunneling Quantum Dot Infrared Photodetectors (T-QDIPs)

3.1 Introduction

At present, commercially available IR detectors work at cryogenic temperatures, thus single element devices and FPAs made of these detectors require cryogenic coolers. These detector systems are complicated, bulky, and very expensive. The most effective way to overcome these drawbacks would be the development of IR detectors capable of operating at room temperature. However, the development of room temperature IR detectors is a challenge as the rate of thermal excitations leading to the dark current increases exponentially with temperature. While a QD-based structure is a potential choice, conventional QDIP structures have not shown adequate performance above 150 K. At temperatures above 150 K electron occupation is dominated by the excited-states in the QD; and as a result, the reduction in the dark current is not significant. As a solution, a new QD-based device

architecture[48] was explored, demonstrating room temperature IR detection.

Aslan et al.[49] have recently observed resonant tunneling through a QD layer. In general, any device structure designed to reduce the dark current will also reduce the photocurrent. A novel design, the tunneling quantum dot infrared photodetector (T-QDIP)[48, 46, 50, 51, 52] can counteract this problem using resonant tunneling to selectively collect the photocurrent generated within the quantum dots, while the tunneling-barriers (double-barrier system) block the majority of carriers contributing to the dark current. The limited operating temperature of detectors is associated with the dark current, which in turn related to the detector response wavelength region. Ideally, the resonant tunneling approach can be used to develop IR detectors operating at high temperatures irrespective of the response wavelength region. In this chapter, the characteristics of the room temperature T-QDIP, showing two color response at wavelengths of $\sim$6 and $\sim$17 μm are discussed.

Technically, a T-QDIP structure can be considered as an extended DWELL structure. That is, a DWELL structure coupled with a double-barrier system transforms to a T-QDIP structure, which have several advantages over DWELL. Conventional QDIPs have low inherent dark current, which can be further reduced using DWELL. Compared to DWELL, T-QDIPs exhibit low dark current due to dark current blocking by the double-barrier system. As a result, T-QDIPs have the potential to achieve higher operating temperatures. Additionally, photocurrent filtering by means of resonant tunneling in T-QDIPs offers a solution for low quantum efficiency, observed in other QD-based devices.

Quantum efficiency can be increased further through resonant cavity enhancement, which increases the absorption in the active region without increasing the dark current.

In addition, several other important properties of T-QDIPs include the tunability of the operating wavelength and the multi-color (band) nature of the photoresponse based on different transitions in the structure. The operating wavelength can be tailored by changing the parameters of the QW, QD, and double-barrier system. Using transitions between the energy levels of the QD and the energy levels of the QW, it is possible to obtain detectors with multiple distinct response peaks.

3.2 T-QDIP Structure and Theoretical Background

Incorporating resonant tunneling into QDIP structures reduces the dark current without reducing the photocurrent leading to high performances such as high responsivity, high detectivity and high operating temperatures. A typical T-QDIP consists of InGaAs QDs embedded in a AlGaAs/GaAs QW coupled to a AlGaAs/InGaAs/AlGaAs double-barrier system. The conduction band profile of a T-QDIP structure under an applied reverse bias is shown in Fig. 3.1. Pulizzi et al.[53] has reported resonant tunneling phenomena for a similar QD-based structure coupled with a double-barrier. The photocurrent generated by a transition from a state in the QD (E_1, E_2 or E_3) to a state in the QW (denoted as the resonant-state, E_r, as this state is associated with resonance tunneling) that is coupled with a state in the double-barrier system can be collected by resonant tunneling. The double-barrier system blocks the majority of the carriers contributing to the dark current (carriers excited to any state other than the resonant-state in the QW). It can be shown that the tunneling probability is near unity for carriers excited by radiation with energy equal to the energy difference between the QD ground-state and the resonant-state.

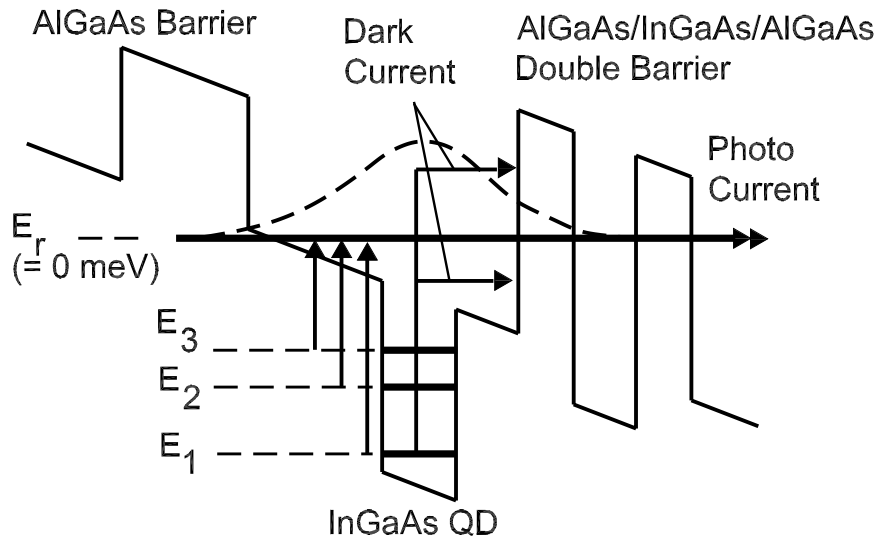

Figure 3.1: Schematic diagram of the conduction band profile of a T-QDIP structure under a bias. E_1, E_2 and E_3 are the energy level positions in the QD with respect to the resonant-state E_r. The photocurrent generated by a transition from a state in the QD (E_1, E_2 or E_3) to a state in the QW (denoted as the resonant-state, E_r, since this state is associated with resonance tunneling), which is coupled with a state in the double-barrier system can be collected by resonant tunneling.

The first step in designing a T-QDIP is the calculation of the QD energy levels using the 8-band **k.p** model[46]. This model uses the strain in the QD calculated using the valence force field (VFF) model, which has proven successful in calculating the strain tensor in self-assembled QDs. The size of the QD and the confinement potential should be determined such that the required spacing between energy levels can be obtained. For example, in order to design a two-color T-QDIP with response peaks at 5 and 10 μm, the ground and first excited-states in the QD (labeled as E_1 and E_2 in Fig. 3.1) should be 248 and 124 meV below the resonant-state energy. The energy spacing between states, $E_2 - E_1$ is equal to 124 meV. Theoretical calculations indicate that the energy difference between the ground and first excited-state in small InAs/GaAs QDs with a height of 60 Å and a width of 110 Å is approximately 124 meV. The width and the confinement potential of the QW are determined to obtain the resonant-state at a level such that the transitions from the E_1 and E_2 states to the resonant-state give rise to the peaks at expected wavelengths. The doping concentration in the QDs should be sufficiently high so that both states in the QD are filled with ground-state electrons. The energy states in the QW, including the presence of the wetting layer and the double-barrier system, are calculated by solving the one dimensional Schrödinger equation. The transmission probability for the double-barrier structure is calculated using the transfer matrix method[54].

The double-barrier system (AlGaAs/InGaAs/AlGaAs) is integrated with each QD layer of the QDIP, and is designed such that the resonant-state coincides with the photoexcited carrier energy under certain bias conditions. In this way, a higher potential barrier for thermal excitations can be introduced, while the photoexcitation energy is very low. Due

to the energy-dependent tunneling rate of the double-barrier system, the dark current resulting from carriers with a broad energy distribution is suppressed. Thus the dark current can be significantly reduced, particularly at high temperatures.

The intersubband absorption coefficient of a photon with energy $\hbar\omega$ in a QD layer can be expressed as[15],

$$\alpha(\hbar\omega) = \frac{\pi\ q^2\hbar}{\varepsilon_0 n_0 c m_0^2 V_{av}} \frac{1}{\hbar\omega} \sum_{fi} |a\ .\ p_{fi}|^2 N(\hbar\omega), \tag{3.1}$$

where $V_{a\nu}$ is the average dot volume, a is the polarization of the light, p_{fi} is the momentum matrix element between states, q is the electron charge, and $N(\hbar\omega)$ is the electron density of states. The Gaussian broadening due to the fluctuation in dot size is

$$N(\hbar\omega) = \frac{1}{\sqrt{2\pi}\sigma} \exp\left\{\frac{-(E_{fi} - \hbar\omega)^2}{2\sigma^2}\right\}, \tag{3.2}$$

where E_{fi} is the energy separation between states and σ is the linewidth of the transition. The momentum matrix element is calculated from the QD wavefunctions, which can be obtained from the 8-band **k.p** model.

The transmission probability for the T-QDIP structure is calculated using the transfer matrix method reported by Anemogiannis et al.[54] In addition, this model can be used to obtain the possible energy states in a 2-D quantum structure along with the carrier lifetime corresponding to each energy state. Consider the T-QDIP structure along with its conduction band profile shown in Fig. 3.2. For the i^{th} region, the Schrödinger equation has the following form,

$$\frac{d^2}{dz^2}\psi_i(z) + k_i^2(z)\psi_i(z) = 0 \tag{3.3}$$

$$k_i = \pm\sqrt{\frac{2m_i^*}{\hbar^2}(E - V_i)}, \tag{3.4}$$

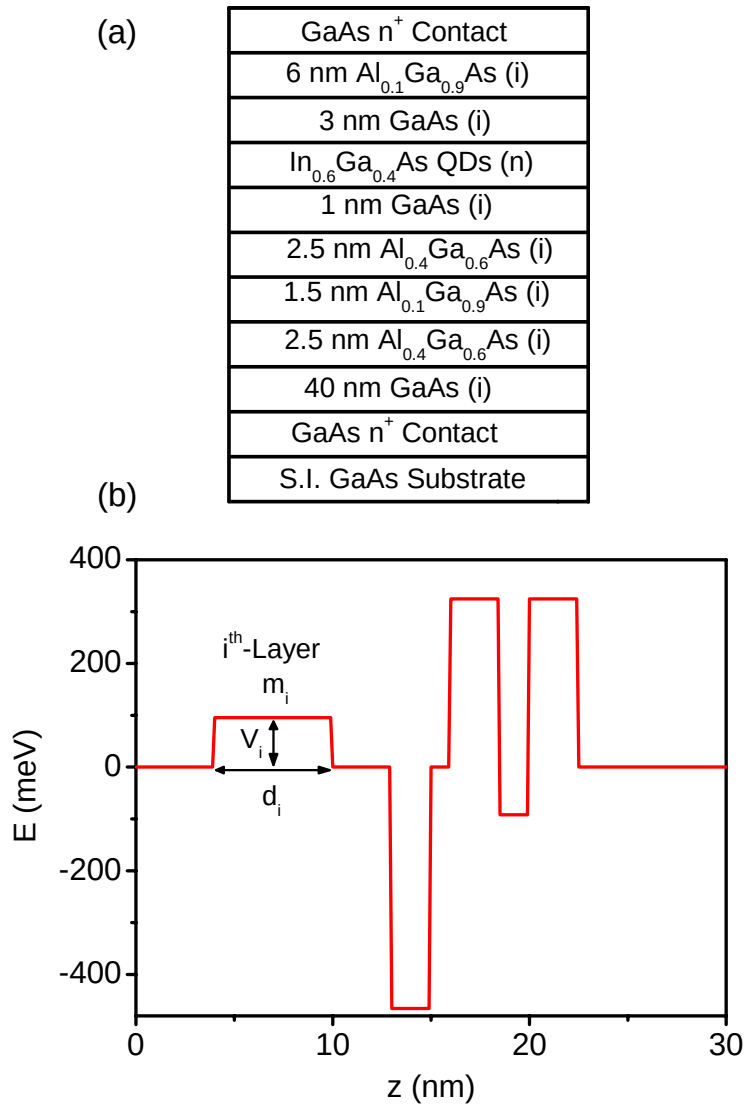

Figure 3.2: (a) A T-QDIP structure used for calculation, and (b) its conduction band profile. The parameters in the i^{th} layer: v_i, d_i, and m_i are potential energy, width of the layer, and electron effective mass, respectively.

where ψ_i, k_i, m_i^*, and V_i represent the envelop function, wave number, effective mass, potential energy in the i^{th} layer. E is the real eigenstate energy level. The solution for the wave function can be written as,

$$\psi_i(z) = A_i exp[jk_i(z - z_{i-1})] + B_i exp[-jk_i(z - z_{i-1})], \tag{3.5}$$

where A_i and B_i are wavefunction expansion coefficients.

$$\begin{pmatrix} A_i \\ B_i \end{pmatrix} = \begin{pmatrix} \frac{1}{2}[1 + \frac{k_{i+1}m_i^*}{m_{i+1}^*k_i}]\exp(-jk_id_i) & \frac{1}{2}[1 - \frac{k_{i+1}m_i^*}{m_{i+1}^*k_i}]\exp(-jk_id_i) \\ \frac{1}{2}[1 - \frac{k_{i+1}m_i^*}{m_{i+1}^*k_i}]\exp(+jk_id_i) & \frac{1}{2}[1 + \frac{k_{i+1}m_i^*}{m_{i+1}^*k_i}]\exp(+jk_id_i) \end{pmatrix} \begin{pmatrix} A_{i+1} \\ B_{i+1} \end{pmatrix} = M_{i,i+1} \begin{pmatrix} A_{i+1} \\ B_{i+1} \end{pmatrix}, \tag{3.6}$$

where d_i is the thickness of the i^{th} layer.

Using the boundary conditions, the transmission and reflection coefficients, t and r, can be calculated from;

$$\begin{pmatrix} 1 \\ r \end{pmatrix} = \begin{pmatrix} M_{11}(E) & M_{12}(E) \\ M_{21}(E) & M_{22}(E) \end{pmatrix} \begin{pmatrix} t \\ 0 \end{pmatrix}. \tag{3.7}$$

Then the transmission probability, T, can be found from,

$$T(E) = \frac{k_{N+1}m_0^*}{k_0 m_{N+1}^*}|t^2|. \tag{3.8}$$

For the T-QDIP structure shown in Fig. 3.2, the energy states and the transmission probabilities under different applied bias values, calculated using this model (for implementation of the model, see Appendix C), are shown in Fig. 3.3.

The spectral responsivity of the detector is characterized by peak wavelength (λ_p), peak responsivity (R_p), and the peak quantum efficiency (η_p). The responsivity is given by $R = q\eta\lambda/hc$, where q is the electron charge, λ is the wavelength, h is Planck's constant

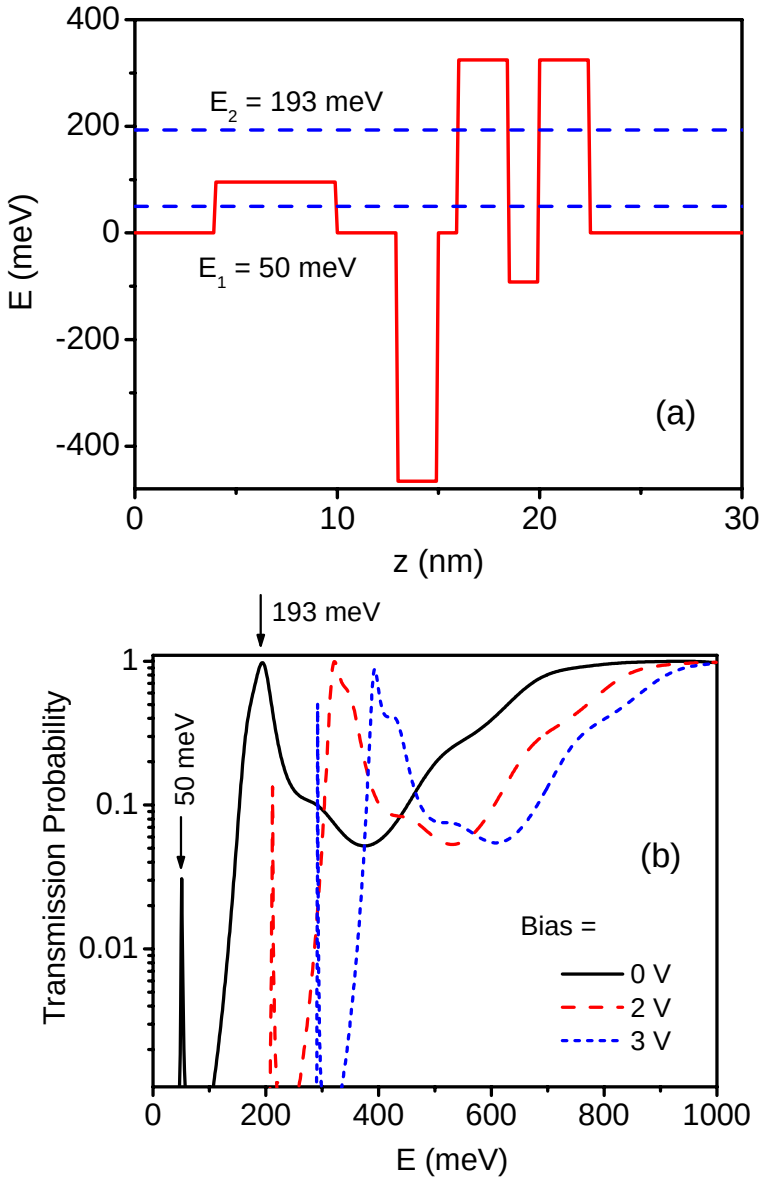

Figure 3.3: (a) Calculated energy states and (b) the transmission probabilities under different applied bias values for the T-QDIP structure shown in Fig. 3.2.

and c is the speed of light. The quantum efficiency can be calculated from the absorption coefficient (from Eq. 3.1), the thickness of the absorption region, and the transmission probability (from Eq. 3.8).

In order to achieve background limited infrared performance (BLIP) conditions at high temperatures, the detector should exhibit an extremely low dark current density. A T-QDIP detector, designed to have strong resonant tunneling is capable of achieving high BLIP temperatures. The dark current, I_d, of a T-QDIP structure at a bias, V, is given by,[51]

$$I_d(V) = qv(V)n_{em}(V)A, \tag{3.9}$$

where A is the device area, v and n_{em} (given by equations 3.10 and 3.11) are the average electron drift velocity in the barrier material and the concentration of electrons excited out of the QD, respectively. The electron drift velocity is given by

$$v(V) = \frac{\mu\ F(V)}{\sqrt{1 + (\frac{\mu\ F(V)}{v_s})^2}}, \tag{3.10}$$

where μ is the electron mobility, F is the electric field, and v_s is the electron saturation velocity. The excited electron density from the QD is given by

$$n_{em}(V) = \int_{-\infty}^{\infty} N(E)f(E)T(E,V)dE, \tag{3.11}$$

where $f(E)$ is the Fermi-Dirac distribution function, $T(E,V)$ is the tunneling probability calculated from Eq. 3.8, and $N(E)$ is the density of states, which is given by the following equation,

$$N(E) = \sum_i \frac{2N_d}{L_p}\frac{1}{\sqrt{2\pi}\sigma}\exp\left\{\frac{-(E_{fi}-E)^2}{2\sigma^2}\right\}$$
$$+\frac{4\pi\ m^*}{L_p h^2}H(E-E_W) + \frac{8\pi\sqrt{2}}{h^3}(m^*)^{(3/2)}\sqrt{E-E_C}H(E-E_C), \tag{3.12}$$

where the first term is the density of states of the QD state and N_d is the surface density of QDs. The second term is the density of the wetting layer states, where E_W is the wetting layer state, and $H(x)$ is a step function with $H(x) = 1$ for $x \geq 0$ and $H(x) = 0$ for $x < 0$. The third term represents the density of states in the barrier material, where E_C is the conduction band edge of the barrier material.

As shown in Fig 3.1, the carriers excited to any state other than the resonant-state are blocked by the tunnel barriers. However, for efficient dark current blocking the broadening of the resonant-state has to be a minimum. That is, the resonant-state should be strongly bound. Basic parameters should be adjusted so that the tunneling probability remains close to unity and the carrier escape lifetime is smaller than the carrier recombination lifetime. Also the Fermi level in the QD (hence QD ground-state) should be below the band edge of the QW. However, adjusting the ground-state will change the energy difference between the QD ground-state and the resonant-state, affecting the peak response wavelength. Thus, all these factors need to be taken into account in designing an optimized detector exhibiting low dark current.

3.3 Two-Color Room Temperature T-QDIP Detectors

A T-QDIP structure[48] (MG386) was grown by MBE at the University of Michigan, and the characterization was carried out by performing I-V, spectral response, and noise measurements. The preliminary results demonstrated that room temperature operation is possible due to resonant tunneling phenomenon in the structure. The device showed a two color response at wavelengths of $\sim$6 and $\sim$17 μm up to room temperature. To our

knowledge, this is the first T-QDIP device to achieve room temperature operation. A detailed explanation of the device structure, spectral response and device performance are given in following sections.

3.3.1 Device Structure and Experiment

The structure (MG386) grown by MBE is schematically shown in Fig. 3.4. A schematic diagram of the conduction band profile of the detector under reverse applied bias is shown in Fig. 3.5 along with the calculated bound state energies in the dots and wells. Self organized $In_{0.1}Ga_{0.9}As$ QDs were grown on a GaAs layer. A stack of $Al_{0.3}Ga_{0.7}As/In_{0.1}Ga_{0.9}As/Al_{0.3}Ga_{0.7}As$ layers serve as the double-barrier system. The conduction band profile of the T-QDIP structure under an applied reverse bias is shown in Fig. 3.1. The GaAs and AlGaAs layers were grown at 610°C and the InGaAs or InAlAs QD layers were grown at 500°C. Vertical circular mesas for top illumination were fabricated by standard photolithography, wet chemical etching and contact metallization techniques. The n-type top ring contact and the n-type bottom-contact were formed by evaporated Ni/Ge/Au/Ti/Au with a thickness of 250/325/650/200/2000 Å. The radius of the optically active area is 300 μm. Samples with devices to test were mounted onto chip carriers with silver epoxy. Then electrical contacts were made by bonding gold wires from devices to the chip carrier leads. Characterization was carried out as explained in Appendix A. The I-V measurements were performed, using a Keithley 2400 source meter, on all the mesas of the sample in order to check for dark current leakage and uniformity of the structure. Spectral measurements for normal incidence radiation were carried out by using a Perkin Elmer System 2000 Fourier Transform Infrared spectrometer. The spectra were calibrated relative to a reference spectrum obtained by a

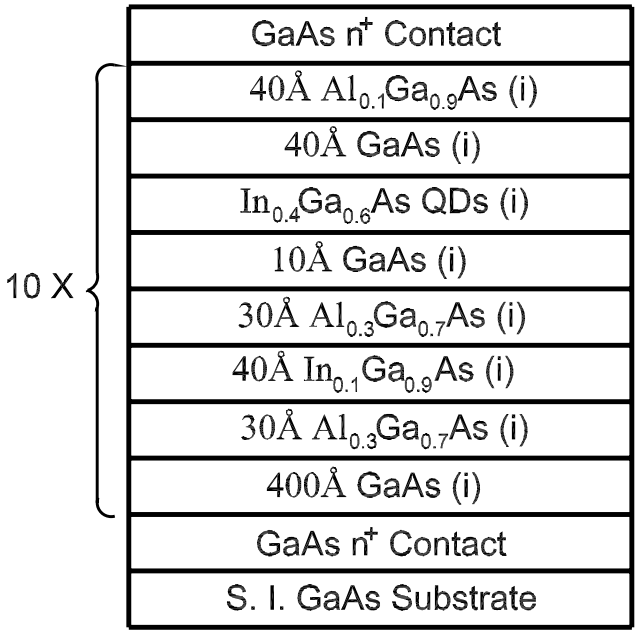

Figure 3.4: Schematic heterostructure of a T-QDIP grown by molecular beam epitaxy. InGaAs QDs are placed in a GaAs well. The AlGaAs/InGaAs/AlGaAs layers serve as a double-barrier system to decouple the dark and photo currents. The letter "i" stands for intrinsic.

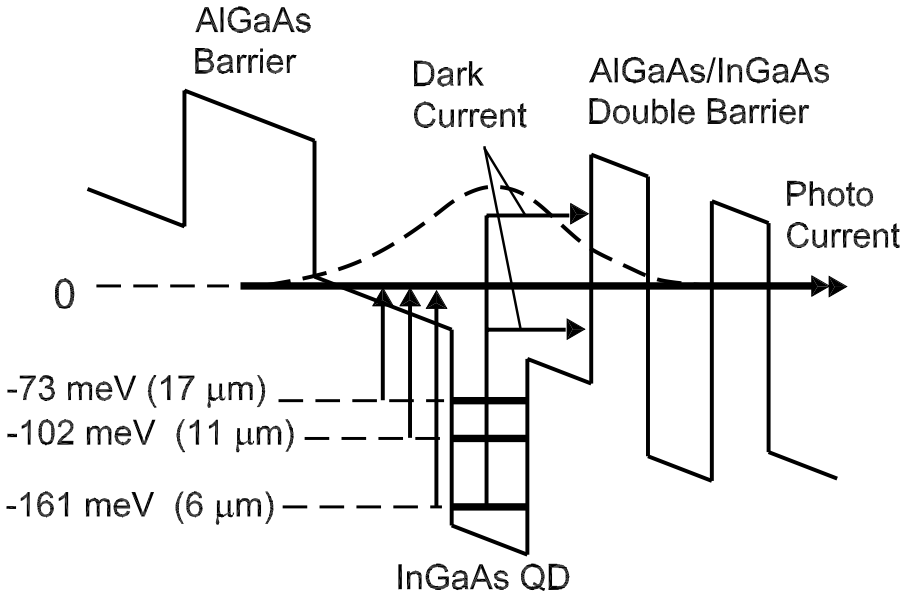

Figure 3.5: A schematic diagram of the conduction band profile of the T-QDIP detector (MG386) under reverse applied bias along with the calculated bound state energies in the dots and wells. The dark current channels are blocked by the barrier unless they happen to be excited to match the resonance level.

Si composite bolometer with the same set of optical components. The specific detectivity (D*) of the devices at different temperatures and applied biases is obtained from the measured peak responsivity R_p and noise current density, S_i, measured with a Fast Fourier Transform (FFT) signal analyzer and a low noise pre-amplifier. A thick copper plate, close to the device and at the same temperature as the device, was used as the radiation block to provide the dark conditions for the measurements (for more details, see Appendix A: Device Characterization).

3.3.2 Dark Current Measurement

Dark I-V measurements were performed for both bias polarities, where positive (or negative) bias denotes positive (or negative) polarity on the top-contact. The I-V characteristics of MG386 at different temperatures ranging from 80-300 K are shown in Fig. 3.6 (a). A comparison of the dark current density between DWELL (1299)[19] and T-QDIP (MG386) detectors at 80 K is shown in Fig. 3.6 (c). Dark current densities at a bias of -2 V are 3×10^{-1} and 1.8×10^{-5} A/cm^2 for DWELL and T-QDIP, respectively. The reduction in the dark current of T-QDIP is associated with dark current blocking by the double-barrier system in the structure. Moreover, dark current densities at a bias of 1 V are 0.21, 0.96, and 1.55 A/cm^2 at 240, 280 and 300 K, respectively. These dark current density values are lower than the dark current values of other IR detectors operating in comparable wavelength regions at the same temperature. Based on the dark current variation as a function of bias, negative conductance peaks were not visible even though resonant tunneling takes place in the structure. This observation can be expected for T-QDIPs since sequential resonant tunneling through ground-state is not possible. In T-QDIPs, there is no coupling between

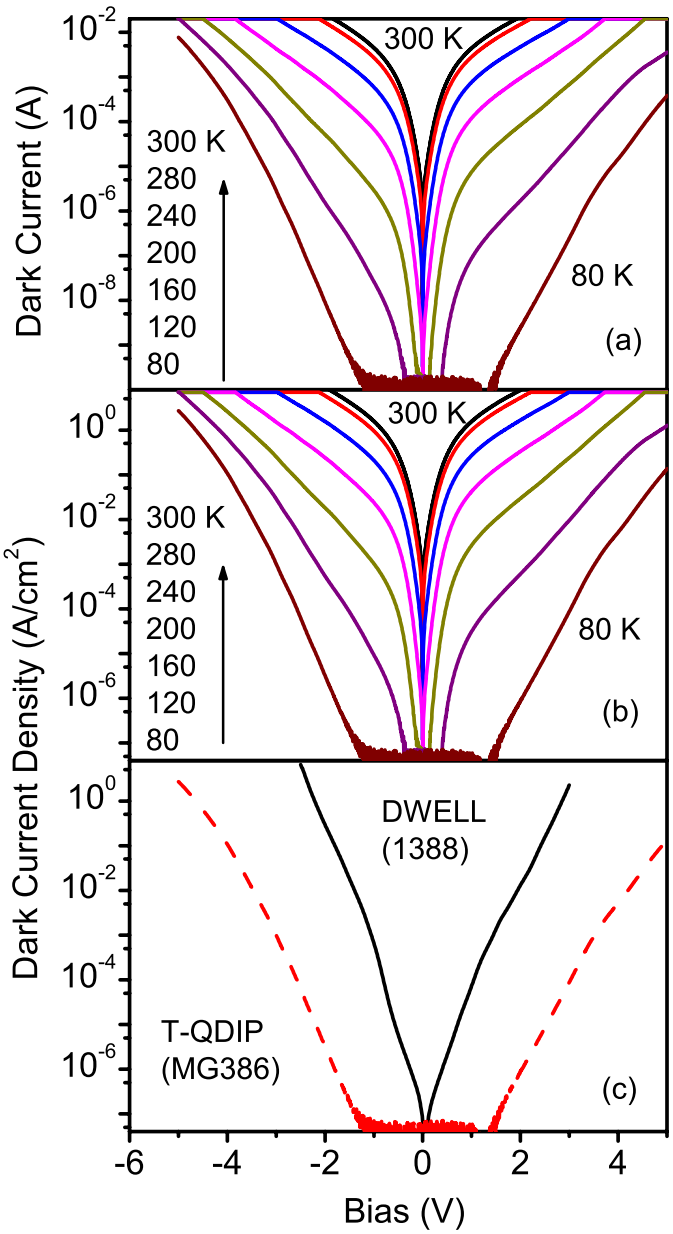

Figure 3.6: (a) Dark current and (b) dark current density of the T-QDIP detector (MG386) as a function of bias in the temperature range 80-300 K. The reduction of the dark current in T-QDIP is attributed to dark current blocking by double-barrier system. (c) A comparison of the experimental dark current density between DWELL (1299) and T-QDIP (MG386) detectors at 80 K.

the QD ground-state and states in the double-barrier (unlike in superlattice structures[55]). Also, each active region of T-QDIP is separated by a thick spacer layer (400 Å GaAs) which does not allow any significant coupling between two active regions (two periods). Thus, I-V curves are not expected to display negative conductance regimes. Furthermore, it is important to note the thin AlGaAs barriers (30 or 40 Å) on both sides of the QW. Even though the double-barrier is placed only on one side of the QW (on the right side according to Fig. 3.1), tunneling through the single-barrier on the opposite side (on the left side of the QW) is also possible. However, the transmission through this barrier is lower compared to that through the double-barrier. Thus, an asymmetric I-V characteristic was observed.

3.3.3 Spectral Responsivity

The spectral response of MG386 at 80 K under different bias values is shown in Fig. 3.7 (a), and the variation in peak responsivity at 6.2 μm is demonstrated in Fig. 3.7 (b). Based on calculations, the allowed confined energy states in the QD E_1, E_2, and E_3 are located at -161, -103, and -73 meV with respect to the resonant-state (see Fig. 3.1). Thus the peak at $\sim$6 μm is due to transitions from the ground-state of the QD to the resonant-state in the structure, which is consistent with the calculated energy spacing between corresponding states (ΔE = 161 meV). The peak responsivity and the conversion efficiency (the product of quantum efficiency and the photoconductive gain) of the 6 μm peak at 80 K and -4.5 V are $\sim$0.75 A/W and 16%, respectively. Under reverse bias (top-contact is negative), the photoexcited electrons tunnel through the double-barrier by resonant tunneling. Similarly, under forward bias photoexcited electrons tunnel through the single barrier (on the oppo-

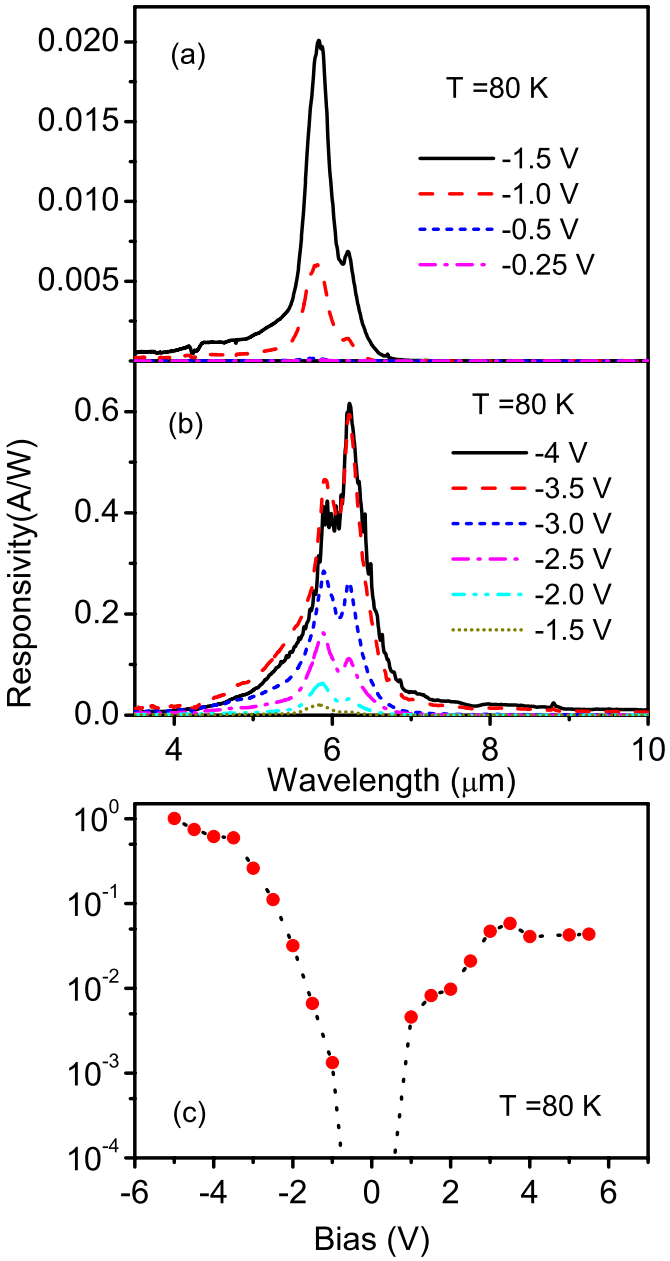

Figure 3.7: Bias dependence of the spectral responsivity of T-QDIP (MG386) at 80 K: (a) from -0.25 to -1.5 V, (b) from -1.5 to -4 V. (c) Variation of the peak responsivity with applied bias at 80 K.

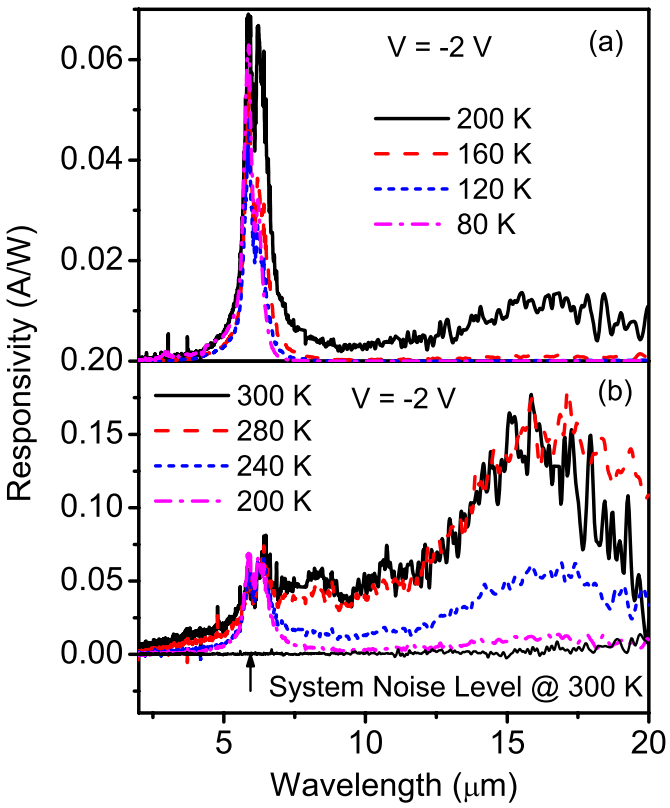

Figure 3.8: Spectral responsivity of T-QDIP (MG386) in the temperature range (a) 80-200 K, and (b) 200-300 K under -2 V bias. Two distinct peaks centered around ∼6 and ∼17 μm can be observed at high temperatures, and a weak response around 11 μm is also visible. The system noise level at 300 K, which is a spectrum taken under dark conditions, is also shown.

site side of the double-barrier system). Due to the variations in transmission through the single and double-barriers, the response under reverse bias is significantly higher than the response under forward bias, as evident from Fig. 3.1. However, the responsivity shows a strong dependence on the applied bias in both positive and negative directions. This behaviour is attributed to resonant tunneling similar to that of double-barrier superlattice structures.[49, 56] Applying a bias across the structure can fine-tune the alignment of the bound state in the QW (resonant-state) and the bound state in the double-barrier system, allowing for resonant tunneling conditions. The observed bias dependence of the responsivity indicates that resonant conditions are satisfied over a considerable range of applied bias voltages. This behavior could be associated with thin barriers and the broadening of the energy states (δE) in the system.

The spectral response of MG386 under -2 V bias at different temperatures in the range of 80-300 K is shown in Fig. 3.8 (a) and (b). Two distinct peaks centered around $\sim$6 and $\sim$17 μm were observed at high temperatures, and a weak response around 11 μm was also present. The peak at 17 μm results from transitions between the second excited-state of the QD and the resonant-state (ΔE = 73 meV). The line-width is $\sim$26 meV, which corresponds to the inhomogeneous broadening of QD states at 300 K. Due to the symmetry of QD geometry, excited-states have a higher degeneracy (8) than the ground-state (2). The carrier density in excited-states increases with increasing temperature, as compared to that in the ground-state. As a result, the 17 μm peak was dominant above 200 K, as evident from Fig. 3.8. The weak response at $\sim$11 μm corresponds to the energy separation between the first excited QD state and the resonant-state (ΔE = 102 meV).

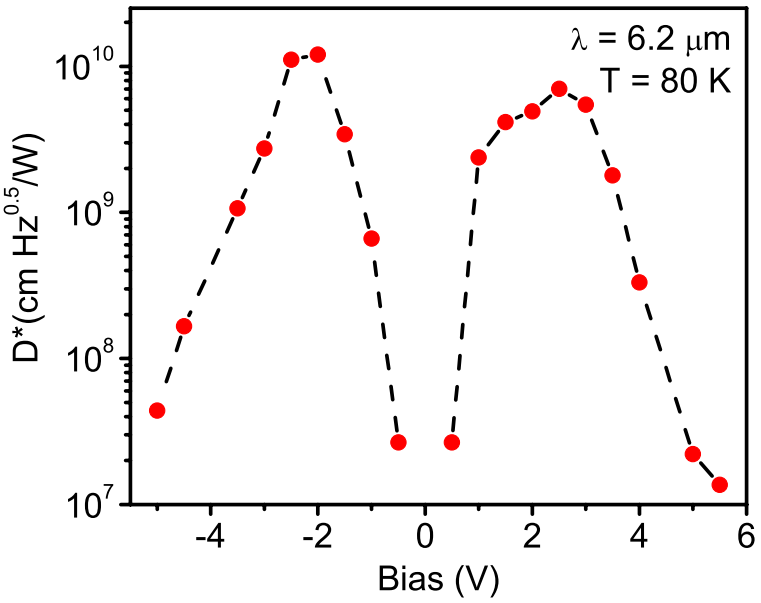

Figure 3.9: Variation of detectivity of the T-QDIP detector (MG386) response at 6.2 μm as a function of bias at 80 K. The rate of increasing noise current with bias is much higher than the rate of increasing responsivity with bias, resulting in lower D* at higher bias voltages (above $\pm$ 2V).

3.3.4 Noise Measurement and Detectivity

The noise current density spectra of the devices were measured with a dual-channel Fast Fourier Transform (FFT) signal analyzer and a low noise pre-amplifier. A thick copper plate, maintained at almost the same temperature as of the device measured, is used as the radiation block to provide the dark conditions (for more details, see Appendix A: Device Characterization). Similar to QWIPs,[57, 58, 59] QDIPs exhibit 1/f noise and generation-recombination noise components due to the emission and capture processes in shallow states. The noise spectrum due to 1/f and generation-recombination noise has the form,

$$S(f) = C + \frac{B}{f} + \frac{A}{1 + (\frac{f}{f_c})^2}, \tag{3.13}$$

where A, B, and C are constants. The cut off frequency, f_c, is given by $f_c = 1/2\pi\tau_0$ where τ_T is the electron life time, which is given by

$$\tau_T \propto T^{-2} \exp(\frac{E_A}{kT}), \tag{3.14}$$

where T is the temperature, k is the Boltzmann constant and E_A is the activation energy of the thermally activated trap level. Using noise current density spectra at different temperatures, the variation of τ_T with temperature can be determined. Based on Eq. 3.14, the plot of $\log(\tau_T/T^2)$ against $1/T$ would result in a straight line with a slope of E_A/k, which can be used to calculate the activation energy of the trap level.

The value of D* of the device at different temperatures and applied biases is obtained from the measured peak responsivity and noise density spectra, as explained in Appendix A. At 80 K and under a bias of -2 V, the maximum D* was found to be 1.2×10^{10} cmHz$^{1/2}$/W. The variation of D* corresponding to 6.2 μm at 80 K is shown in Fig. 3.9. The

rate of increasing noise current with increasing bias is much higher than the rate of increasing responsivity with increasing bias, resulting in lower D* at higher bias voltages (beyond ± 2 V). This variation in D* with changing bias is expected for a typical photodetector. The value of D* at 17 μm and 300 K is of the order of 10^7 cmHz$^{1/2}$/W, and with some re-designing of the device heterostructure, a higher D* is possible for the same conditions.

3.4 T-QDIPs for Terahertz Radiation Detection

3.4.1 Introduction

With increasing interest in the terahertz region of the spectrum (0.1-3.0 THz), there is a need for terahertz detectors exhibiting low dark current and high operating temperatures for applications in imaging, communication, security and defense. The primary challenge in developing terahertz detectors is the reduction of the dark current (due to thermal excitations) associated with terahertz detection mechanisms in the device structure. Presently, terahertz detectors such as Ge blocked impurity band (BIB) detectors,[60] photoconductors triggered by femtosecond laser pulses,[61] QW detectors,[62] heterojunction detectors[63], and thermal detectors, such as bolometers and pyroelectric detectors are being studied. However, all of these detectors operate at low temperatures. A typical detector structure, in which the transitions leading to terahertz detection occur between two electronic states with an energy difference of ΔE ($\sim$ 4.1 meV for 1 THz), would not be suitable for high temperature terahertz detection since the dark current due to thermal excitations become dominant even at 77 K due to the small ΔE. The T-QDIP structure[50], in which the photocurrent is selectively collected while the dark current is blocked, can be adjusted to

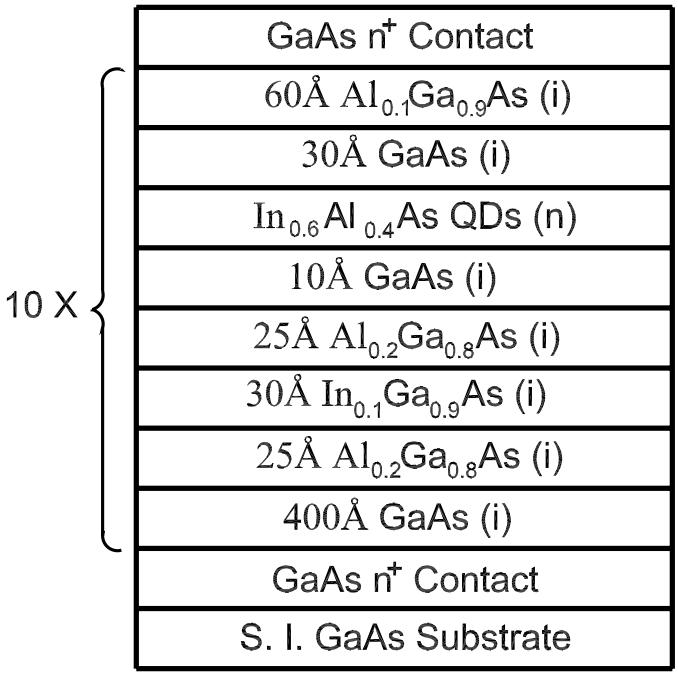

Figure 3.10: Schematic heterostructure of a T-QDIP THz detector. $In_{0.6}Al_{0.4}As$ QDs are n-doped with Si. The growth of smaller QDs compared to InAs or InGaAs QDs was achieved using InAlAs material. The QD size has been considerably reduced to 40 Å (height) and 130 Å(width).

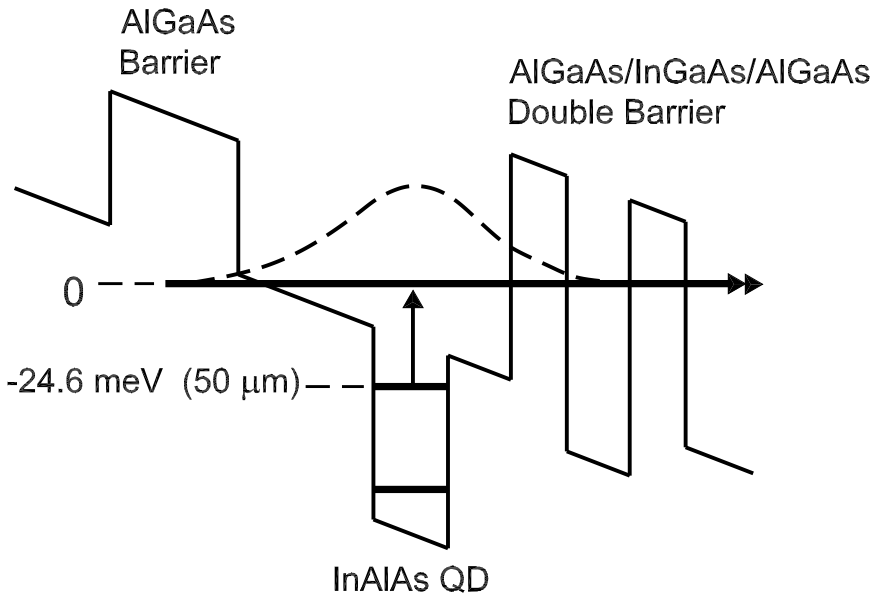

Figure 3.11: Schematic diagram of the conduction band profile of the THz T-QDIP under reverse applied bias along with the calculated bound state energies in the dots and wells. The dark current channels are blocked by the barrier unless they happen to be excited to match the resonance level. Photoexcitation occurs from the second bound state in the dot to the resonant-state in the well.

obtain terahertz response, thus, offering a suitable platform for high operating temperature terahertz detectors.

The schematic structure of a terahertz T-QDIP detector grown by MBE in an EPI Mod Gen II system equipped with an arsenic source, and the conduction band profile of the detector are shown in Figs. 3.10 and 3.11, respectively. The heterostructure was grown on (001)-oriented semi-insulating GaAs substrate. The GaAs and AlGaAs layers were grown at 610°C and the rest of the structure was grown at 500°C. The top and bottom GaAs contact layers are n-doped with Si to a level of 2×10^{18} cm^{-3}. Mesa-shaped vertical n-i-n devices for top illumination were fabricated by standard photolithography, wet chemical etching, and contact metallization techniques. The top and bottom n-type contacts were formed by evaporating Ni/Ge/Au/Ti/Au (thickness = 250/325/650/200/2000 Å, respectively) followed by annealling. In order to obtain a transition leading to a THz response, the excited-states in the QD are pushed towards the resonant-state by forming smaller QDs. The QDs are doped to raise the Fermi level so that photoexcitations take place from an upper state in the QD to the resonant-state. In order to reduce QD size, $In_{0.6}Al_{0.4}As$ was used because the Al-containing islands (QDs) are smaller in size compared to InAs islands due to the smaller migration rate of Al adatoms on the growing surface during epitaxy.

3.4.2 Growth of "Small" Quantum Dots by MBE

The typical size of the near-pyramidal InAs/GaAs self-organized QDs[19, 28] is ∼60-70 Å(height)/∼200-250 Å(base). The QD density varies in the range 5-10$\times10^{10}$ cm^{-2}. Typical electron intersublevel energy separation in such QDs ranges between 40 and 80

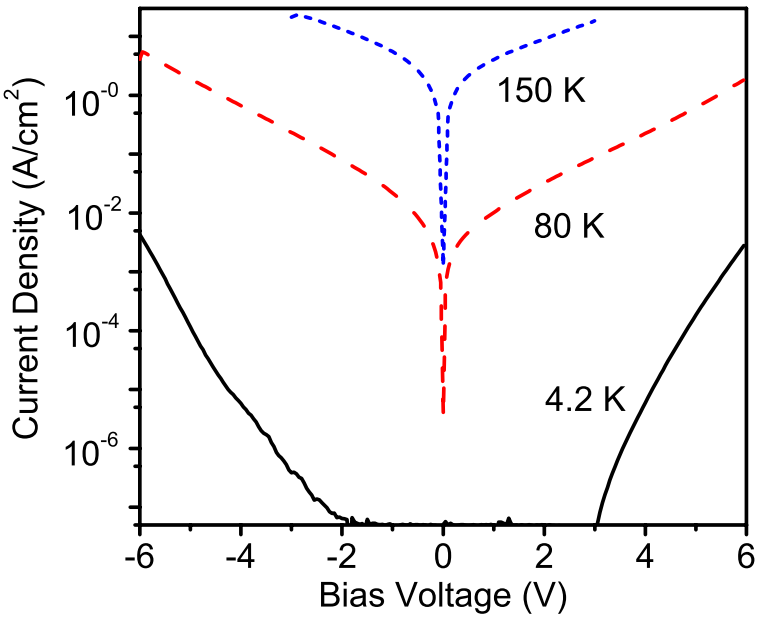

Figure 3.12: The dark current density of THz T-QDIP as a function of bias in the temperature range 4.2-150 K. In the reported response range, the T-QDIP detector shows a lower dark current density compared to other THz detectors operating in the ∼20-60 μm range.

meV. Based on calculated results, a large energy spacing (∼124 meV) between the QD ground and first excited-states can be obtained by using smaller QDs. Smaller QDs also provide a large QD density for the same amount of adatom change, which increases the absorption of radiation. QD size is reduced by inhibiting growth kinetics on the surface. This can be done either by growing QDs on an Al-containing material, or by incorporating a small amount of Al into the QD material. The presence of Al reduces the adatom migration lengths on the growing surface (insufficient kinetics), resulting in smaller QDs. During the investigation of terahertz T-QDIP operating at high temperatures, the QD size has been considerably reduced to 40 Å (height) and 130 Å(width). The reduced size of $In_{0.5}Al_{0.5}As$ QDs on GaAs increases the QD density by an order of magnitude.

3.4.3 Dark Current and Responsivity

The dark current density of the THz T-QDIP at different temperatures is shown in Fig. 3.12. The T-QDIP detector shows a lower dark current density compared to other THz detectors[64] operating in the ∼20-60 μm range. The spectral response of the detector at 80 and 150 K is shown in Fig. 3.13. The calculated energy difference between the two energy levels leading to the response is 24.6 meV (50.4 μm). Responsivity values at 80 and 150 K are 6 and 0.6 mA/W, respectively. The sharp dip around 37 μm is due to the reststrahlen band of GaAs, which is present in all GaAs based photon detectors[63, 65]. The observed full-width at half maximum (FWHM) of the spectral response is ∼35 meV (35 μm). This broadening arises due to the inhomogeneous size distribution of self-organized QDs. The measured D* value is $\sim 5\times10^7$ cmHz$^{1/2}$/W at 80 K under a bias of 1 V. Therefore, it can be concluded that THz operation at high temperatures (up to 150 K) is possible by

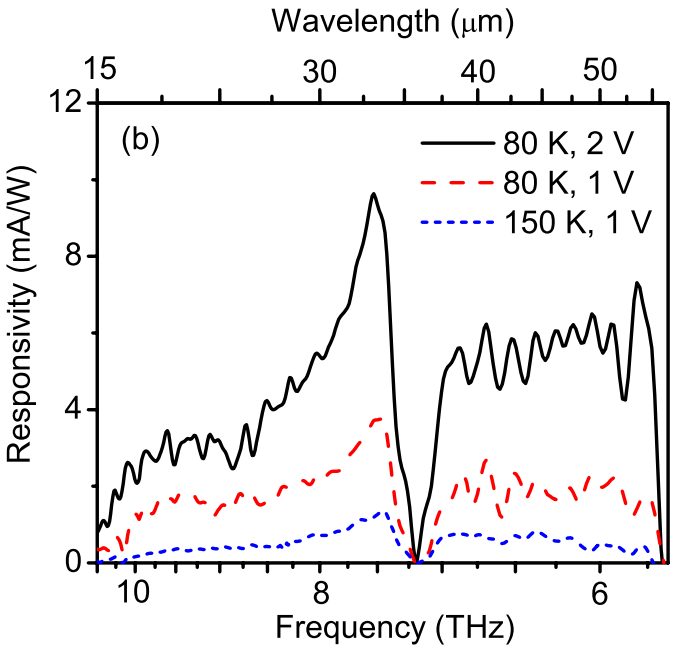

Figure 3.13: Spectral responsivity of THz T-QDIP in the temperature range 80-150 K. The dip at 37 μm is the reststrahlen region of GaAs. THz operation at high temperature (150 K) is made possible by the incorporation of resonant tunneling phenomena into the device design. The calculated energy difference between the two energy levels leading to the response is 24.6 meV (50.4 μm). The peak responsivity at 80 and 150 K are 6 and 0.6 mA/W, respectively.

incorporating resonant tunneling phenomena into the device design. However, in order to achieve THz detection in 1-3 THz region at high temperatures, several issues such as the growth of small QDs with reduced size fluctuation, optimization of structure parameters, and tight resonant conditions to maintain low dark current, need to be resolved.

3.5 Conclusion

T-QDIP detectors designed for room temperature operation and THz detection were investigated. As evident from the results, T-QDIPs exhibit lower dark current and work at higher operating temperatures, properties which made possible by the incorporation of double-barriers into the structure. This is clear advantage over other types of photon detectors. A 17 μm detector that can be operated at room temperature, and a 6 THz detector operating at 150 K were successfully demonstrated. The design of the T-QDIP structure can be modified for wavelength tuning and performance optimization.

Chapter 4

Bi-Layer Quantum Dot Detectors for Multi-Band Infrared Radiation Detection

4.1 Introduction

In this chapter, a QDIP detector structure consisting of two layers of QDs (Bi-QDIPs), where the QDs in the two layers are intentionally grown to be different in sizes, is presented. The main objective of the Bi-QDIP structure is to obtain uniform QDs in the second layer ("active" layer with large QDs), which is directly grown on the first QD layer with small QDs. The first QD layer is called the "stresser". Each QD yields one or two response peaks, and hence the detector can be used as a multi-color IR detector.

4.2 Device Structure and Experimental Results

A schematic diagram of the detector structure (MG593) grown by MBE with 20 periods of Bi-QDIPs and the conduction band profile of the structure are shown in Fig. 4.1.

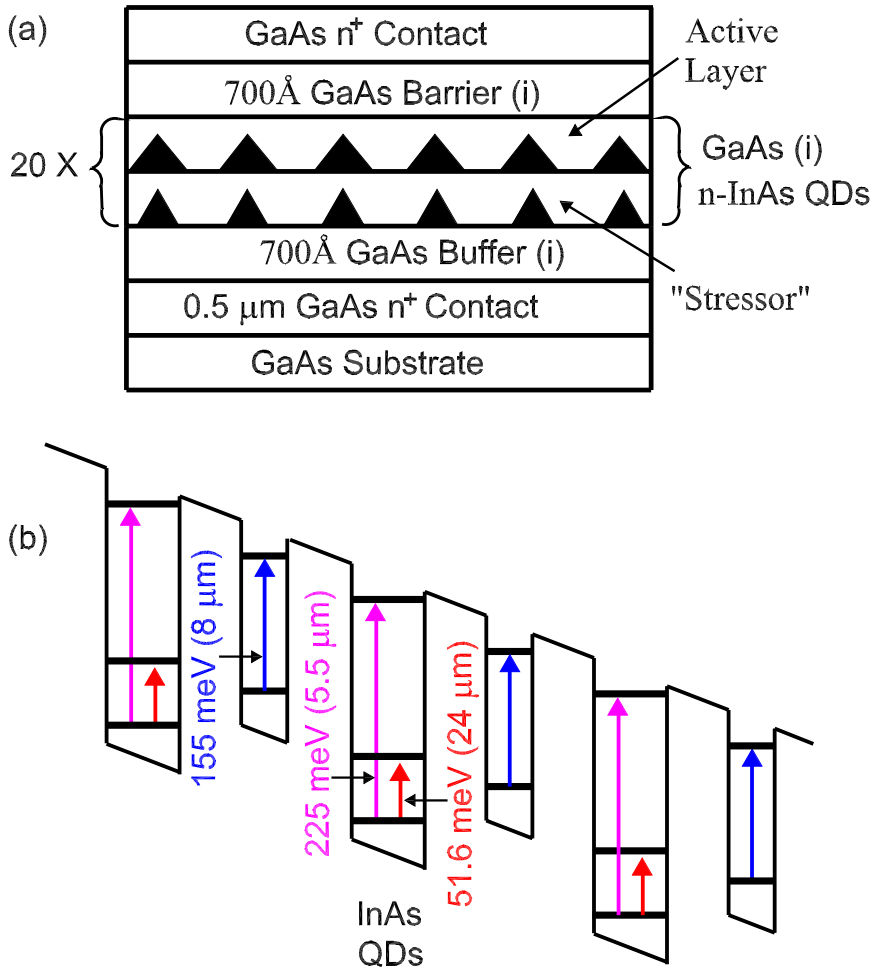

Figure 4.1: (a) Schematic heterostructure of a Bi-layer multi-color QDIP (MG593). On top of the first QD layer ("stresser"), another QD layer ("active" layer) is grown. In this way a good uniformity in the second QD layer can be achieved. (b) Schematic diagram of the conduction band profile of the Bi-QDIP. Energy states in each QD layer and expected transitions are also shown.

The heterostructure was grown on a semi-insulating GaAs substrate. The first (stresser) and the second (active layer) InAs QD layers were grown at 535°C and 480°C, respectively, with a growth rate of 0.01 ML/s. The thicknesses of the first and second QD layers are 2.4 and 3.1 ML, and each layer is covered with a 100 Å GaAs barrier layer. Under these conditions the first QD layer ends up being small in size, and a good vertical coupling between first and second QD layers can be obtained, resulting in excellent QD size uniformity in the second layer. The active QDs (larger QDs) consist of three bound states, while the stresser (small QDs) have two bound states due to the difference in size. Also, a change in band-gap of the stresser is expected[66] due to the high stress associated with the formation of small QDs. Energy states in each QD layer and expected transitions are also shown in Fig. 4.1.

Dark I-V characteristics of the Bi-QDIP (MG593) were obtained with a fully automated setup including a Keithley 2400 source meter (for more details, see Appendix A: Device Characterization). Measurements were performed for both bias polarities, where positive (negative) bias denotes positive (negative) polarity on the top-contact. The measured I-V curves of MG593 at different temperatures (80-160 K), are shown in Fig. 4.2. A very low dark current is observed, confirming high carrier confinement in the 3-D confined system. This can also be due to carrier blocking by the thick GaAs barriers between which 20 periods of bi-layer QDs are sandwiched. Unlike the T-QDIP detectors, both dark- and photo-currents are reduced in this structure, leading to a lower quantum efficiency than found in T-QDIPs. However, there are several improvements in spectral responsivity of Bi-QDIPs, which will be discussed in the following sections, compared to other QDIPs already discussed in previous chapters.

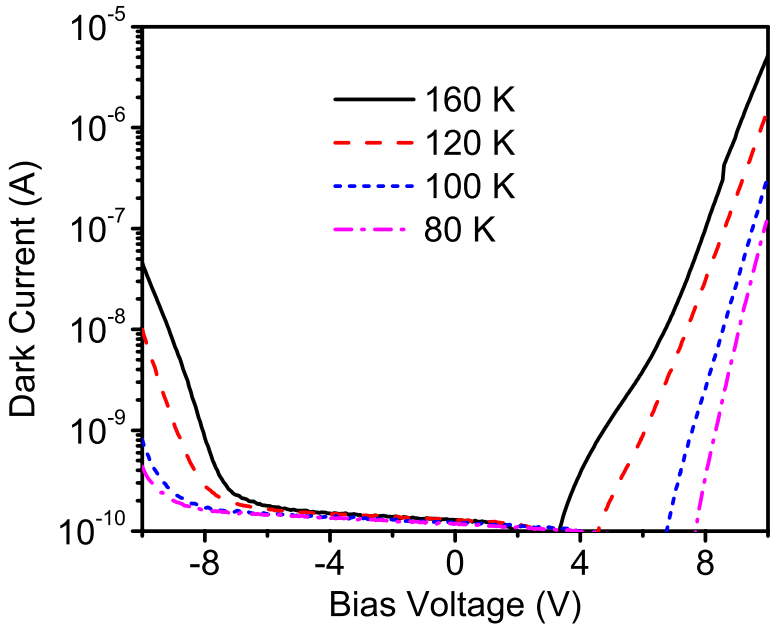

Figure 4.2: Dark I-V characteristics of the Bi-QDIP (MG593) at different temperatures. A very low dark current is observed, confirming high carrier confinement in the 3-D confined system. This could also be due to the blocking of carriers by thick GaAs barriers between which 20 periods of Bi-QDIPs are sandwiched.

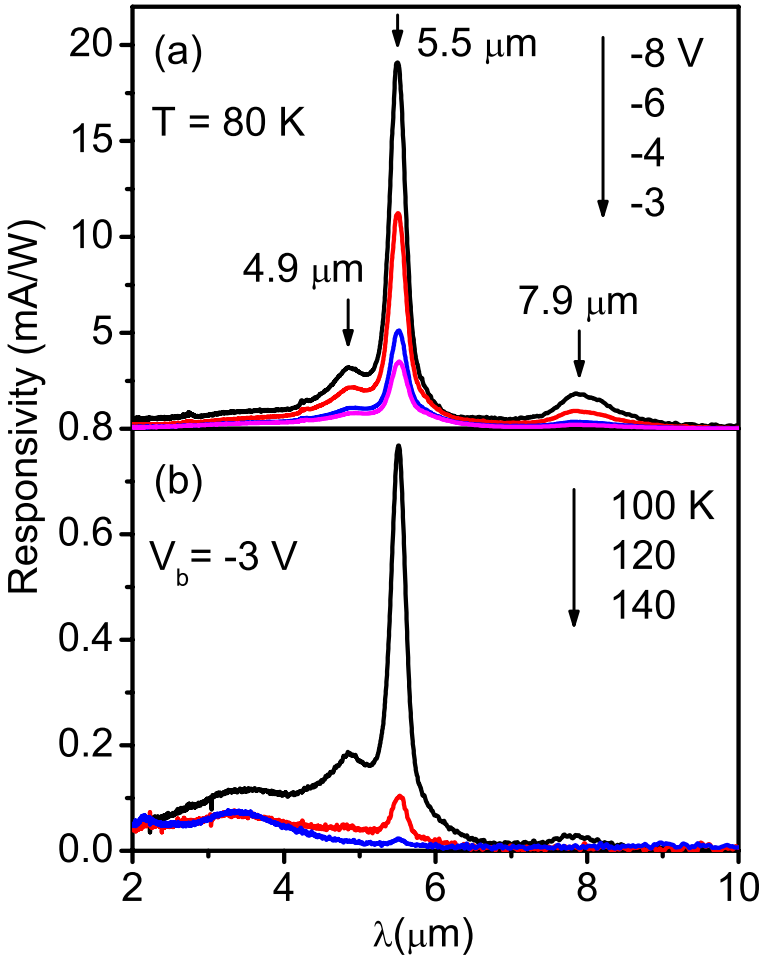

Figure 4.3: (a) Spectral responsivity of the Bi-QDIP (MG593) in the MWIR and LWIR regions under different bias values for a temperature of 80 K. (b) Variation of the response with temperature under -3 V bias.

The experimental spectral response of the detector in MWIR and LWIR regions is shown in Fig. 4.3 (a). There are two distinct peaks at 5.5 and 7.9 μm observed and these can be assigned to the transitions of electrons from the ground-state to the top most bound states in the active QDs (large) and stresser (small QDs), respectively. The intensity of the second peak (7.9 μm) is weaker than that of the first peak, and this is probably due to inter dot tunneling of ground-state carriers in the stresser-QDs. The ground-state in stresser-QDs is located at a higher level with respect to the ground-state of the active-QDs. Thus the ground-state carriers in the stresser-QDs can easily tunnel into the states in the active-QDs through the thin GaAs barrier, leaving low ground-state carrier density in stresser-QDs, and hence reducing the responsivity at 7.9 μm. The observed line-width ($\Delta\lambda/\lambda$) of 5.5 μm peak is $\sim$6%, signifying an excellent QD size uniformity in the active layer, as expected. Moreover, a broad peak is also observed at 4.9 μm, which is probably due to transitions of ground-state carriers in the active-QDs to the continuum, similar to bound-to-continuum transitions in DWELL discussed in Chapter 2. The spectral response can be observed up to 140 K, as shown in the inset to Fig. 4.3 (b). The maximum D* of $\sim 3 \times 10^9$ cmHz$^{1/2}$/W at 5.5 μm was obtained for a -8 V bias at 80 K.

As the most exciting result, a response peak in the VLWIR region (at 23.3 μm with a line width of 13%) was observed up to 140 K, as shown in Fig. 4.4. This peak is probably due to the transition of carriers from the ground-state to the first excited-state in the active-QDs. This observation is consistent with the energy spacing between the bound states in QDs. Similar results for DWELL structures[19, 67] in this wavelength region has been observed previously. The intensity of the peak is strongly dependent on the applied

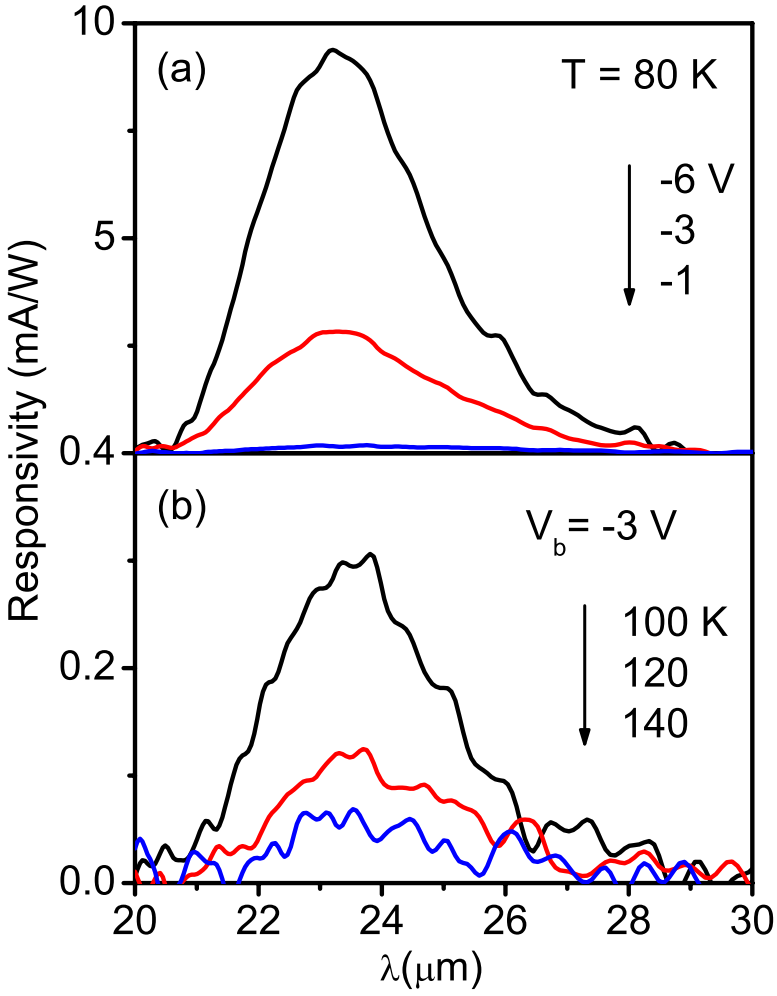

Figure 4.4: (a) VLWIR spectral responsivity of Bi-QDIP (MG593), which is due to transitions of photoexcited carriers from the ground-state to the first excited-state in the active-QDs, under different bias voltages at 80 K. (b) Variation of the response with temperature under -3 V bias.

electric field since electric field enhances field assisted tunneling of strongly bound excited carriers. Based on the band diagram shown in Fig. 4.1 (b), it is apparent that the excited carriers in the first excited-state in the active-QDs are trapped and can not escape under zero bias. When an electric field is applied, the first excited-state in the active-QDs can line up with the ground-state in the stresser-QDs, building a path for photocarriers by sequential resonant tunneling. Under this condition, an enhanced photocurrent can be observed. This is an advantage over DWELL structures where the excited carriers in the first excited-state escape to the continuum by field-assisted tunneling. Similar to the MWIR and LWIR responses, the VLWIR response can be observed up to 140 K, as shown in Fig. 4.4 (b). The optimum D* obtained at 23.3 μm is $\sim 1.2 \times 10^9$ cmHz$^{1/2}$/W under -6 V bias at 80 K.

4.3 Conclusion

A multi-color Bi-QDIP with response peaks at 4.9, 5.5, 7.9, and 23.3 μm was demonstrated. A very low dark current was observed, and the two peaks at 5.5 and 23.3 μm showed a good responsivity up to 140 K. Maximum detectivity values of $\sim$ 3 and 1.2×10^9 cmHz$^{1/2}$/W at 80 K were obtained for 5.5 and 23.3 μm response peaks, respectively. Narrow line widths ($\Delta\lambda/\lambda = 6$ and 13% for 5.5 and 23.3 μm, respectively) justify the achievement of QD size uniformity in bi-layer structures. The major advantage of this detector structure is an improved QD size distribution, which was achieved with a bi-layer structure.

Chapter 5

Homojunction Dual-Band Detectors

5.1 Introduction

Homojunction Interfacial Workfunction Internal Photoemission (HIWIP) IR detectors are formed by a highly doped emitter layer and an intrinsic layer acting as the barrier followed by another highly doped contact layer. These detectors can detect MIR-to-FIR radiation by intraband transitions in the emitter, and they can also respond to visible (VIS)-to-NIR radiation by interband transitions in the barrier. In this chapter, two HIWIP dual-band detectors constructed from GaAs and Si material systems are presented. The wavelength threshold of the interband response depends on the band gap of the barrier material, and the MIR/FIR response due to intraband transitions can be tailored by adjusting the band offset between the emitter and the barrier. Previously reported GaAs-based HIWIP FIR detectors[68, 64] have focused only on the intraband transitions leading to a response in the FIR region (λ_0 is in the 20-92 μm range). Compared to QWIPs and QDIPs, the response of HIWIPs is broad, and narrow peaks or combinations of several

peaks are not observed. This broad band response of HIWIPs is very useful for spectroscopic and space-astronomy applications. However, using resonant cavity architectures (RCAs)[69], Fabry-Perot type oscillations on the free carrier response can be obtained, where each peak represents an order of the interference pattern. Resonant cavity effects are mainly used to enhance the responsivity at desired wavelengths (cavity-peaks), and the locations of the cavity peaks can be tuned by adjusting the thickness of the layers in the structure at the device designing stage. The dual-band mechanism in HIWIPs produces two distinguishable wavelength bands (regions), where the origin of the detection mechanism of each band is independent of the other. Thus, there are several possibilities to control the response in each band independently, opening up the opportunity for potential dual-band detector applications.

While previously reported dual band[3, 70, 71, 72] and multiband[73, 18, 19, 67] detectors can detect NIR, MIR, and FIR radiation, the HIWIP detectors have the ability to detect a much wider range of photons, even covering the UV and FIR regions using a single structure. Here, the focus will be on dual-band detection using GaAs and Si based HIWIPs for detection in the NIR and FIR regions. Although the devices are not optimized for either NIR or FIR operations, both the NIR and the FIR responses together could have a high commercial appeal. However, these detector structures can be optimized for NIR and FIR detection independently, and several improvements are discussed in Chapter 6. In astronomy where IR technology plays a dominant role in observing celestial objects, the NIR response of the detector can be used to observe cooler red objects, and FIR response can detect cold objects such as comets, planets, and interstellar dust.

5.2 HIWIP Detector Structures and Dual-Band Detection Mechanism

A typical HIWIP detector structure consists of a single (or series of) doped emitter(s) followed by an undoped barrier(s), which are in turn sandwiched between two highly doped contact layers. The layer architecture of a typical multi-periodic HIWIP detector and Actual image of a detector consisting of a number of mesas (appearing as squares) are shown in Fig. 5.1. Both the emitter and barrier in a HIWIP structure are made of the same material but with different doping levels. A schematic diagram of a processed single period *p*-type HIWIP structure is shown in Fig. 5.2(a). The doped emitter layer can also act as the top-contact layer, if the doping concentration is high. In that case, an extra doped layer is not required for the top-contact. If the doping in the emitter is low, an extra layer (highly doped) is required for the top-contact, and a window is opened by etching the top-contact layer down to the emitter layer to allow IR radiation direct incidence onto the emitter, as shown in Fig. 5.2(a). Two metal contacts are deposited on the top- and bottom-contact layers, and the photocurrent is collected at these two contacts. Results have shown that this type of detector structure can lead to a dual-band response, meaning there are two response regions due to two detection mechanisms, "intraband" and "interband", which are discussed below.

The IR detection mechanism (intraband response) is a three-stage process: free carrier absorption of the incoming photons in the emitter, internal photoemission, and collection of emitted carriers by an applied electric field across the contacts. When the emitter is doped above the Mott transition level, an impurity band is formed, and for

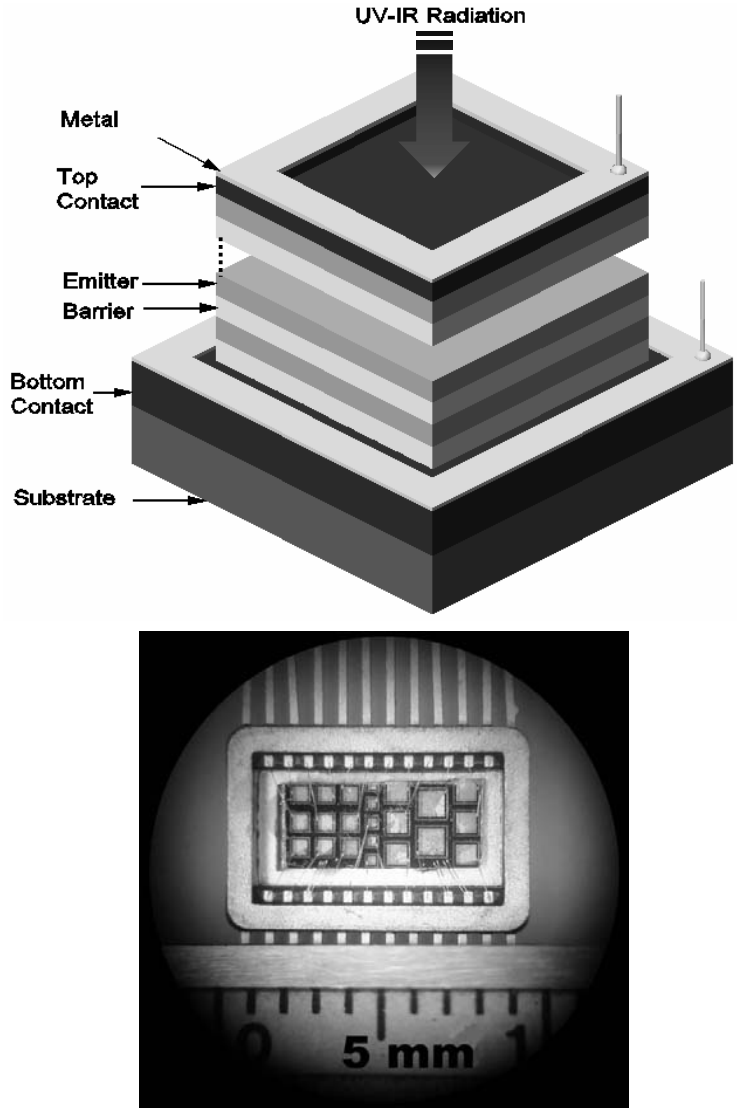

Figure 5.1: (a) Layer architecture of a typical multi-periodic HIWIP (and HEIWIP, which will be discussed in Chapter 6) detector. A series of emitter/barrier layers are sandwiched between two highly doped contact layers (top- and bottom- contact) and metal contacts are formed on the top- and bottom-contact layers. (b) Actual image of a detector consisting of a number of mesas (appearing as squares). These mesas have different electrical areas ranging from 400×400 to 1000×1000 μm^2.

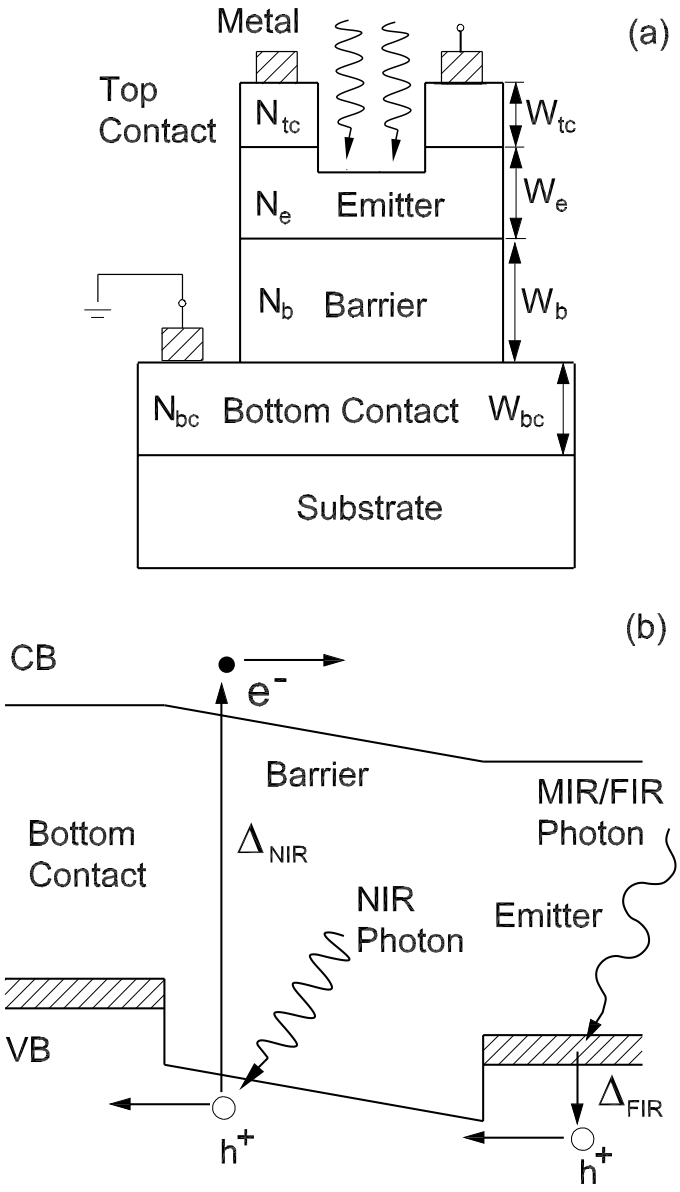

Figure 5.2: (a) Schematic structure of a HIWIP dual-band detector after processing. A window is etched out on the top-contact region for front side illumination. (b) The band diagram of a *p*-type HIWIP dual-band detector indicating both interband and intraband transitions leading to NIR and MIR/FIR responses.

a p-type (n-type) structure the Fermi level goes below (above) the valence (conduction) band edge, forming a metallic emitter layer. However, for a p-type (n-type) structure the Fermi level in the emitter still can be above (below) the valence (conduction) band edge of the barrier due to band gap narrowing in the emitter caused by high doping. A schematic diagram of conduction and valence band profiles of a p-type HIWIP detector is shown in Fig. 5.2(b). The carriers (holes for p-type and electrons for n-type) in the emitter are considered as "free carriers" since they are not confined in any direction, unlike in QWIPs or QDIPs. The ground-state carriers can be excited by incident IR radiation, and this process refers to "free carrier absorption". For the free carrier absorption, both the initial and final carrier states are part of the same continuum, resulting in a response that is inherently broadband. The limit on response wavelength (wavelength threshold) is introduced in the photoemission stage. The offset between the Fermi level in the emitter layer and the valence band edge of the barrier layer forms the interfacial workfunction Δ (Δ_{FIR} according to Fig. 5.2(b)). If the shift of the valence band edge of the emitter with respect to that of the barrier due to band gap narrowing is ΔE_V, and the Fermi level with respect to the valence band edge of the emitter is E_F, then $\Delta = \Delta E_V - E_F$. A detailed explanation is given elsewhere.[68, 74] Carriers in the emitter with sufficient energy to pass over the barrier (with energy $> \Delta$) will escape the emitter, and can be collected at the contact by an applied electric field, as shown in Fig. 5.2(b). Thus, the threshold condition arises when the photon energy is equal to Δ. The wavelength threshold λ_0 of the detector (in μm) is determined by $\lambda_0 = 1240/\Delta$, where Δ is in units of meV. By changing the doping concentration in the layers, Δ can be reduced, tailoring λ_0 to the desired value, covering

the MIR and FIR (terahertz) regions. However, there are growth limitations[68, 74] on the emitter doping concentration, which is required to form an effective workfunction.

As shown in Fig. 5.2(b), the interband response is based on the valence-to-conduction band transitions (interband transitions) in the undoped barrier. Incident NIR photons are absorbed in the barrier layer, exciting valence electrons across the band gap and generating an electron-hole pair, which can contribute to the photocurrent. These excited carriers are then collected by the applied electric field. The same process is possible in the emitter, however, the electron-hole pairs generated in the emitter would have to undergo internal photoemission before being collected, unless the electron is excited to a level above the conduction band edge of the barrier. Therefore, this process would exhibit the same threshold as for electron-hole pairs generated in the barrier. The wavelength threshold of the interband response corresponds to the band gap of the barrier material, represented by Δ_{NIR} in the figure. For GaAs and Si based HIWIP structures, the interband response thresholds fall in NIR region. The photoexcited carriers from both the intraband and interband transitions are finally swept out of the active region by the applied electric field and collected at the contacts. The two device structures presented in this chapter were designed mainly focusing on the FIR response (intraband response). However, a reasonably good NIR response (intraband response) was also observed. One drawback for effective dual-band applications is that the photocurrents generated by the two detection mechanisms are not separable without external optical filters. This aspect was considered and a possible approach is presented in Chapter 6 in order to measure simultaneously the two components of the photocurrent generated by dual-band detection without using external filters.

Material System	W_{bc} μm	N_{bc} 10^{19} cm^{-3}	W_b μm	N_b 10^{17} cm^{-3}	W_e nm	N_e 10^{18} cm^{-3}	W_{tc} nm	N_{tc} 10^{19} cm^{-3}
GaAs	1	2.0	1	1.8	200	15	120	5.3
Si	1	1-1.5	1	-	200	2-3	100	1-1.5

Table 5.1: Layer thickness (W), and doping concentration (N) of the bottom-contact (bc), barrier(b), emitter(e), and top-contact (tc), respectively, for p-GaAs/GaAs and p-Si/Si HIWIP structures. The barriers of both structures are undoped.

5.3 Experimental Results

5.3.1 NIR/FIR Dual-Band Detector Based on a p-GaAs/GaAs HIWIP Structure

The p-GaAs/GaAs HIWIP structure (RU003) was grown[64] by the OrganoMetallic Chemical Vapor Deposition (OMCVD) technique at 610 °C on a semi-insulating GaAs (100) substrate. As shown in Fig. 5.3(a), the structure consists of a bottom-contact (p^{++}) layer with 1.0 μm thickness, a barrier layer with 1.0 μm thickness, an emitter (p^{+}) layer with 0.2 μm thickness, and a top-contact layer. The top-contact and a part of the emitter layer were etched out in order to optimize the radiation absorption in the emitter, leaving an 800 Å thick emitter region (out of the original 0.2 μm layer). The layer parameters (thickness and doping level) of the sample (given in Table 5.1) were confirmed by Secondary Ion Mass Spectroscopy (SIMS). The mesas have different sizes of optical windows and the spectral measurements were carried out on a mesa with a 460 μm $\times$ 460 μm optical window (for more details, see Appendix A: Device Characterization).

The NIR spectral response due to the interband transition of carriers in the GaAs barrier layer is shown in Fig. 5.4 (a). The solid line represents the experimental curve for a -100 mV bias setting, while the dashed line represents the calculated curve based on a model[64] in which the absorption coefficient for interband transitions was calculated using the permitivity model from Ref.[75]. The threshold wavelength observed at 0.82 μm confirms the interband transition in GaAs (see Fig.5.3 (b)), with the band gap in GaAs being 1.51 eV. The optimum responsivity at 0.8 μm is $\sim$ 9 A/W, while the detectivity is $\sim 2.7\times10^{11}$ cmHz$^{1/2}$/W for a -100 mV bias and a temperature of 4.6 K. The oscillations seen in the

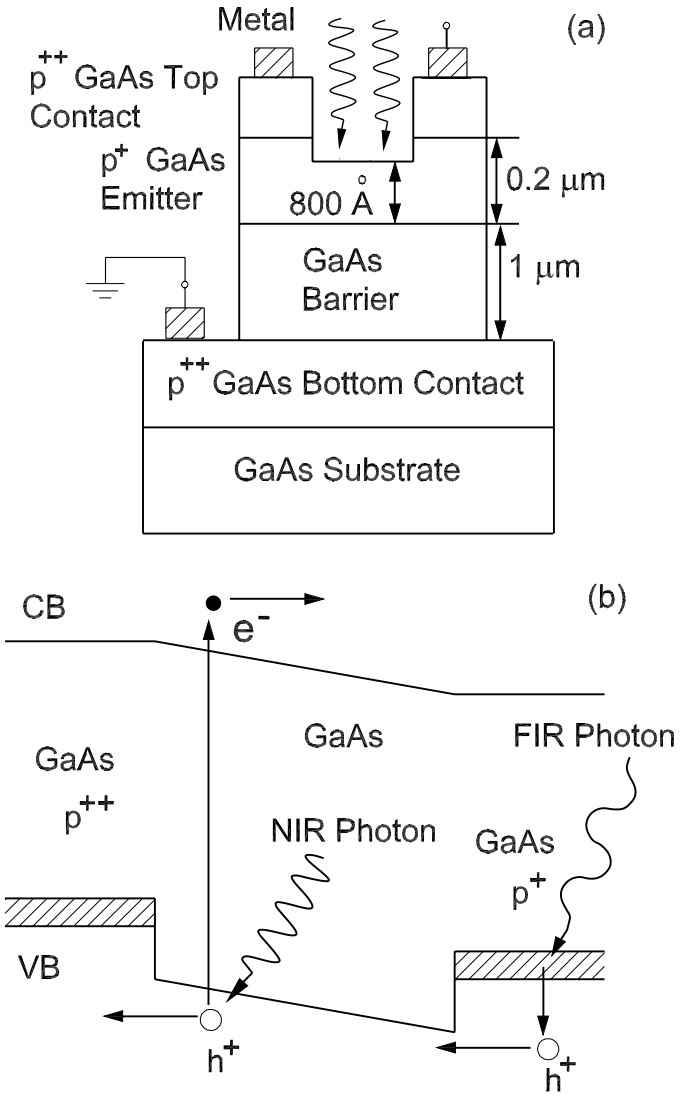

Figure 5.3: (a) Schematic diagrm of the p-GaAs single emitter HIWIP dual-band detector after processing. The top-contact, emitter, barrier, and bottom-contact have thicknesses of 0.12, 0.20, 1.0, and 1 μm, respectively. A window on the top of the device is made for front side illumination, leaving only about 800 Å as the emitter thickness. (b) Conduction and valence band profile of the dual-band structure indicating both interband and intraband transitions leading to NIR and MIR/FIR responses.

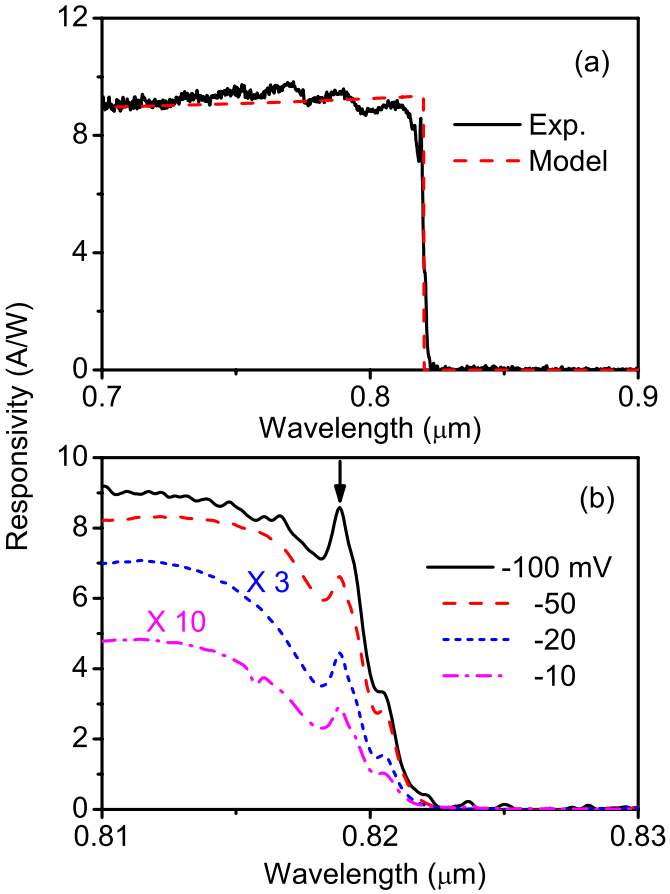

Figure 5.4: (a) Interband response of a p-GaAs/GaAs HIWIP (RU003) fitted with a model for a -100 mV bias. (b) Bias dependence of the exciton peak at the threshold edge of the experimental response curve. The curves for -10 and -20 mV bias voltages have been multiplied by 10 and 3 for clarity.

NIR region diminish with increasing applied electric field and the temperature. As shown in Fig. 5.4 (b), the weaker peak at 0.819 μm (1.514 eV) is due to excitonic[76] transitions and the amplitude of the peak increases with increasing bias.

The spectral response under different bias voltages in both NIR and FIR regions at 4.6 K is given in Fig. 5.5. The NIR response (intraband response) is observed up to 70 μm and it has a responsivity of $\sim$ 1.8 A/W and a detectivity of $\sim 5.6\times10^{10}$ cmHz$^{1/2}$/W at 57 μm for a -100 mV bias. Since the interband response is optimum at -100 mV bias, Fig. 5.5 shows the spectra for both bands only up to -100 mV bias. The oscillations observed in the MIR region are due to Fabry-Perot interference arising from the 1 μm thick GaAs barrier layer in the device structure. The sharp drop around 37 μm is due to the strong phonon absorption around the reststrahlen band of GaAs. The two peaks[64] at 57 and 63 μm arise from transitions of hydrogenic-like impurity atoms in the barrier region (from the impurity ground-state to the excited-states). These transitions show a strong bias dependence due to the fact that the carriers excited to the upper impurity states undergo tunneling through the barrier, formed by the Coulomb potential of the acceptors with the support of an externally applied field.

The spectral responsivity curves due to both interband and intraband transitions measured from 4.6 to 20 K are shown in Fig. 5.6. An optimum responsivity of $\sim$ 8 A/W and a detectivity of D*$\sim 6\times10^{9}$ cmHz$^{1/2}$/W were obtained at 0.8 μm for the interband response, while a responsivity of $\sim$ 7 A/W and a detectivity of $\sim 5\times10^{9}$ cmHz$^{1/2}$/W were measured at 57 μm, under a -100 mV bias voltage at 20 K. The responsivity of the 63 and 57 μm peaks show a strong dependence on temperature, and the 63 μm peak is relatively high at

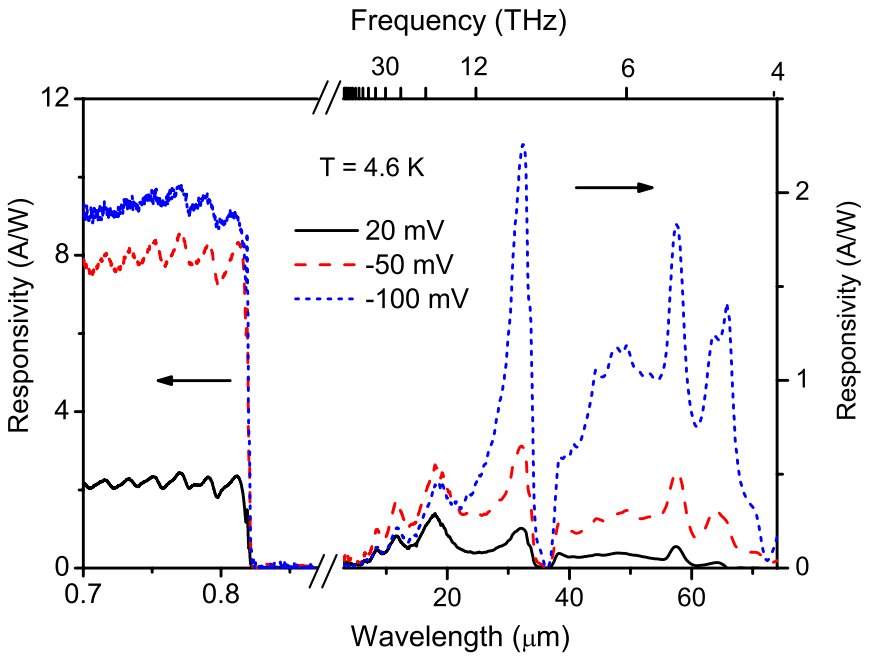

Figure 5.5: The NIR/FIR dual-band (interband and intraband) response of a p-GaAs/GaAs HIWIP (RU003) detector at 4.6 K for several different reverse bias voltages. The left and right axes correspond to NIR and FIR responsivity, respectively. Note: a break on wavelength axis at 2 μm has been made in order to expand the view in both regions.

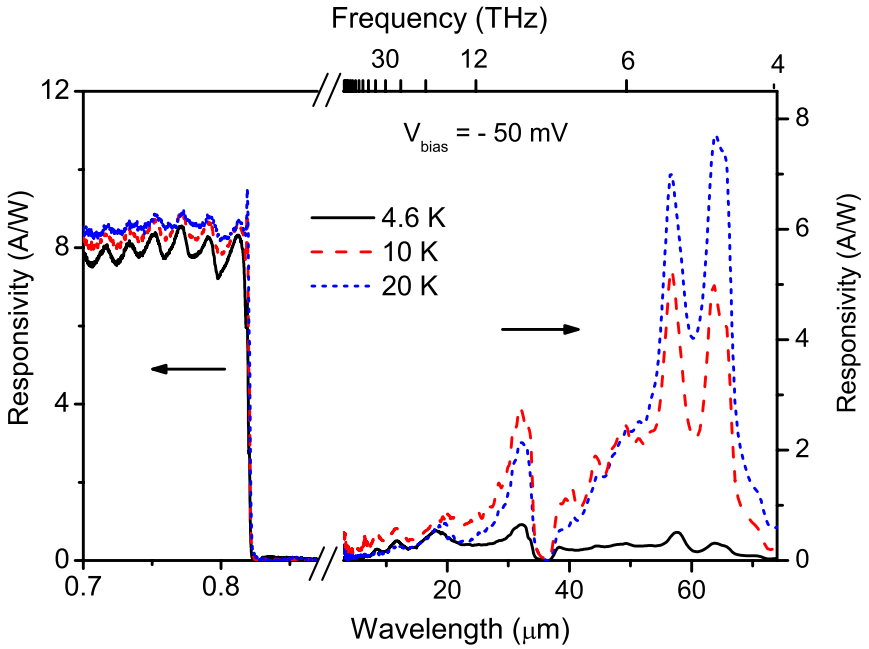

Figure 5.6: The NIR/FIR dual-band (interband and intraband) response of a p-GaAs/GaAs HIWIP (RU003) detector at different temperatures for a -50 mV bias. The left and right axes correspond to NIR and FIR responsivity, respectively. Note: a break on wavelength axis at 2 μm has been made in order to expand the view in both regions.

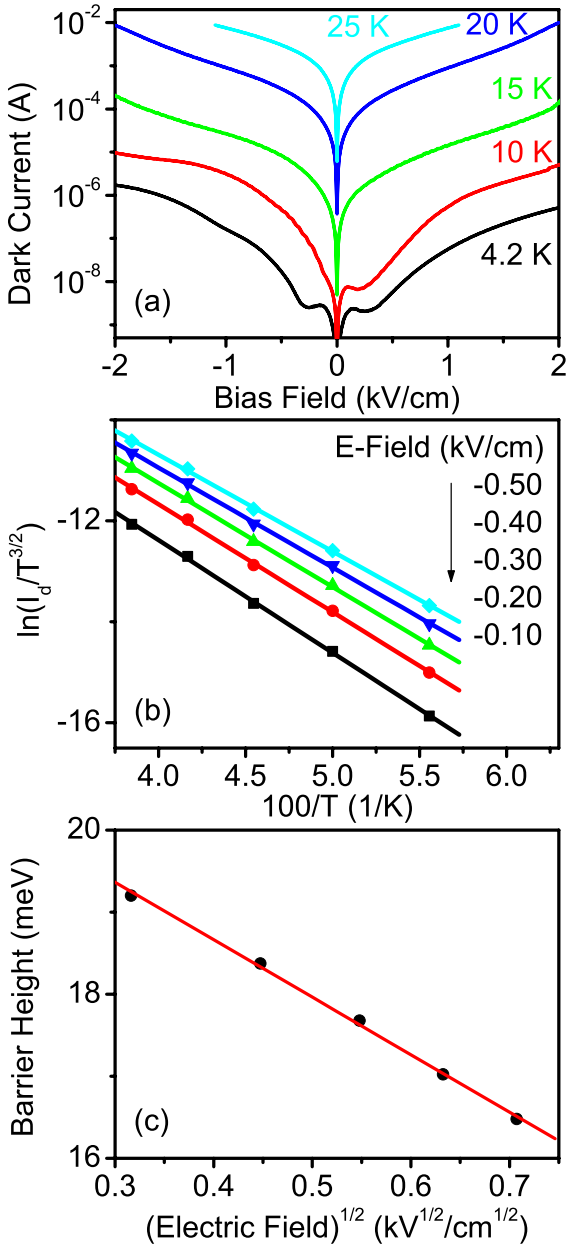

Figure 5.7: (a) I-V characteristics of the p-GaAs/GaAs HIWIP (RU003) detector at different temperatures under dark conditions. The asymmetry in the I-V curves is probably due to the asymmetry in the structure. (b) Arrhenius plot under different electric fields. (c) The variation of the calculated effective barrier height based on the Arrhenius plot as a function of the applied electric field.

higher temperatures. This is caused presumably by the increased rate of collecting carriers excited to the upper states from the impurity ground-state. If the rate of collection of excited carriers by the external circuit is low, than the excited carriers will either relax back to the ground-state or occupy the excited-states resulting in a high population density. At high temperature, the rate of collection of excited carriers over the barrier can be enhanced by the thermal energy leading to enhanced responsivity.

The variations of the dark current at different temperatures are given in Fig. 5.7(a). The asymmetry in the I-V curve is due to the asymmetry in the structure. Arrhenius plots under different electric fields are shown in Fig. 5.7(b) and the symbols represent the experimental data, while solid lines represent the linear fit. The effective barrier height (Δ) can be calculated from the slope of the fitted lines. As shown in Fig. 5.7 (c), a dependence of effective barrier height on the square root of applied field was observed. The fitted line denotes that the effective barrier height has a linear relationship with the square root of applied electric field. Δ increases with the applied bias[68] giving rise to an increasing threshold with bias. For a 0.20 kV/cm field, Δ is 18.4 meV which corresponds to a 67.5 μm threshold, and similarly for a 0.50 kV/cm field, Δ is 16.5 meV, giving a 75 μm threshold. These results are consistent with the spectral response curves shown in Fig. 5.5.

5.3.2 NIR/FIR Dual-Band Detector Based on a p-Si/Si HIWIP Structure

A p-Si/Si (HIWIP) detector (Sample:79) sensitive to NIR and VLWIR radiation is discussed in this section. In comparison with the GaAs dual-band detector[77] reported in the previous section, this detector has an extended NIR response (up to 1 μm) and a continuous IR response from 5-35 μm with a peak at 25 μm. Commercially available Si detectors with a

response in the range 5-30 μm are operated at 4.2 K, and have a responsivity of 2 A/W. Si BIB[78] detectors have a responsivity of 32 A/W at an operating temperature of 7 K and foa a wavelength of $\sim$ 30 μm, and previously demonstrated Si HIWIP detectors[79] have shown a responsivity of 12.3 A/W at 27.5 μm with a detectivity of 6.6×10^{10} cmHz$^{1/2}$/W at 4.2 K. As a VLWIR detector, this device can be operated at 4.6 K with a responsivity of 1.8 A/W and a detectivity of $\sim1.2\times10^{11}$ cmHz$^{1/2}$/W at 25 μm for a -1 V bias. It also operates up to 30 K with a background limited infrared performance (BLIP) temperature of 25 K for a $\pm$0.9 V bias.

The structure (Sample:79) was grown by OMCVD on a Si substrate, and consists of a *p*-doped Si bottom-contact, an undoped Si barrier, a *p*-doped Si emitter layer, and a *p*-doped Si top-contact layer, as shown in Fig. 5.8(a). Boron was used as the p-type dopant. The devices were processed and a mesa with an electrical area of 400 $\times$ 400 μm^2 was used for characterization. The layer parameters (thickness and doping level) of the sample are given in Table 5.1. Although the Si barrier is not intentionally doped, a slight doping is expected due to dopant migration from the emitter. These dopant atoms in the barrier act as Hydrogenic-like impurities, in which a series of transitions between energy levels may take place leading to tiny photoresponse peaks[80]. Further discussion about the impurity transition peaks will be given in the following sections.

The NIR response for a -1 V bias shows a threshold at $\sim$1.05 μm, which is in accordance with $\sim$1.17 eV bandgap of Si at 4.6 K, as shown in Fig. 5.9(a) and (b). The two arrows in the figure mark the positions of the E_1^{TO}, E_2^{TO}absorption bands, which are due to TO-phonon assisted exciton transitions at the band edge.[81] E_1^{TO} is observed at 1.21

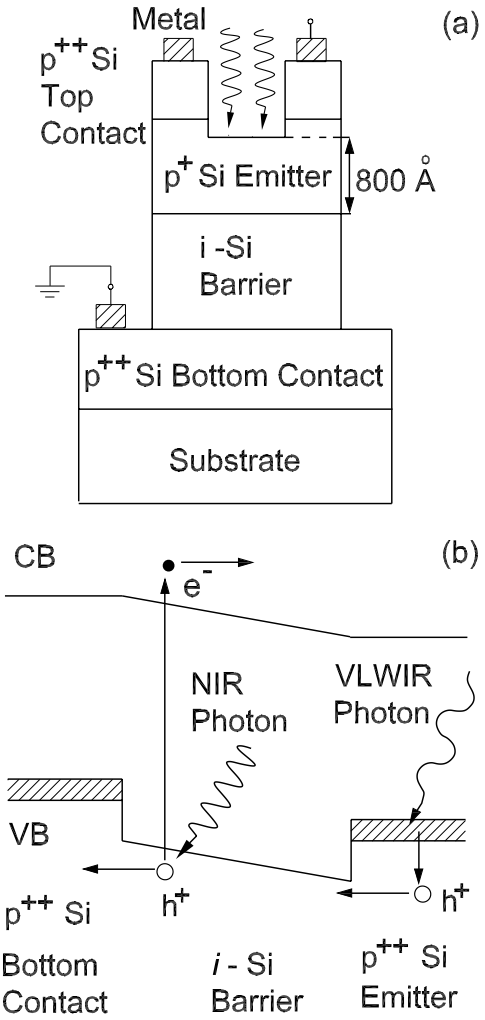

Figure 5.8: (a) Schematic diagram of the *p*-Si/Si HIWIP (Sample:79) structure. The doping concentration of the Si emitter is 2.5×10^{18} cm^{-3}, while the contacts are doped to 1.5×10^{19} cm^{-3}. The Si barrier is not intentionally doped. The thicknesses of the top-contact, emitter, barrier, and bottom-contact layers are 0.1, 0.2, 1, and 1 μm, respectively. (b) Band diagram showing the conduction and valence band (CB, and VB) profile of the structure.

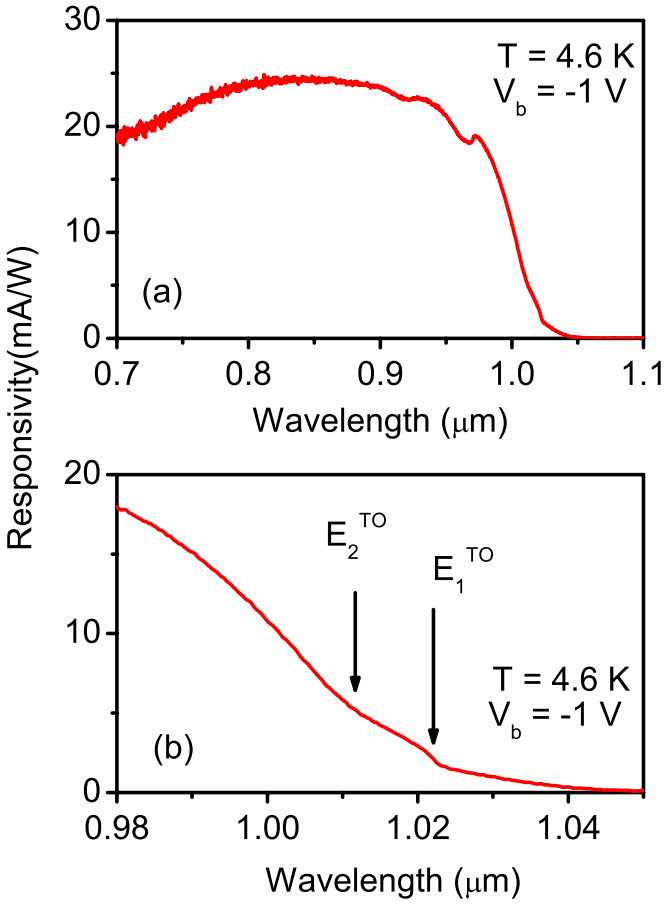

Figure 5.9: (a) NIR response ofthe p-Si/Si HIWIP (Sample:79) detector measured at 4.6 K. (b) Expanded view of the NIR response at the band edge. The two arrows in the figure mark the position of the E_1^{TO}, E_2^{TO}absorption bands, which are due to TO-phonon assisted exciton transitions at the band edge.

eV and the separation between E_1^{TO} and E_2^{TO} is less than 2 meV. Hence E_2^{TO} cannot be observed clearly in the photoresponse curve. A responsivity of 0.024 A/W is obtained at 0.8 μm with a detectivity of $\sim 1.7 \times 10^9$ cmHz$^{1/2}$/W at 0.8 μm for a -1 V bias at 4.6 K.

As shown in Fig. 5.10 (a), the VLWIR response arising from intraband transitions (see Fig. 5.8) at 4.6 K is in the range of 5-35 μm. The threshold wavelength observed for a -0.5 V bias is 32 μm, and the corresponding value of Δ = 38.7 meV is in good agreement with the theoretical model[64]. Arrhenius calculations based on the dark current also confirm this value of Δ. The threshold wavelength increases with the applied bias as shown in Fig. 5.10 (a) and (b). This is a result of decreasing Δ with increasing bias.[74] The photoresponse shows a strong bias dependence mainly due to field-assisted tunneling of photoexcited carriers. The responsivity values at 25 μm and -0.5, -1 and -1.5 V bias voltages are 0.90, 1.78, and 31.0 A/W, respectively. When the bias is increased further, a rapid improvement of the photoresponse can be observed, and Fig. 5.10 (b) shows a responsivity of 157 A/W at 25 μm for a -2 V bias, which translates to a conversion efficiency of 780%. Highly sensitive NIR detectors with a high internal gain have been observed previously[82, 83]. Applying a high electric field across the structure enhances the process of impact ionization within the barrier, introducing a gain into the photocurrent.[84] While contributing to the photocurrent, carriers excited by photons with an energy greater than Δ can ionize impurity atoms in the barrier, which are confined in a weak Coulomb potential. As a result, more than one carrier per photon can be generated. This type of gain mechanism is possible if the barrier contains impurity atoms. The observation of impurity transition peaks to be discussed later is evidence for the existence of impurities

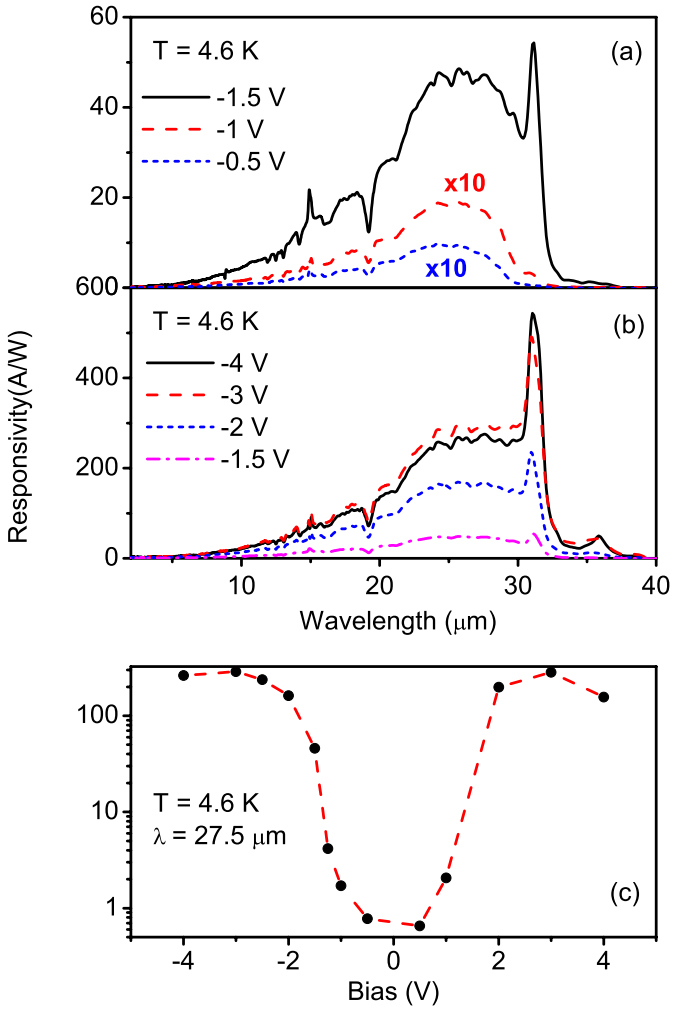

Figure 5.10: VLWIR response of the *p*-Si/Si HIWIP (Sample:79) detector at 4.6 K for bias voltages in the range (a) -0.5 V to -1.5 V (b) -1.5 V to -4 V. The curves at -1 and -0.5 V biases have been multiplied by 10. (c) Variation of responsivity with applied bias. Applying a high electric field across the structure enhances the process of impact ionization within the barrier, introducing a gain into the photocurrent. Thus, the extremely high observed responsivity for high bias voltages is due to the enhancement of the photocurrent by impact ionization.

in the barrier. Despite the high responsivity obtained at high bias voltages, the optimum detectivity observed is $\sim 1.5\times10^{11}$ cmHz$^{1/2}$/W for a -1 V bias. This is due to an increase of the noise current with bias. Moreover, Fig. 5.11 (a) and (b) show the variation of the detectivity at 25 μm with applied bias voltage at 4.6 K and with temperature for a -1 V bias, respectively. The behaviour of the detectivity with temperature is typical for most of IR devices since the noise current increases with temperature.

The dual-band response can be obtained up to 30 K as shown in Fig. 5.12. At a -1 V bias and 30 K, the responsivity, quantum efficiency, and detectivity at 0.8 μm are $\sim$0.30 A/W, 46 %, and $\sim 6.7\times10^{8}$ cmHz$^{1/2}$/W, while at 25 μm they are 1.4 A/W, 7 %, and $\sim 3.1\times10^{9}$ cmHz$^{1/2}$/W, respectively. The quantum efficiency can be improved by using a multi-periodic design and incorporating a RCA[69] into the structure. The sharp peaks (labeled as A, B, C, and D) superimposed on the free carrier response become dominant at 30 K. These peaks can be fitted with the impurity transitions of Boron in Si. The intensity of the transition increases with temperature[85] as the efficiency of the photo-thermal mechanism leading to the excitations increases with temperature. The enhanced response at 30 K and the appearance of the peak A (30.7 meV) at 30 K, which is not visible at 4.6 K, confirm that the relative intensity of the impurity peaks increases with temperature. Merlet et al.[80] compared the positions of the peaks reported by several other researchers. In Fig. 5.12, the peaks A, B, C, and D observed at 30.7, 34.4, 38.3, and 39.6 meV has been previously reported at 30.37, 34.50, 38.38, and 39.63 meV, respectively, by Merlet et al. The deviation of the energy values fall within the spectral resolution. A theoretical calculation of acceptor states of Si along with experimental results have been presented by Onton et

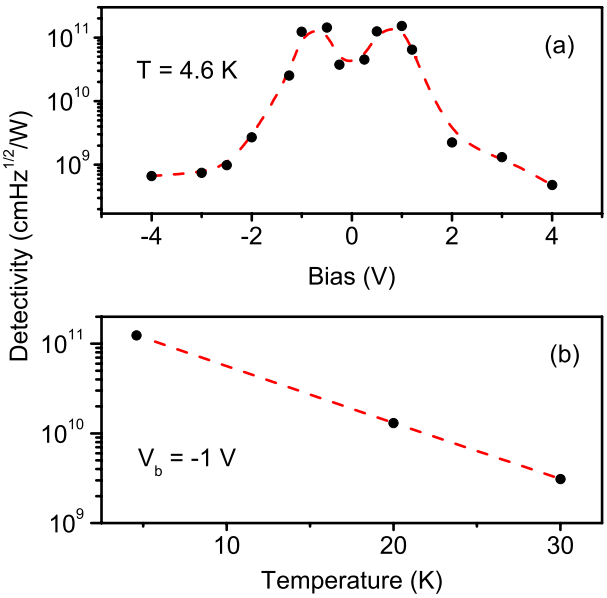

Figure 5.11: (a) Detectivity of the p-Si/Si HIWIP (Sample:79) detector at 25 μm under different bias voltages at 4.6 K. Despite the high responsivity observed at high bias voltages, the detectivity decreases with increasing bias. This variation is due to the drastic increase of noise current with increasing bias voltage. (b) Variation of the detectivity with temperature.

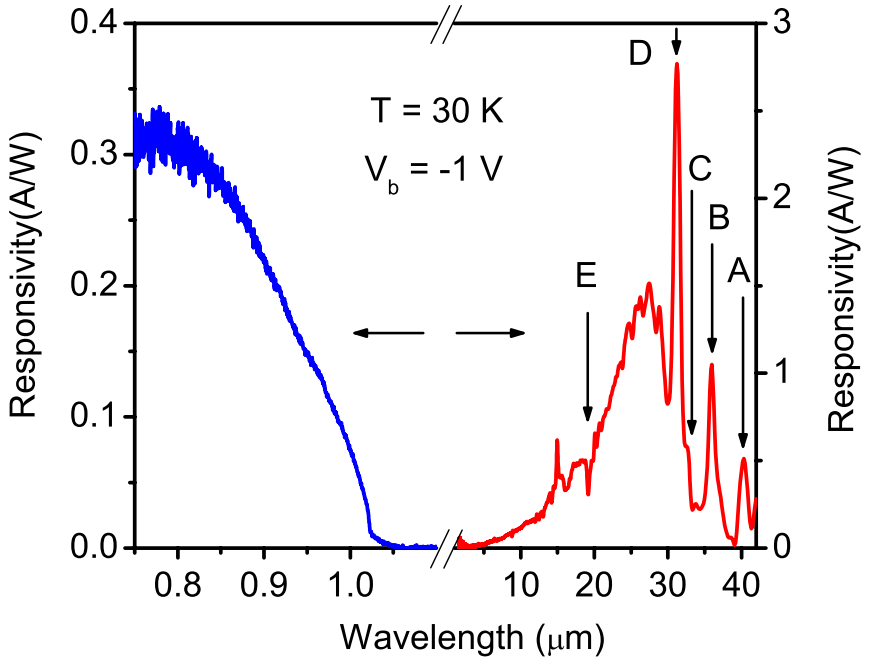

Figure 5.12: NIR/VLWIR dual-band response of the *p*-Si/Si HIWIP (Sample:79) detector measured at 30 K under -1 V bias. The arrows indicate the positions of impurity transitions of Boron in Si (A, B, C, and D), and the absorption due to the optical phonon in Si (E).

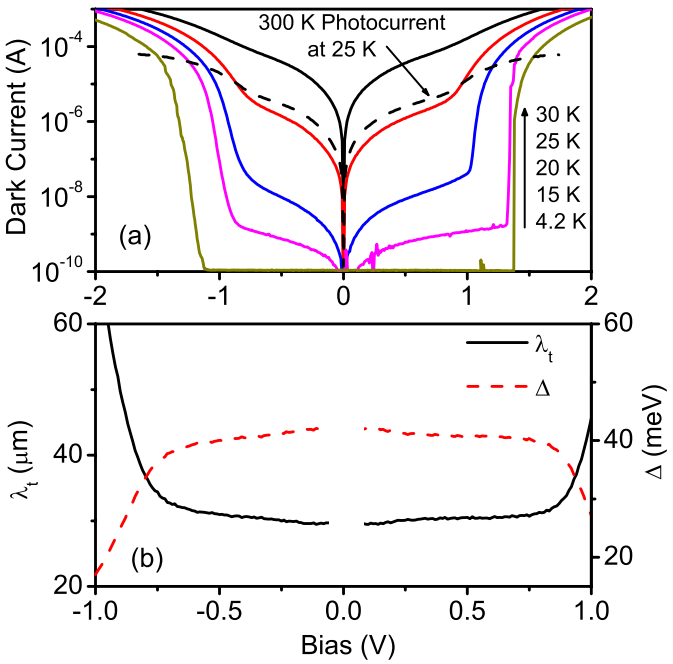

Figure 5.13: (a) Dark I-V characteristics of the p-Si/Si HIWIP (Sample:79) detector at different temperatures. The 300 K background photocurrent curve at 25 K is also shown. (b) Calculated activation energy (Δ), and corresponding threshold wavelength (λ_t) with bias, based on the Arrhenius model.

al.[86] Furthermore, the small absorption dip around 19 μm is due to the optical phonon of Si, which has been observed at 63 meV (19.6 μm).

The dark I-V characteristic curves at different temperatures and the 300 K background photocurrent measured at 25 K are shown in Fig. 5.13 (a). Dark current increases drastically possibly due to hopping conduction[79] beyond a bias of ± 1 V (an electric field of 10 kV/cm). Based on the dark and the 300 K background photocurrent measurements at different temperatures, performed using a closed-cycle refrigerator with a cold shield at 70 K and under 60° field-of-view (FOV), the BLIP temperature at ± 0.9 V was determined as 25 K. The activation energy (Δ) was calculated using the Arrhenius model, and the variation of the calculated Δ and the corresponding λ_t with applied bias are shown in Fig.5.13 (b). The calculated λ_t is in good agreement with the observed threshold in the bias range from -0.75 to 0.75 V. Beyond this region, the dark current from tunneling dominates the thermal current, as seen in the I-V characteristic curves. As a result, the Arrhenius model diverges under high applied bias voltages, resulting in invalid values for Δ.

5.4 Conclusion

HIWIP dual-band structures based on p-GaAs/GaAs and p-Si/Si, which can detect NIR and MIR/FIR radiation were demonstrated. Based on a theoretical model and experimental data, the transitions in the structures giving rise to NIR and MIR/FIR responses can be determined. The NIR response can be explained in terms of interband transitions in the undoped GaAs and Si barrier layers in the two structures, and the NIR wavelength thresholds correspond to the bandgaps of GaAs and Si. The FIR response arises due to

free carrier absorption and intraband transitions in the emitter. The high performance of the detector demonstrates the potential for applications where detection in both NIR and MIR/FIR is important. Using different material systems such as GaN/AlGaN instead of GaAs or Si based systems can extend the detection capability of the detector into the UV range, providing a dual band detector covering UV and FIR regions (see Chapter 6). In addition, the impurity transitions of Boron in Si were confirmed based on the spectral response of a Si-based HIWIP detector.

Chapter 6

GaN-Based Heterojunction Dual-Band Detectors

6.1 Introduction

Detectors based on the GaAs/AlGaAs material system were of interest for developing IR devices during the past few decades. GaAs/AlGaAs detectors covering a wide range from NIR-to-FIR[72, 87, 65, 63] have been developed using different concepts and techniques. Due to the rapid development of group III-As based device structures, mainly detectors, lasers[88], and focal plane arrays,[10, 89, 90] the optimization of device structures has been readily achieved. Further improvements may require the use of other material systems, which have advantages in different regions compared to the GaAs/AlGaAs system. Presently, as a group III-V material, GaN has attracted the interest of the scientific community for the development of wide bandgap electronic and optoelectronic devices. UV detectors,[91, 92] UV light emitting diodes,[93, 94, 95] and laser diodes[96] have been successfully demonstrated, and

are widely available for commercial applications such as flame detection, UV imaging, solar UV detection, as well as applications for industries such as those focusing on military, agricultural, and automotive products. In the IR range, researchers have reported GaN/AlGaN Schottky photodiodes,[97] and QWIPs.[98] In the FIR region, one advantage of GaN-based detectors over GaAs based ones is that the reststrahlen region of GaAs can be accessed with GaN, gaining a broad response from 20 μm and above. Moreover, GaN shows radiation hardness and the wide band gap of GaN reduces interband tunneling compared to the case of GaAs based devices. Also the higher effective electron mass for GaN will reduce the thermal emission. However, the development of GaN high speed optoelectronic devices with improved performance is still in its infancy since the growth of high-quality GaN/AlGaN heterostructures is limited by the availability of suitable lattice-matched substrate materials and by the process/material knowledge base. In this chapter, HEIWIP detectors[99, 100] based on GaN/AlGaN heterostructures, which can be operated in both UV and IR regions, are presented. Detecting multiple wavelength bands with a single detector has a number of advantages as discussed before. So far, several dual-band detectors[72, 3, 71] based on group III-As material systems (GaAs, AlAs, and InAs), operating in NIR, MIR, VLWIR, and FIR regions have been reported. In Chapter 5, homojunction device structures based on GaAs[77] and Si[101] having a dual-band response in NIR and VLWIR wejre discussed. GaN-based dual-band detectors[102] already demonstrated can detect UV and NIR radiation. UV/IR dual-band detectors are particularly useful in applications where the detection of both the UV and IR radiation is important. One example is fire and flame detection where fires emit radiation from the UV to the IR, and different flames such as hydrogen and coal have

significant intensity variation in their emission spectrum in the UV and IR regions.

Two preliminary GaN/$Al_xGa_{1-x}N$ HEIWIP detectors (denoted as 1158 and 1547) with different Al fractions in the barrier (0.026 and 0.1) were analyzed and results demonstrates the UV/IR detection capability. In a manner similar to HIWIPs, the UV detection is due to an interband transition process, while the MIR/FIR detection is from free carrier absorption in the emitter/contact followed by internal photoemission over the barrier at the GaN/AlGaN interface. In a HEIWIP structure, the emitter and the barrier are made of materials with different bandgaps (in HIWIPs, both the emitter and the barrier are made of the same material). The work function is defined as $\Delta = \Delta_d + \Delta_x$, where Δ_d is the contribution from bandgap narrowing due to a doping difference between emitter and barrier (similar to HIWIP) and Δ_x is the band offset due to different materials in the emitter and the barrier. Thus, compared to HIWIPs, HEIWIP dual-band structures have a higher flexibility to adjust the response wavelength region in both bands. The UV detection, which was observed over a temperature of 300 K to 4.2 K, has a threshold of 360 nm with a peak responsivity of 1-15 mA/W at 300 K. The detectors show a free carrier IR response in the 3-8 and 8-14 μm ranges for operating temperatures up to 120 K. In addition, this work demonstrates that 54 μm (5.5 THz) detection is possible based on the 1s-2p$\pm$ transition of Si donors in GaN. There is also a response in the range 7-14 μm, which is tentatively assigned to transitions from C impurities and N vacancies in the barrier region. Moreover, a flat response in the 30-300 μm range, which is visible only at low temperature (4.2-6 K), is also observed. Several possible explanations for this observation are given later in this chapter.

A comparison between the IR absorption of a 1 μm thick GaAs film on a GaAs substrate and a GaN film on a sapphire substrate is shown in Fig. 6.1. Both films are n-doped to a density of 5×10^{17} cm^{-3}. The absorption calculation was carried out considering both the film and the substrate. The absorption is higher in the region above 40 μm for GaN compared to GaAs even though the absorption coefficient of GaAs is higher than GaN. This absorption is due to the high reflection at the GaN-Sapphire interface. Due to strong TO phonon-photon interactions and phonon absorption, there is a deep valley at $\sim$18 μm in the responsivity curve of a GaN/AlGaN detector ($\sim$37 μm for GaAs/AlGaAs). The GaN/AlGaN detectors reported in this chapter are not optimized to have the best performance in either UV or IR regions. The response of the present single period detectors can be significantly enhanced by incorporating multi-periods of emitter/barrier layers. In comparison with a GaAs/AlGaAs HEIWIP detector[103] with multi-periods responding in 5-20 μm range, the reported GaN/AlGaN detector has a higher response even with a single period. However, the detectivity is lower than the GaAs/AlGaAs detector. This could be due to the increased dark current (also the increased noise current) as a result of the response at 54 μm due to the transitions of Si impurity atoms in GaN, which will be discussed in detail.

In order to improve the performance of the detector in UV and IR regions, several approaches are also addressed. For an effective UV/IR dual-band detection capability, the two components of the photocurrent generated by UV and IR mechanisms should be separable and measured simultaneously. In order to test this, a measurement setup capable of performing simultaneous UV and IR photocurrent measurements was built. Finally, a

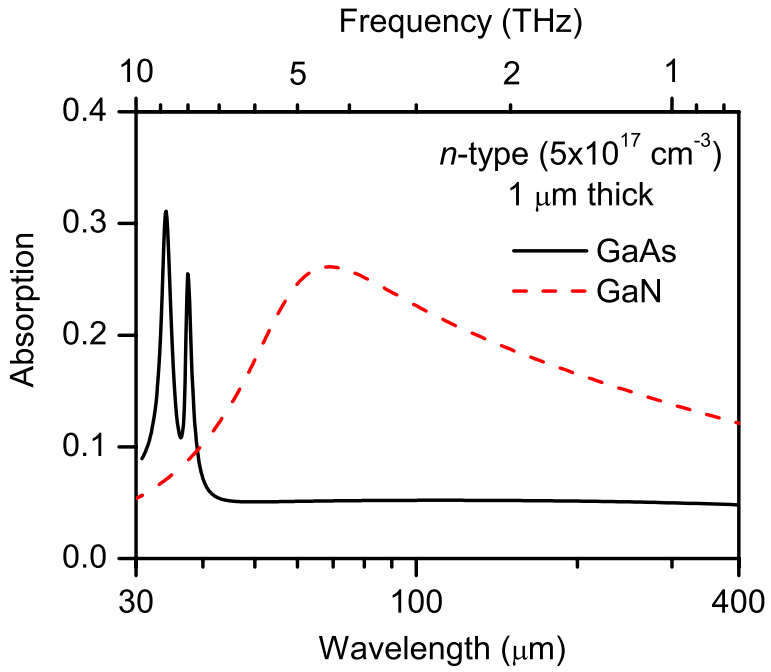

Figure 6.1: A comparison of the calculated IR absorption of 1 μm thick 5×10^{17} cm^{-3} n-doped GaAs and GaN films in the IR region. The absorption calculation was carried out considering both the film and the substrate. Due to higher absorption in the region above 40 μm, GaN would be a good candidate for FIR detector development.

dual-band detector design, which allows not only the measurements of the two components of the photocurrent generated by UV and IR radiation simultaneously, but also optimizes the UV and IR responses independently, is proposed.

6.2 GaN/AlGaN Structures: Growth and Experiment

The HEIWIP structure was grown by OMCVD on a sapphire substrate, and it consists of a Si doped n^+ GaN emitter layer (which also serves as the top-contact), an undoped $Al_xGa_{1-x}N$ barrier, and an n^+ GaN bottom-contact layer, as shown in Fig. 6.2 (a). The thickness and the doping density of the GaN emitter, and the GaN bottom-contact are 0.2 μm, 5×10^{18} cm^{-3}, 0.7 μm, and 5×10^{18} cm^{-3}, respectively, and the thickness of the undoped $Al_xGa_{1-x}N$ barrier is 0.6 μm. Two preliminary detectors have the same structure except the Al fraction in the barrier (x), which is 0.026 for 1158 and 0.1 for 1547. The structures were processed to form square mesa elements with different active areas by dry etching techniques. The ohmic contacts were formed by deposition of Ti/Al/Ti/Au (metalization) on the top- and bottom-contact layers. After the metalization, the device structure was annealed under a N_2 gas flow at 700 °C temperature for two minutes. The annealed sample was mounted on chip carriers and wire bonds were made from each mesa of the sample to the chip carrier.

Dark I-V measurements were performed using a Keithley 2400 source meter on all the mesas of the sample in order to check for uniformity of the structure. The spectral response of the detector in the UV region was obtained using an Oriel Deuterium UV source, UV/VIS monochromator, and neutral density filters, and spectra were calibrated using a

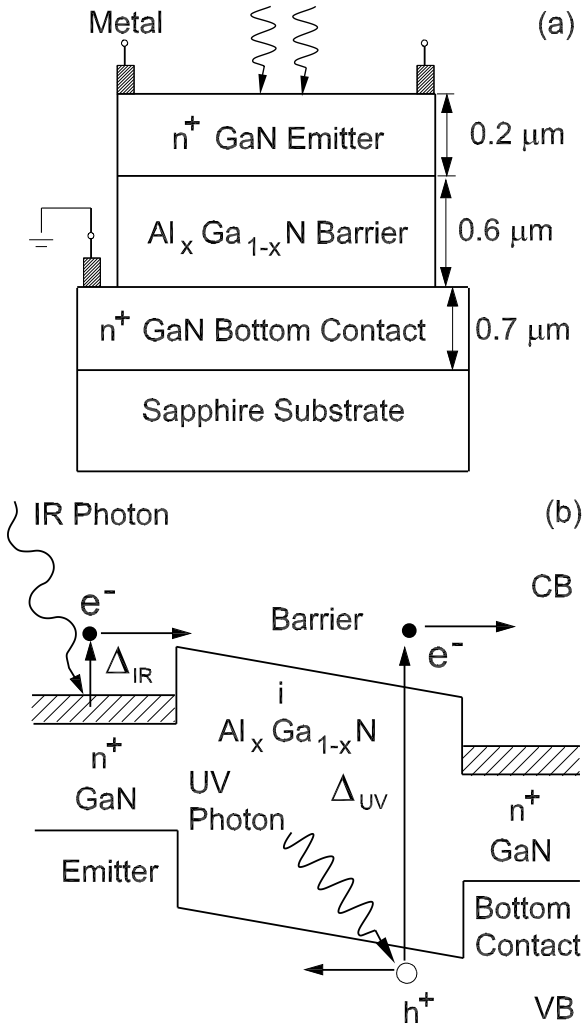

Figure 6.2: (a) Schematic diagram of the GaN/AlGaN HEIWIP structure. The doping concentration of the GaN emitter is 5×10^{18} cm^{-3}, while the GaN bottom-contact is doped to 5×10^{18} cm^{-3}. The AlGaN barrier is not intentionally doped. By design, the Al fraction of $Al_xGa_{1-x}N$ is 0.026 for 1158 and 0.1 for 1547. (b) Band diagram showing the conduction/valence band (CB/VB) profile of the structure and the transitions leading to UV/IR dual-band responses.

background spectrum obtained by a Hamamatsu photomultiplier tube with a known sensitivity. Spectral measurement in the IR region for normal incidence radiation was carried out by using a Perkin Elmer System 2000 Fourier Transform Infrared (FTIR) spectrometer. The spectra were calibrated relative to a background spectrum obtained by a Si composite bolometer with the same set of optical components (for more details, see Appendix A: Device Characterization).

The dual-band detection involves two detection mechanisms. The energy band diagram indicating the transitions due to both mechanisms is depicted in Fig. 6.2 (b). The UV detection is based on interband transitions of carriers in the $Al_xGa_{1-x}N$ barrier, while the IR response is due to free carrier absorption (intraband) followed by internal photoemission in the emitter/barrier junction. More details are given in the following sections.

6.3 UV Responsivity Modeling

The UV spectral response is due to interband transitions of carriers in the AlGaN barrier layer. The theoretical UV response is obtained based on a model[64] in which the absorption coefficient for interband transitions was calculated using the permittivity model in Ref.[104, 105] with the appropriate parameters for AlGaN given in the same references. The dielectric function associated with the interband transition can be approximated by

$$\epsilon(E) = \epsilon_0(E) + \epsilon_{0E}(E) + \epsilon_1(E) + \epsilon_{1E}(E) + \epsilon_\infty, \tag{6.1}$$

where $\epsilon_0(E)$ and $\epsilon_{0E}(E)$ are the contribution from 3D critical point E_0 and exciton contribution at E_0, respectively. The contribution from $E_{1\beta}$ ($\beta = A$, B, and C) critical points

and excitons at $E_{1\beta}$ are given by $\epsilon_1(E)$ and $\epsilon_{1E}(E)$, respectively. The additive constant is denoted by ϵ_∞. The terms are given by

$$\epsilon(E) = AE_0^{-3/2}\chi_0^{-2}[2-(1+\chi_0)^{1/2}-(1-\chi_0)^{1/2}], \tag{6.2}$$

with

$$\chi_0 = \frac{E+i\Gamma'_0}{E_0}, \tag{6.3}$$

A and Γ'_0 are the strength and damping constants of E_0 transition, respectively.

$$\epsilon_{0E}(E) = \sum_{m=1}^{\infty} \frac{A_0^{ex}}{m^3} \frac{1}{E_0 - (G_0^{3D}/m^2) - E - i\Gamma'_0}, \tag{6.4}$$

where A_0^{ex} and G_0^{3D} are the 3D exciton strength parameter and binding energy.

$$\epsilon_1(E) = -\sum_{\beta=A,B,C} B_{1\beta}\chi_{1\beta}^{-2}\ln(1-\chi_{1\beta}^2), \tag{6.5}$$

with

$$\chi_{1\beta} = \frac{E+i\Gamma'_{1\beta}}{E_{1\beta}}, \tag{6.6}$$

$B_{1\beta}$ and $\Gamma'_{1\beta}$ are the strength and damping constants of $E_{1\beta}$ transitions, respectively.

$$\epsilon_{1E}(E) = \sum_{\beta=A,B,C}\sum_{m=1}^{\infty} \frac{B_{1\beta}^X}{(2m-1)^3} \frac{1}{E_{1\beta} - [G_{1\beta}^{2D}/(2m-1)^2] - E - i\Gamma'_{1\beta}}, \tag{6.7}$$

where $B_{1\beta}^X$ and $G_{1\beta}^{2D}$ are the strength parameters and binding energy at $E_{1\beta}$, respectively. The frequency dependent damping constant is given by

$$\Gamma'_j(E) = \Gamma_j \exp[-\alpha_j(\frac{E-E_j}{\Gamma_j})^2], \tag{6.8}$$

where $j = 0,\ 1A,\ 1B,\ 1C$; Γ_j is the frequency independent damping constant and α_j is a broadening parameter. More details on the model and values of the parameters can be found in Ref.[105]

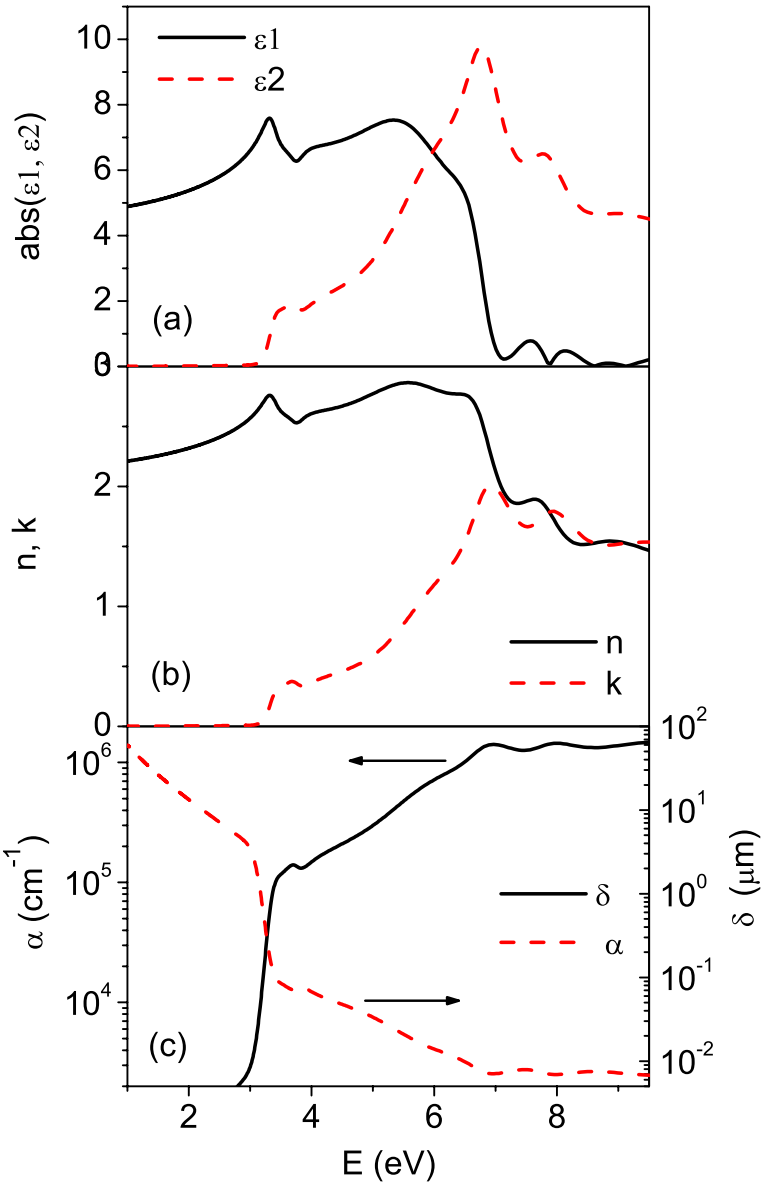

Figure 6.3: (a) Real/imaginary parts of the dielectric function, (b) refractive index and extinction coefficient, and (c) absorption coefficient and optical skin depth (the distance at which the intensity falls to 1/e of its original value), calculated for hexagonal GaN, based on the model dielectric function.

The optical electrical field strength is then calculated from the transfer matrix approach[64] and the absorption is determined from the Poynting vector and the imaginary part of the permittivity. The model assumes that all excited carriers should escape and be collected.

The calculated real/imaginary parts of the dielectric function, refractive index/extinction coefficient, and absorption coefficient/optical skin depth (the distance in the medium at which the intensity of the optical field reduced by a factor of 1/e compared to the incident intensity) are given in Fig. 6.3 (a), (b), and (c), respectively. The calculated and experimentally measured responsivity for the 1158 detector (to be described later) at a -0.5 V bias are shown in Fig. 6.4 (a). (For implementation of the model, see Appendix C)

The bandgap of the $Al_xGa_{1-x}N$ alloy is given by,[106]

$$E_g(eV) = 6.13x + 3.42(1-x) - 1.08x(1-x), \tag{6.9}$$

where x is the Al fraction in the $Al_xGa_{1-x}N$ alloy. The wavelength threshold of interband transitions λ_{0g} (in nm) is given by $\lambda_{0g} = 1240/E_g$ with E_g in eV.

6.4 IR Responsivity Modeling

The band diagram indicating the conduction band profile and the transition of electrons leading to free carrier response is shown in Fig. 6.2(b). The detection mechanism[107] involves free carrier absorption in the emitter, followed by internal photoemission of photoexcited carriers across the interfacial barrier, and then collection of carriers by the applied electric field at the contacts. The offset between the Fermi level in the emitter layer and the conduction band edge of the barrier layer forms the interfacial workfunction (Δ), which

arises due to the band offset of different materials and the band gap narrowing[68] of the highly doped emitter layer. The threshold wavelength λ_0 (in μm) is given by $1240/\Delta$, where Δ is in meV.

The IR response of the detector is characterized by the threshold (λ_0), where the response approaches zero, the peak responsivity (R_p) where the response reaches its peak, and the peak quantum efficiency (η_p). The basic approach of the responsivity calculation for a detector is outlined below following the process reported previously.[107, 74] The responsivity is given by

$$R = q\eta\lambda/hc, \tag{6.10}$$

where q is the electron charge, η is the total quantum efficiency of the detector, λ is the wavelength, h is Planck's constant and c is the speed of light. The total quantum efficiency is the product of the photon absorption efficiency (η_a) and the internal quantum efficiency (η_i), $\eta = \eta_a\eta_i$. The collection efficiency is assumed to be 1 since the maximum barrier height is at the interface.

Compared to HIWIP dual-band detectors, the HEIWIP structure has extra flexibility to adjust the response wavelength ranges. In fact, for a given material system, the wavelength threshold of the interband response in HIWIP can not be changed, while in HEIWIPs, the wavelength threshold of interband response can be changed by adjusting the alloy fraction in the barrier. In other words, the wavelength thresholds of both the interband and intraband responses of a HEIWIP can be adjusted at the device design stage. These aspects are discussed in more detail in the following sections.

6.5 Experimental UV Response

The UV spectral responsivity measurement was performed using a UV spectrometer setup consisting of a Deuterium UV source, a DK480 monochromator, and UV focusing elements. The incident UV light was modulated by a copper, and the photocurrent generated by the detector was then measured by a lock-in amplifier. The monochromator and lock-in amplifier are both controlled by LabView programs (for more details, see Appendix B). The spectra are calibrated using a photomultiplier tube with a known sensitivity (for more details, see Appendix A: Device Characterization). The UV responses of both detectors 1158 and 1547 are shown in Figs. 6.4 and 6.5, respectively. UV photons excite the valence electrons in the AlGaN barrier layer, and the generated electron-hole pairs are separated by the applied electric field before recombination, as shown in Fig. 6.2 (b). The UV wavelength threshold observed at 360 nm matches the band gap of $Al_xGa_{1-x}N$ alloys calculated using Eq. 6.3. Due to autodoping in GaN, it is expected that the barrier region will be n-doped to $\sim 10^{17}$ cm^{-3} even though no intentional doping was carried out. This autodoping may enhance the UV detection by increasing the gain in the UV detector due to trapping of minority carriers at the interface.[108]

The calculated UV responsivity along with the experimental response for the 1158 detector under -0.5 V bias at 300 K is shown in Fig. 6.4 (a). Even though the figure shows the response above 250 nm, which is due to the limitation of measurement setup, the detector is expected to show shorter wavelength response below 250 nm. As shown in Fig. 6.4 (b), when the bias applied across the detectors was increased, the responsivity increases, and a similar variation was observed for forward bias, while the responsivity under forward bias is slightly

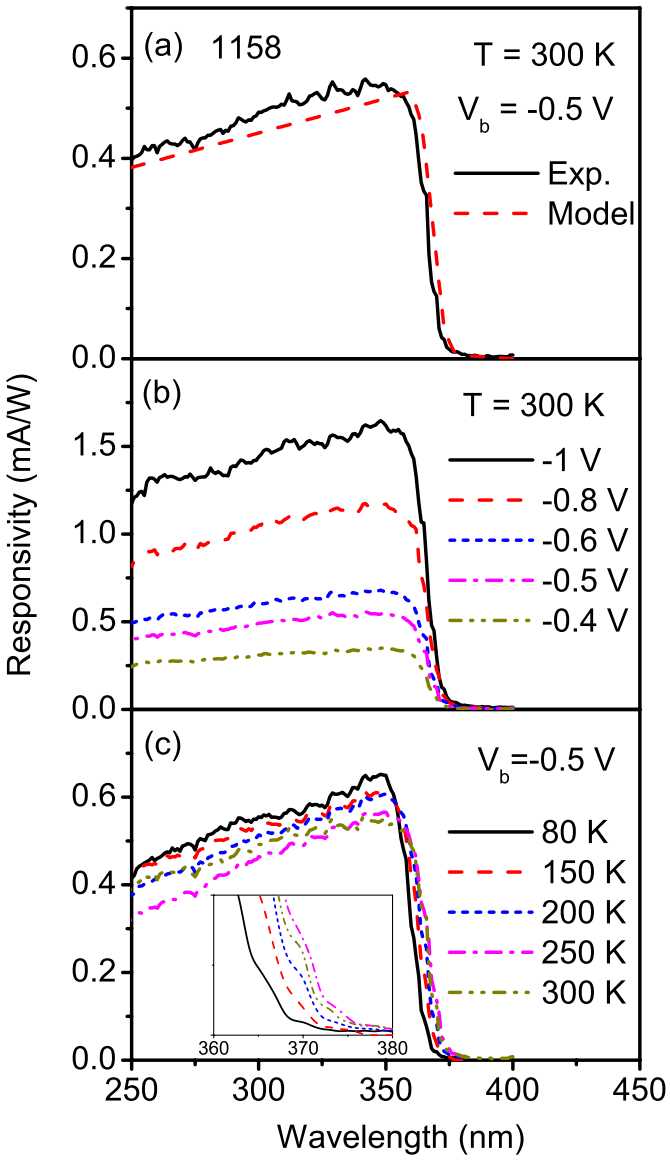

Figure 6.4: (a) Comparison of the calculated and experimental UV response of 1158 at 300 K. UV photons excite the valence electrons in the AlGaN barrier layer, and the generated electron-hole pairs are separated by the applied electric field before recombination. (b) Variation of the UV responses of 1158 detector with bias at 300 K. (c) UV responsivity of 1158 for a -0.5 V bias at different temperatures from 80-300 K. There is a small red-shift in the wavelength temperature.

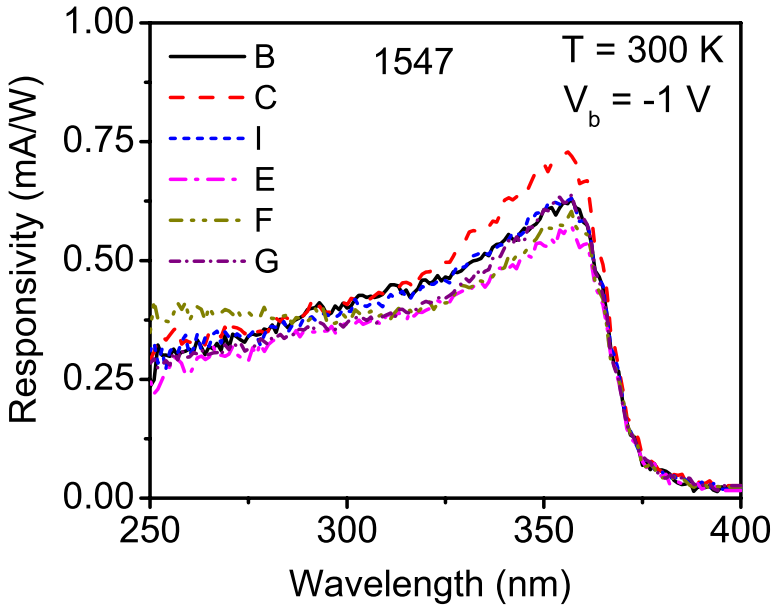

Figure 6.5: UV responsivity of several mesas of the 1547 detector at 300 K for a -1 V bias. A 20% variation in the responsivity from mesa to mesa can be observed.

weaker. When the temperature is increased, no significant variation in the responsivity was observed, as shown in Fig. 6.4 (c). This is expected, since there is no thermal mechanism associated with the UV response mechanism. The red-shift of the wavelength threshold (see inset to Fig. 6.4 (c)) that occurs when the temperature is increased is due to the band gap variation with temperature. Moreover, the UV responsivity of several mesas of the 1547 detector at 300 K is shown in Fig. 6.5. A 20% variation in the responsivity from mesa to mesa can be observed, implying a reasonable device uniformity. Most commercial UV detectors work at room temperature, and the goal of this study is to demonstrate a UV/IR dual-band detector with IR detection operating at high temperatures (above 77 K) and UV detectors operating at temperatures up to 300 K. However, presently the 1158 and 1547 detectors do not show competitive UV response, and hence the device design needs to be optimized to improve the UV and IR detection performance independently.

6.6 IR Response Due to Free Carrier Absorption

the IR spectral response measurement was carried out on both 1158 and 1547 detectors at temperatures 5.3-120 K (for more details on measurement technique, see Appendix A: Device Characterization). The variation of the IR response of 1158 in the 8-14 μm range as a function of bias at 5.3 K is shown in Fig. 6.6 (a). The calculated response at a -1 V bias is also shown in the figure. The detector has a λ_0 of 14 μm with a peak at 12 μm. The reststrahlen absorption of GaN falls in the 14-20 μm region, drastically reducing the photoresponse, as is evident from Fig. 6.6 (a). The spectral measurements performed on several mesas confirm that the detector response is consistent. The response in the 8-14 μm

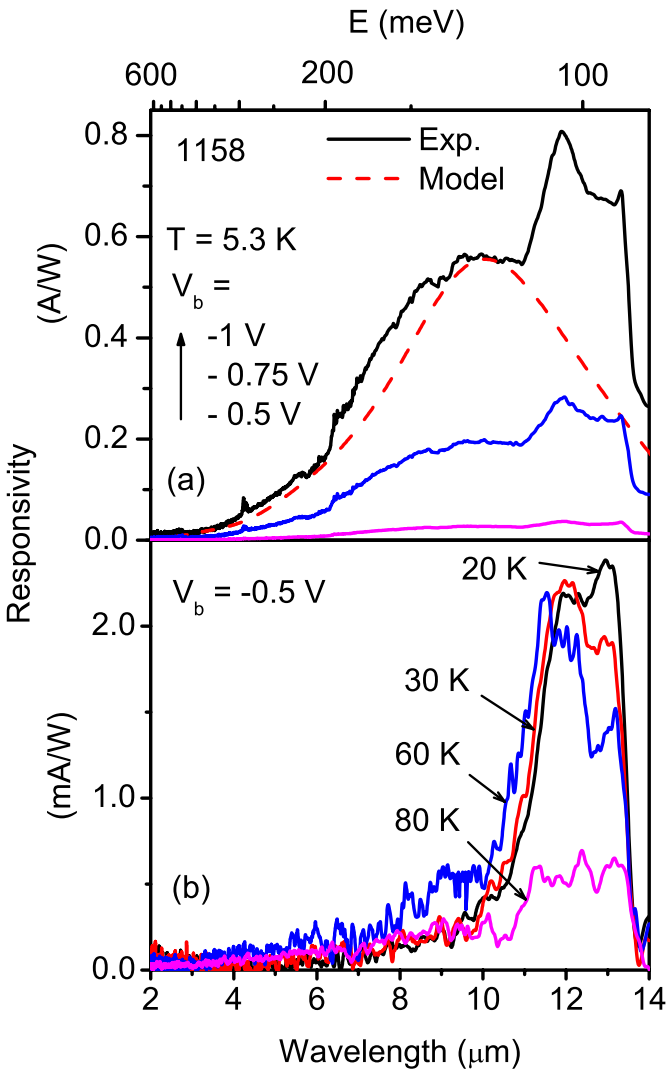

Figure 6.6: (a) Spectral response of the detector measured at 5.3 K for different biases, and the calculated free carrier response fitted with the experimental curve at -1 V. The sharp drop at 14 μm is due to the reststrahlen in GaN. (b) Spectral response measured at 20, 30, 60 and 80 K for a -0.5 V bias. The 10-14 μm response decreased in strength as the temperature increased beyond 60 K.

region is due to free carrier absorption, as expected from the theoretical calculation. The detector has a peak responsivity of 0.8 A/W and a detectivity of 2.5×10^{10} $cm\sqrt{Hz}/W$ at 5.3 K. The responsivity drastically decreases with decreasing bias, and zero response was observed at 0 V bias, confirming the lack of photovoltaic effects. A similar but slightly weaker response was observed for the detector under forward bias. The photoconductive gain at -1, -0.75, and -0.5 V biases is 1.3, 0.7, and 0.4, respectively. In addition, a peak in the 11-13.6 μm range superimposed on the free carrier response is also observed, and the origin of this peak is discussed later. The response below 14 μm can be obtained up to an operating temperature of 80 K, and Fig. 6.6 (b) shows the responsivity at 20, 30, 60 and 80 K for a -0.5 V bias. The response at 80 K is weak, only showing a signature of the response in the 10-14 μm region.

Similar to 1158, the 1547 detector shows two distinguishable IR response bands; 3-8 μm and 8-13 μm. This can be clearly observed in the responsivity curve shown in Fig. 6.7 (a). The short region response 3-8 μm is the expected free carrier response as designed (see Fig. 6.7 (b)), while the response in the region 8-13 μm could be due to impurity related transitions in the structure, which will be discussed in the following section. The oscillations in the response spectrum can be fitted with Fabry-Perot interference that originates in the structure. At 65 K, this detector has a maximum free carrier responsivity of 76 mA/W with a λ_0 of 8 μm, and an impurity response of 120 mA/W at 11.2 μm. Furthermore, the free carrier response was observed up to 120 K, as shown in Fig. 6.7 (c), and the response in the range 8-13 μm drastically decreased with increasing temperature. This temperature dependent variation is good evidence that the responses in the two regions are associated

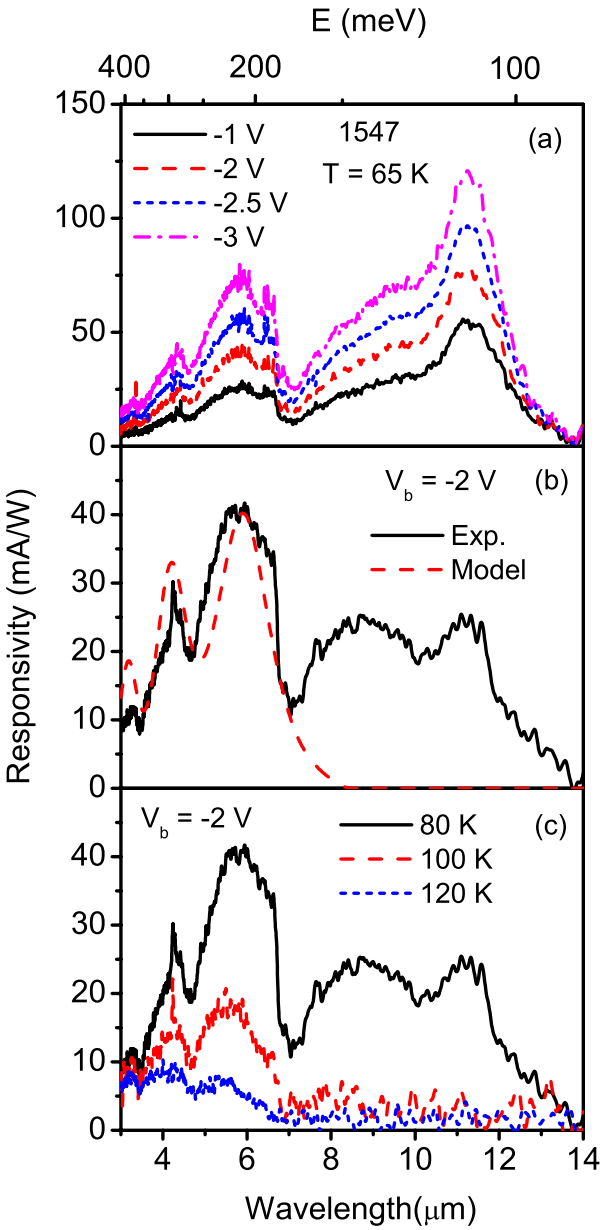

Figure 6.7: (a) Spectral response of the 1547 detector measured at 65 K for different biases. (b) Calculated free carrier response fitted to the experimental curve at 80 K and at a -2 V bias. (c) Variation of the spectral responsivity with temperature for a -2 V bias. The response in the 8-13 μm region decreased in strength as the temperature increased.

with two different mechanisms. The lower temperature for the impurity is associated with the lower energy required for thermal excitation, depleting the impurity states.

6.7 Effects of Impurities on the IR Response

The broad peak superimposed on the free carrier response of the 1158 detector in the 11-13.6 μm region (see Fig. 6.8 (a)) is assumed to be caused by either Carbon impurities or Nitrogen vacancies. The reported donor ionization energy of Carbon[109] falls in the 0.11-0.14 eV range, while the binding energy of N vacancy[110] is about 0.1 eV. As the donors in the barrier will be widely scattered, they will act as a hydrogenic atom, and the standard hydrogenic energy level model can be used to determine the location of absorption peaks associated with a given transition. Carbon can be unintentionally introduced into GaN during the growth, either as a donor at a Ga site, or as an acceptor at a N site, mainly through the organic precursors. Assuming that the two peaks observed at 11.9 μm (104.2 meV) and 13.3 μm (93.2 meV) are due to transitions of the first impurity excited-state, the ionization energies were calculated to be 139 and 124 meV, respectively. These ionization energy values in the 140-110 meV range support the assumption that the corresponding transitions are Carbon donor related impurity transitions. Transitions related to Carbon acceptors (0.89 eV of ionization energy)[109] fall out of the spectral range reported here (below 1.4 μm), although the Carbon acceptors are preferred in GaN.[111] The measurements performed on different devices provide consistent results.

Similarly, as shown in Fig. 6.8 (b), the 1547 detector shows an impurity response in the 7-13 μm range with two peaks at 9 and 11 μm (138 and 113 meV, respectively). Thus,

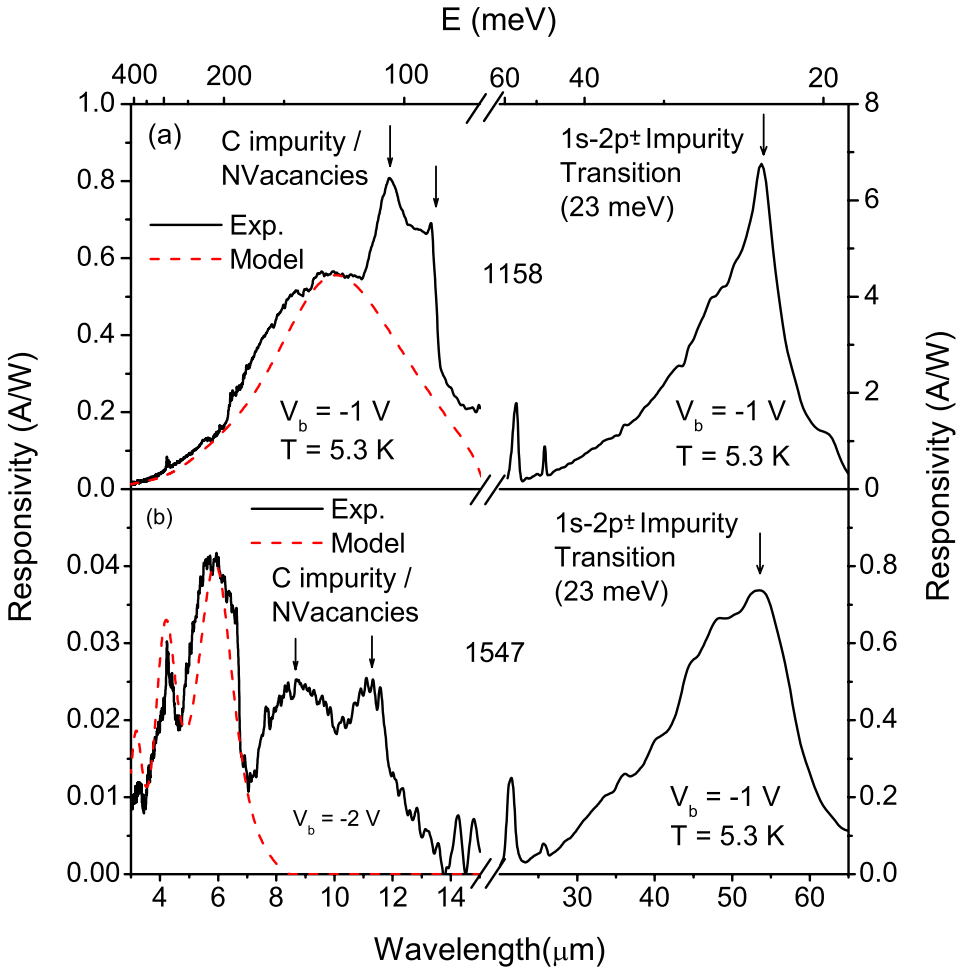

Figure 6.8: Impurity-related responses of the (a) 1158 and (b) 1547 detectors. The broad peak in the 11-13.6 μm and 8-13 μm regions (for 1158 and 1547, respectively) superimposed on the free carrier response is probably due to Carbon impurities and/or Nitrogen vacancies in the structure. The response at 54 μm (5.5 THz) observed for both detectors at 5.3 K is based on 1s-2p$\pm$ transition of Si donors in GaN.

these features could also be due to transitions between carbon impurity states. Furthermore, the temperature variation of the response implies further that the two response regions are associated with two different mechanisms. Depleting the impurity states makes the impurity response visible only at low temperatures. For detectors with a threshold above 14 μm, these impurity transitions enhance the response. Detectors designed to have shorter thresholds (below 14 μm) operating at high temperatures will not show the expected performance at the designed temperature, because the thermal excitations take place through impurity states. However, to reduce the incorporation of carbon, which affects the IR detector response, alternative group III precursors can be explored.

As shown in Fig. 6.8 (a) and (b), a sharp peak at 54 μm (5.5 THz) is observed for both 1158 and 1547 detectors at 5.3 K. The energy corresponding to this peak is 23 meV. The donor binding energy of Si in GaN has been found[112] to be 29 meV, and the transition from 1s to 2p$\pm$ level occurs at 21.9 meV. Moore et al.[113] have reported the 1s-2p$\pm$ transition of Si in GaN at 23.3 meV and the donor effective mass binding energy of 31.1 meV. Hence, the sharp response peak observed at 23 meV can be identified as 1s-2p$\pm$ transition of Si donors in GaN. IR absorption measurement is a well known technique to identify the shallow impurities such as Si in GaN. This study not only confirms the 1s-2p$\pm$ transition of Si in GaN but also shows that a GaN/AlGaN detector can be a 5.5 THz detector. Since the donor states of Si in intentionally doped GaN are clearly understood and stable, a 5.5 THz detector could be developed based on the 1s-2p$\pm$ transition, and the result is promising even for an unoptimized detector. This result is consistent with the impurity associated response observed for GaAs- and Si-based HIWIPs in Chapter 5.

6.8 Terahertz Radiation Detection Based on n-GaN/AlGaN HEIWIPs

In addition to the free carrier and impurity-related responses discussed above, there is also a slower mechanism which responds out to 300 μm (1 THz), as shown in Fig. 6.9. This response could possibly be due to either a thermal or pyroelectric effect. The two curves shown in the figure were taken with two scan speed settings (optical path difference velocity-OPD) in the FTIR spectrometer. Under a high OPD velocity (1 cm/s), only the Si impurity-related response at 54 μm in the 20-300 μm range is visible in the FIR region. When the OPD velocity is reduced to its minimum value (0.05 cm/s), the broad flat response extending to 300 μm is observed. In order to test for possible thermal mechanisms, three samples with different sizes (1158 structure) but with a mesa having the same optical area were fabricated. If the detection is due to a thermal mechanism, one would expect that the photocurrent is proportional to the change in temperature of the sample. Therefore, if the same amount of radiation is incident on all the samples, the responsivity should be inversely scaled with the sample thermal mass. However, the observed responsivity variation for three samples scaled with the total mass of the sample (not inversely scaled). As a reason, it was found that the amount of IR radiation collected by each sample is not the same. Since the three samples collected different amount of IR radiation, it was not possible to determine whether the terahertz response is originated from a thermal mechanism. Other potential detection mechanisms such as pyroelectric effects have not yet been studied. However, a study of the origin leading to this response will not only justify the terahertz detection, but also lead to understanding its effects when optimizing the detectors for shorter wavelengths.

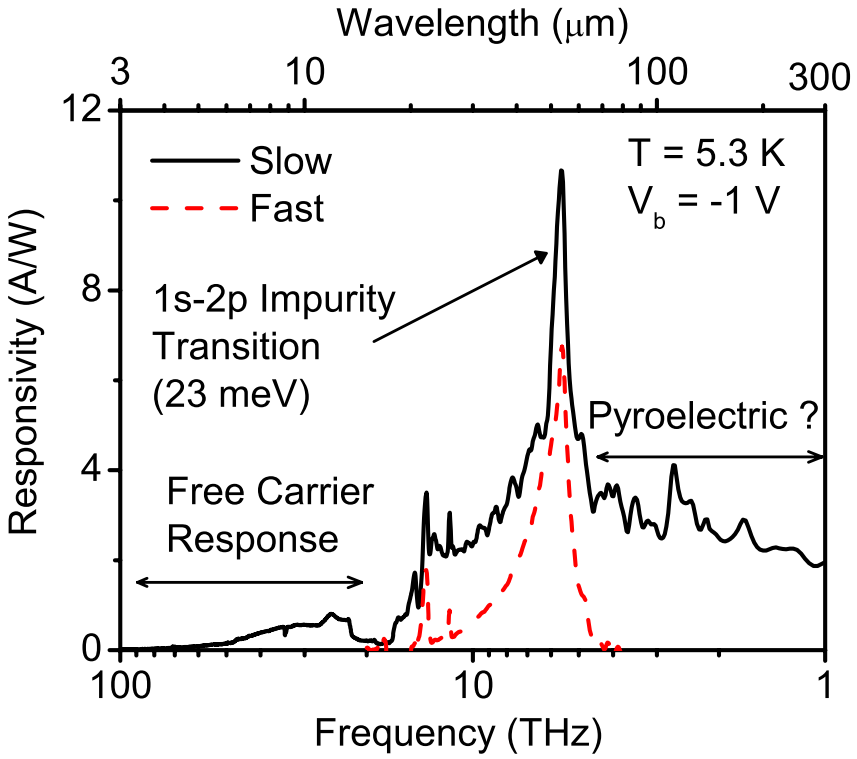

Figure 6.9: The full IR range response of the 1158 detector at 5.3 K for a -1 V bias. There are three response mechanisms, which can contribute to the photocurrent: free carrier response, impurity-related response, and a flat terahertz response. The flat response is slow and could be possibly due to a pyroelectric or other mechanism. At high speed scanning mode, other than the free carrier response only the impurity-related response (dash-line) is visible in the FIR region.

6.9 Dark Current, Noise, and Capacitance Measurements

The dark I-V characteristics of the detectors were obtained as explained in Appendix A: Device Characterization. The I-V characteristics of the 1158 detector at different temperatures, along with the 300 K background photocurrent curve measured at 30 K, are shown in Fig. 6.10 (a). Based on the dark and the photocurrent measurements, the BLIP temperature is 30 K. A higher BLIP temperature is expected for this detector, however, it is possible that the BLIP temperature is reduced by the effects of the FIR response (THz response) mechanisms, which are observed at low temperatures.

The dark I-V characteristics of the 1547 detector at temperatures of 80-300 K are shown in Fig. 6.10 (b). A comparison between the dark current densities of both detectors (1158 and 1547) is shown in Fig. 6.10 (c). The dark current densities for 1547 are lower than that for 1158, and this variation, as expected, is due to the lower free carrier threshold of 1547 than that of 1158. However, both detectors have higher dark current density than other detectors operating in the similar regions. This increase is possibly ascribed to the hopping conductivity of Si impurity electrons in the barrier. The presence of Si impurities has been confirmed by the response peaks corresponding to photoionization of impurity atoms, which was discussed in the previous section.

Preliminary noise measurements were carried out on both 1158 and 1547 detectors (for details of the measurement technique, see Appendix A: Device Characterization). The measurements were conducted at the same temperatures and bias voltages as were used during spectral response measurements. These measurements were done with the detector under dark conditions. The dependence of the noise current (I_n) of 1158 on applied bias

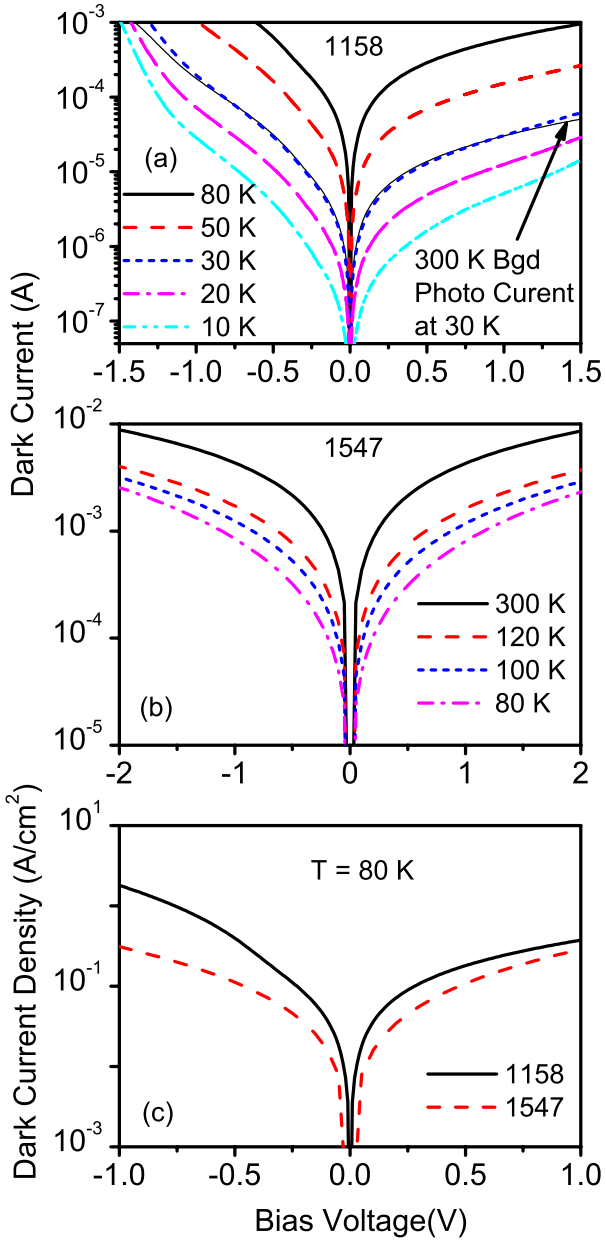

Figure 6.10: (a) The I-V curves of the 1158 detector at different temperatures under dark conditions, and the 300 K background photocurrent at a temperature of 30 K. The detector has a BLIP of 30 K, which is lower than the expected BLIP temperature. (b) Dark current of the 1547 detector at temperatures in the range 80-300 K. (c) Comparison of the dark current density of 1158 and 1547 detectors. The lower dark current for 1547 is expected, because the free carrier threshold of 1547 is shorter than that of 1158.

at 5.3 K, and on temperature for a -0.5 V bias is shown in Fig. 6.11 (a) and (b). A similar variation of the noise current was observed for 1547 detector as shown in Fig. 6.11 (b). As the bias and the temperature increased, the noise current also increased, similar to other IR detectors.[58, 59, 57] Both detectors under any operating temperature showed a 1/f noise component. The exact exponent for the noise spectrum was determined by fitting the noise current density, S_n ($= I_n^2$), as shown in Fig. 6.11 (d). The value of the slope of the linear fit is ∼-0.95 (= -1 for 1/f), and very close values were obtained for all other noise spectra. Based on the dark current and noise spectra, the photo conductive gain can be calculated (for more details, see Appendix A: Device Characterization). The calculated photoconductive gain for the 1158 detector at -1, -0.75, and -0.5 V bias values are 1.3, 0.7, and 0.4, respectively. Furthermore, the detectivity of the detector (reported before) was calculated using the noise current under given conditions.

Capacitance-voltage (C-V) and capacitance-frequency (C-f) measurements were carried out on both detectors (for details of the measurement technique, see Appendix A: Device Characterization). Under the operating conditions, the capacitance values of devices are required at the camera development stage, since the detector array is coupled with readout electronics. However, the primary aim of capacitance measurements in this work is to understand the impurities in the barrier layers. First, consider the results obtained for the 1547 detector shown in Fig. 6.12 (b) and (c). A similar frequency dependence was observed for a forward bias. The variation in the capacitance indicates the presence of space charge (most probably from ionized impurities) in the barrier layer. When the frequency dependence of the capacitance is considered, it is observed that at high frequencies and

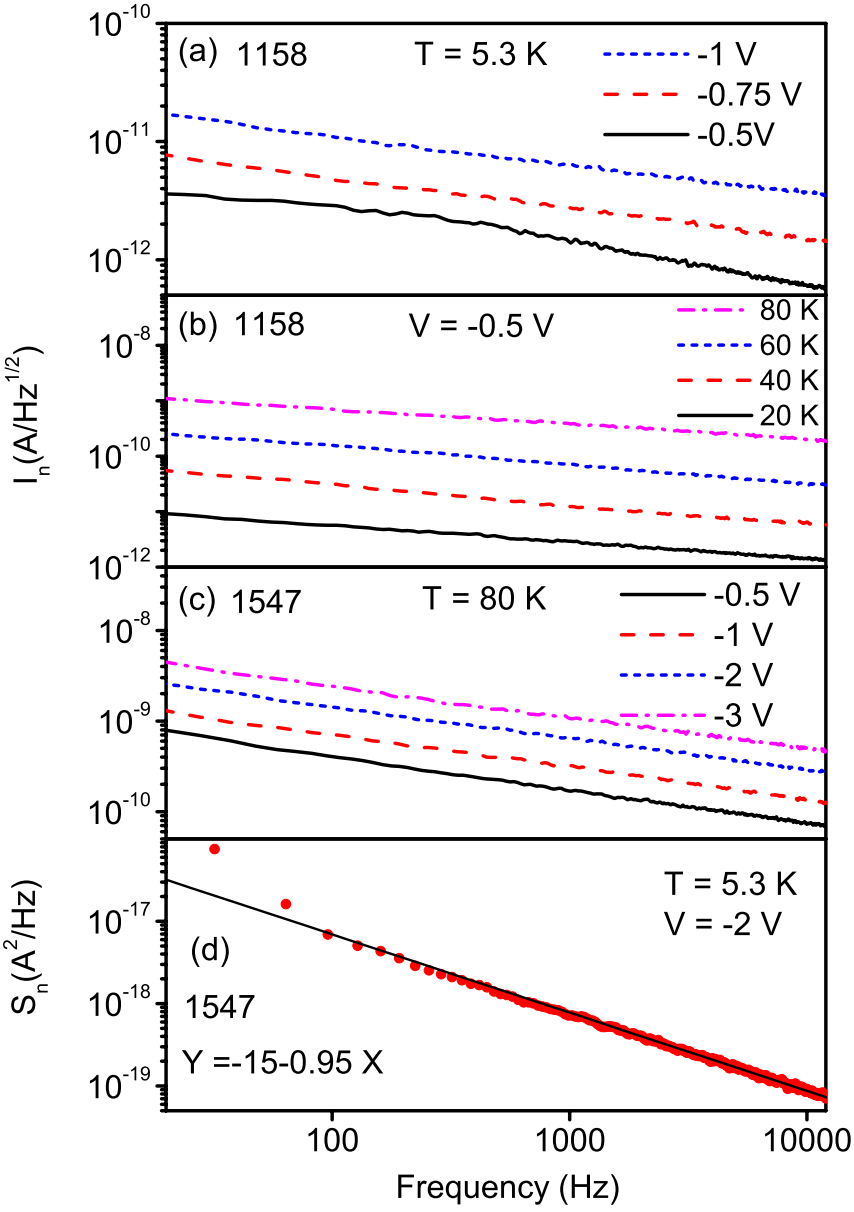

Figure 6.11: Noise current spectra measured for the 1158 for dark conditions at (a) 5.3 K under different bias values, and (b) different temperatures for -0.5 V bias. (c) Noise current spectra measured for 1547 at 80 K. (d) The 1/f behavior of noise current density of 1547 detector. The linear fit with a slope of -0.95 confirms the 1/f dependency of noise current density.

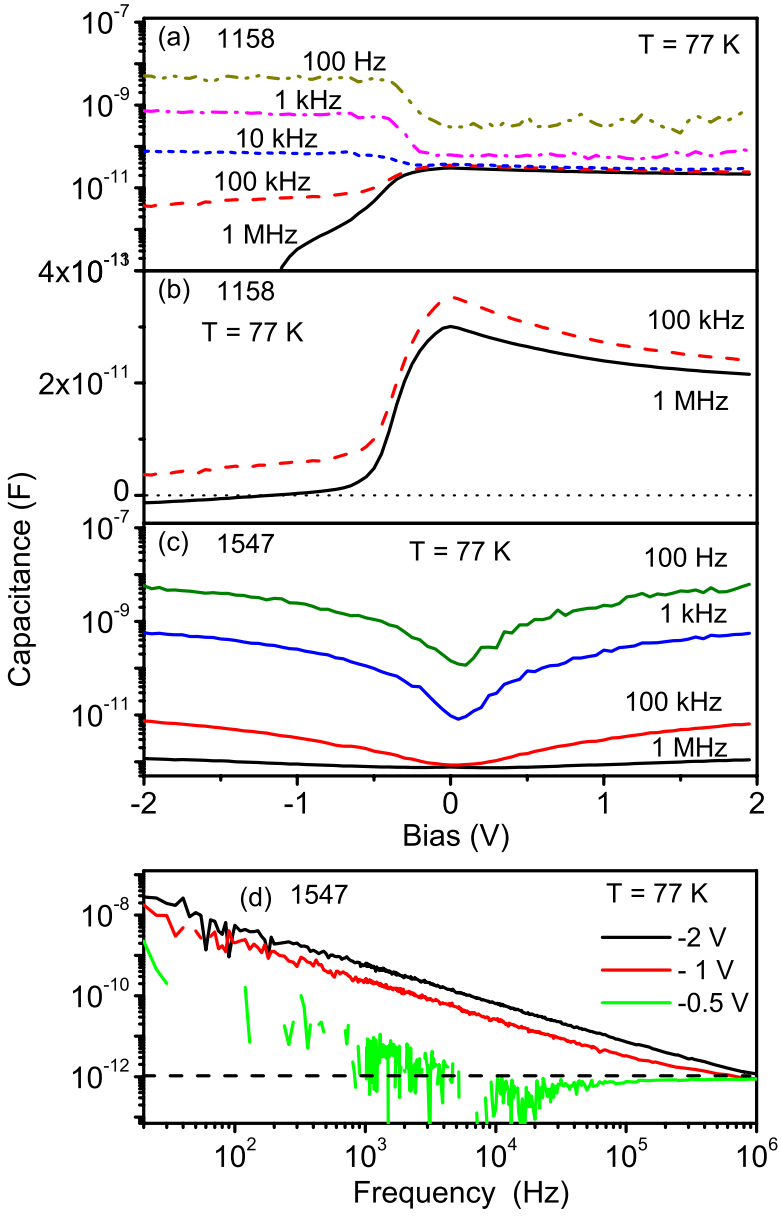

Figure 6.12: (a) C-f curves for the 1158 detector. (b) Linear plot of C-f for 1158 detector showing negative capacitance at 1 MHz under bias values below -1.1 V. The dashed-line indicates the geometrical capacitance. (c) Measured C-V and (d) C-f for the 1547 detector at 77 K. At high frequency and low bias, the capacitance equals the geometrical value for a parallel plate capacitor.

low bias the measured value corresponds to the geometrical capacitance of a parallel plate capacitor with an area equal to the mesa area and a separation equal to the barrier thickness. This is due to the voltage changes being too fast for the impurities to react at the low bias. As the frequency decreases, the impurities have time to become charged and the capacitance increases rapidly with decreasing frequency. As the bias is increased, carriers due to the dark current ionize the impurities, making them respond faster. This increases the value at which the capacitance begins to be above the geometrical value. This trend can also be seen in the C-V measurements which show a steadily increasing capacitance with the bias.

The results observed for the 1158 detector as seen in Fig. 6.12 (a) and (b) were very different from those for the 1547 detector. For positive bias, it showed a nearly constant capacitance. However, for negative bias, there was a step observed in the capacitance in the range of -0.2 to -0.5 V. For high frequencies, this step decreased the capacitance, and for 1 MHz the capacitance becomes negative[114] under bias values below -1.1 V. Although the reason for the step pattern observed in the 1158 detector is not known and needs further investigation, the presence of interface states[115] may be one possible explanation.

6.10 UV/IR Dual-Band Response

The UV/IR dual-band response of detectors is shown in Fig. 6.13. While UV detection is possible at any temperature up to 300 K, the free carrier response can be obtained up to 80 and 120 K for the 1158 and 1547 detectors, respectively. Also, both detectors have the 54 μm impurity-related response at 5.3 K. The experimental and calculated wavelength thresholds of both detectors in UV and IR regions are shown in Fig. 6.14.

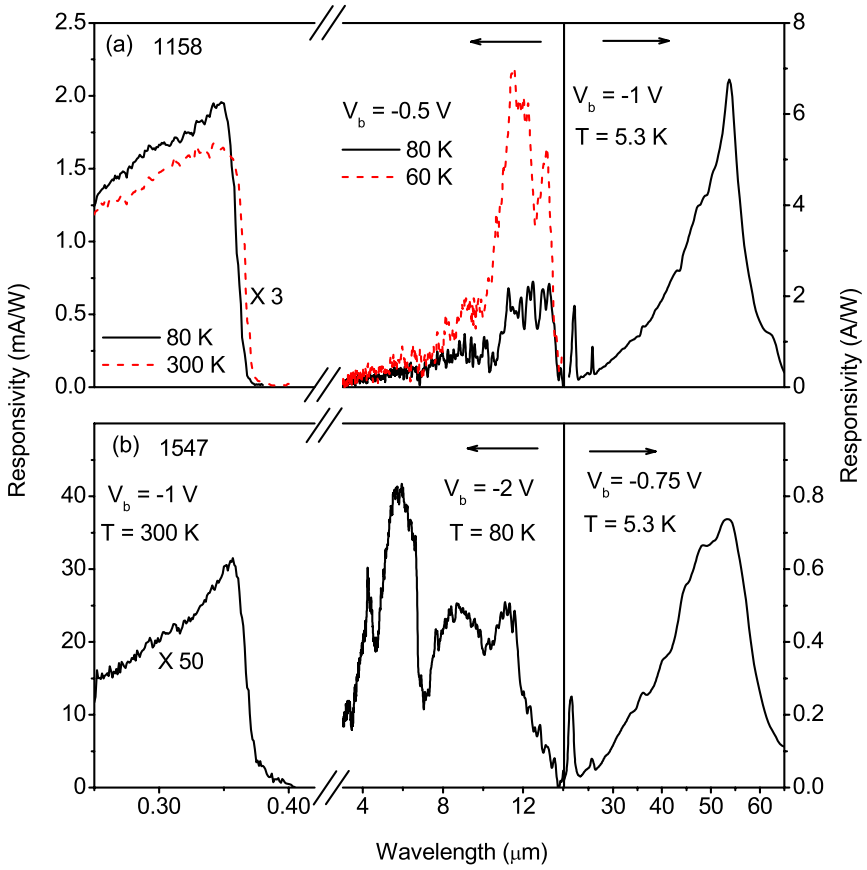

Figure 6.13: (a) UV/IR dual-band response of the (a) 1158 and (b) 1547 detectors. The IR response is visible up to 80 K for the 1158 detector and up to 120 K for the 1547 detector, while the UV response can be obtained at any temperature up to 300 K. The response at 54 μm (5.5 THz) which is due to the transition between 1s and 2p$\pm$ impurity levels of Si in GaN is also shown.

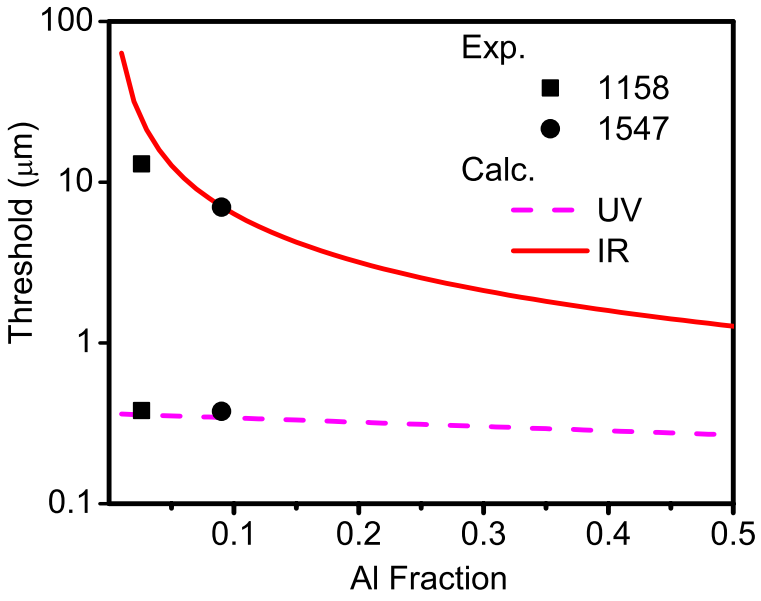

Figure 6.14: Experimental and calculated wavelength thresholds in UV and IR regions for the two $GaN/Al_xGa_{1-x}N$ HEIWIP detector structures with $x = 0.026$ and 0.1.

The dual-band detection approach reported here can be used to develop dual-band detectors tailored to specific applications. This is more easily achievable with HEIWIP than HIWIP detectors. By adjusting the material composition in the layers, the thresholds for the interband and intraband responses can be tailored separately. For an $Al_xGa_{1-x}N/Al_yGa_{1-y}N$ based detector, if the Al fraction is varied in both the emitter and barrier by the same amount, only the interband threshold will change, while the intraband threshold remains constant. Alternatively varying only the emitter Al fraction, the intraband threshold could be varied without changing the interband threshold. Moreover, the resonant cavity effects can be used to tailor the IR response peak to the desired wavelength. By adjusting the materials, it will be possible to tune the interband threshold from the UV to the NIR, and the intraband threshold from the MIR to the FIR. This dual-band approach with HEIWIP detectors can be tested with other materials such as InN, InGaN, AlGaN, and AlN. InN could give an interband response in the NIR region, while InGaN could respond in the VIS-NIR regions. A UV interband response could be expected from an AlN based detector. Also, as the response for the two processes originate at different locations, it will be possible to design a device that is capable of separately measuring both components simultaneously. The idea is to use three contacts to measure the two current components simultaneously, and separate the UV and IR contributions from these current components. This idea is explained in detail later.

6.11 UV Detection Enhancement

In comparison with commercial UV detectors, the reported GaN/AlGaN HEIWIP UV/IR dual-band detectors have much lower UV responses. The probable cause for the low UV response is the high absorption of UV radiation within the 0.2 μm thick top-contact layer. The absorption coefficient for GaN is $> 10^5$ cm^{-1} and the skin-depth (δ) is < 0.1 μm, as shown in Fig. 6.3, which means that in the 0.2 μm thick top-contact, the absorption would be 90% or greater. Also the carriers generated by the absorption of UV radiation in the top-contact do not contribute to the photocurrent. In order to understand the effects of the top-contact, a series of samples with different top-contacts (0.2, 0.1, 0.05, 0.02, and 0 μm) from the 1547 structure were fabricated by etching the top-contact out, except directly under the metal ring. A schematic diagram of these samples is shown in Fig. 6.15 (b). These samples were then tested for I-V measurements and UV/IR response measurements. Below, the labels "Unetched" and "Etched" will refer to the original detector and the detector after etching the top-contact, respectively. In the completely etched-structure, UV radiation is directly incident onto the barrier layer, and a maximum absorption of UV radiation can be expected. However, there will be a reduced IR detection under reverse bias (top-contact is negative) since there is no emitter region for free carrier absorption.

As shown in Fig. 6.16 (a), the dark current of the etched-detector was decreased by more than an order of magnitude when the top-contact was completely etched. Since the top-contact has been removed inside the metal ring, the effective electrical area of the device was reduced, leading to a higher resistance, and hence lower dark current. A comparison of the UV and IR responses between all the samples is shown in Figs. 6.16 (b) and 6.17. The

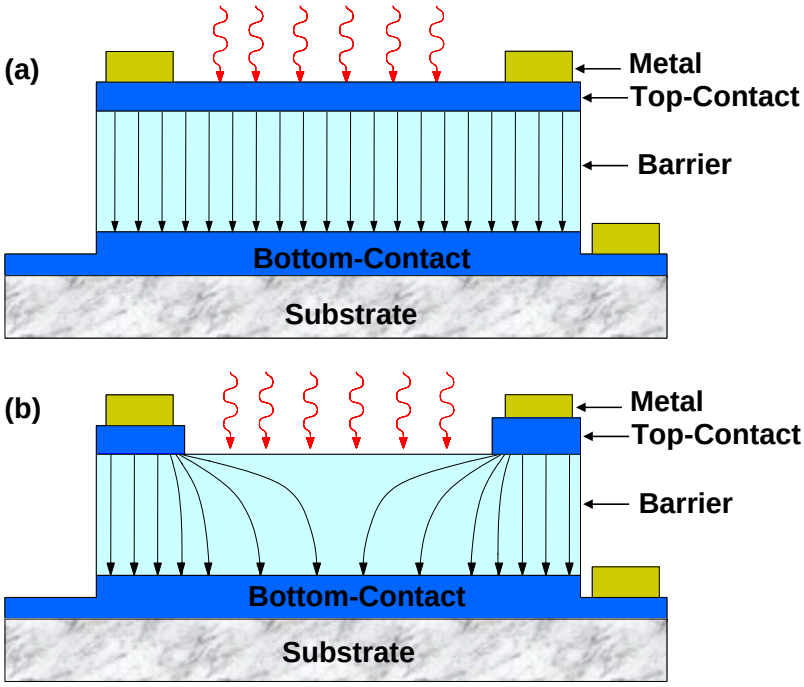

Figure 6.15: Device structure showing (a) the original device and (b) the processed device with the top-contact layer etched away inside the ring contact. Because the AlGaN layer was 400 μm wide and only 0.6 μm thick, when the window was etched into the GaN layer, the electric field in the AlGaN layer did not spread laterally a significant distance. Although no field lines are drawn in the center due to the very low field value, there will be still a small field at the center (0.7% of the field at the edges).

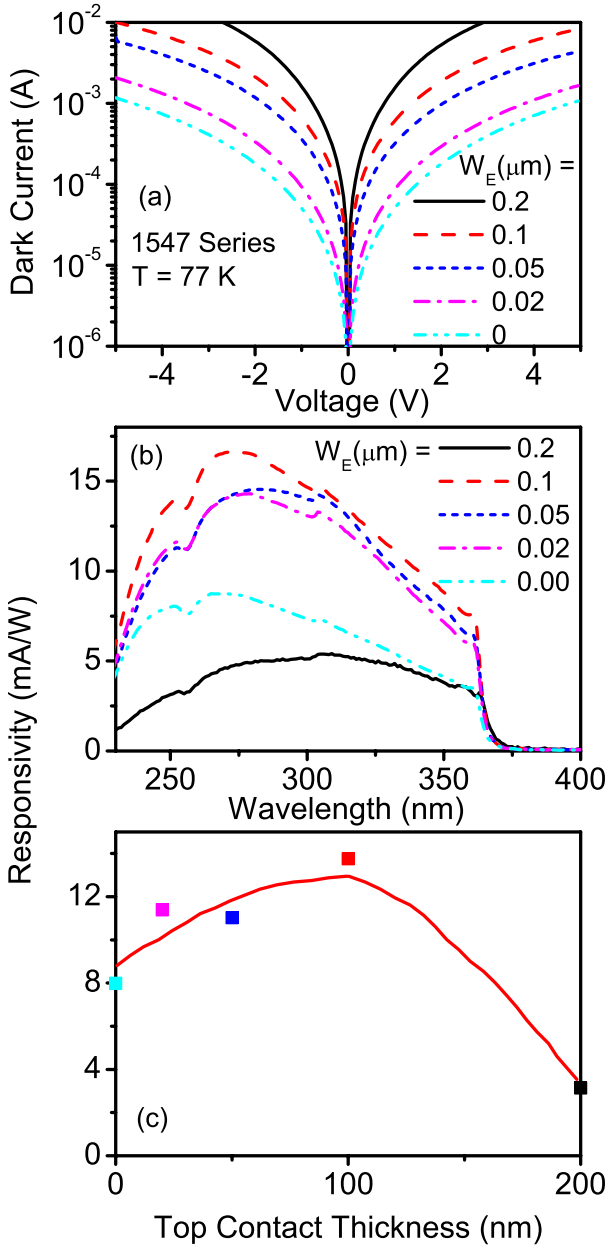

Figure 6.16: (a) A comparison of the dark current of the detectors with different top-contact etching depths. (b) UV responsivity spectra for etched-samples with different etch depths. (c) Variation of the UV response at 250 nm with the top-contact thicknesses. The optimum top-contact thickness is found to be ~ 0.1 μm.

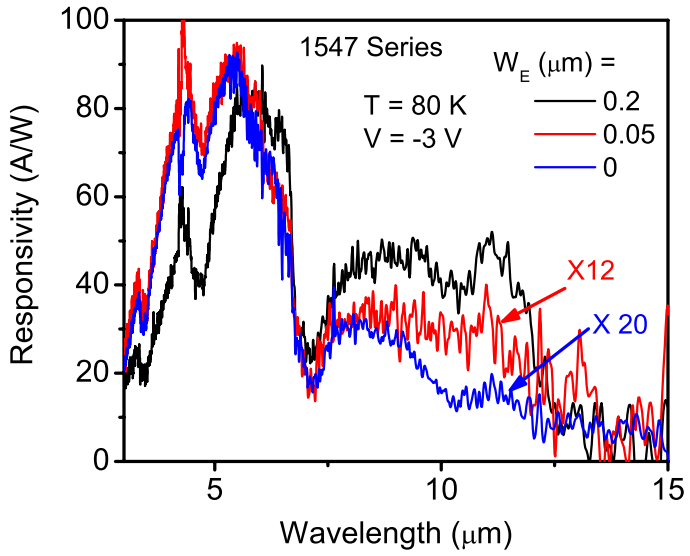

Figure 6.17: A comparison of IR response of unetched- and etched-detectors. The IR response of the completely etched-detector for a reverse bias has been reduced by a factor of 20, since the thickness of the emitter is reduced by etching, which reduces IR absorption in the emitter. However, there is still non-zero IR response due to impurity transitions in the barrier and a portion of the top-contact left under the ring contact in the structure.

UV response was measured at a temperature if 300 K for a -1 V bias, while the IR response was determined at 80 K for a -3 V bias, and all the samples were measured in a single run to minimize any change in the measurement setup. By etching the top-contact, the UV response was enhanced by a factor of 3, while the IR response was reduced by a factor of 20. For the completely etched-detector, even though the absorption in the barrier layer is high, the expected enhancement was not achieved. This could be due to the reduced collection efficiency of the excited carriers as a result of the non-uniform electric field distribution in the barrier and hence the weak field in the middle of the barrier, as shown in Fig. 6.15 (b). Considering the UV responsivity variation as shown in Fig. 6.16 (c), the optimum thickness seems to be approximately 100 nm, which is much larger than the thickness needed for a uniform electric field distribution. The IR response of the etched-detectors under reverse bias has reduced significantly, since the thickness of the emitter is reduced by etching, which reduces IR absorption in the emitter. However, there is still a non-zero IR response due to impurity transitions in the barrier and the portion of the top-contact left under the ring contact in the structure. These results were considered in order to design a UV/IR dual-band detector for simultaneous measurements, which is discussed in the next section.

6.12 Simultaneous Measurements of UV and IR Responses

Before proceeding to simultaneous measurements of UV and IR photo current components, it would be useful to test the effects of UV on IR response and effects of IR on UV response. Hence, the 1547 detector was used to measure the two photocurrent components when both UV and IR radiation is incident onto the detector. In order to per-

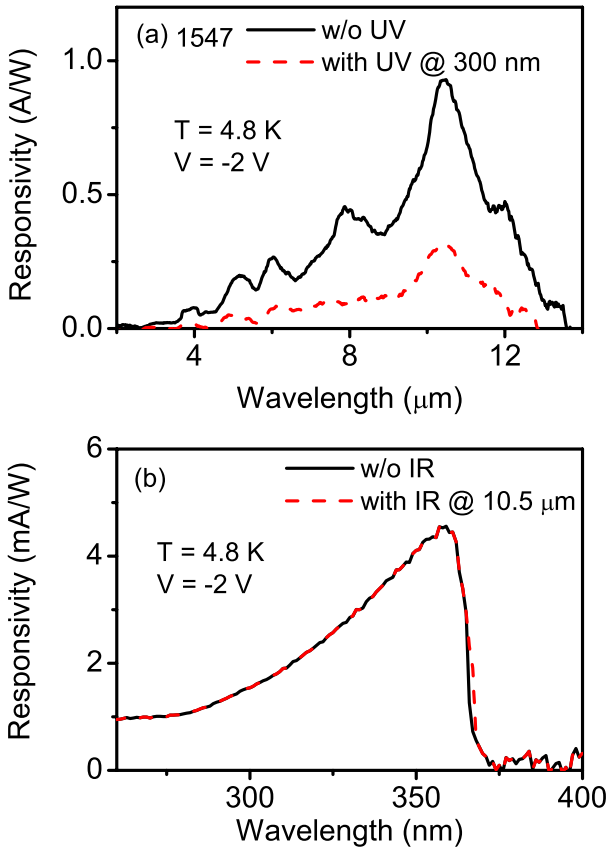

Figure 6.18: (a) A comparison of the IR response of the device without (w/o) UV irradiation (solid), and with UV irradiation (4 μW, dashed). The IR response shows a significant drop. (b) The UV response of the device without (w/o) and with 10.5 μm IR radiation (7.5 nW) incident onto the detector.

form simultaneous response measurements for UV and IR radiation, a UV-IR dual response spectrometer setup was built by using two monochromators, two sources (UV and IR), and UV and IR focusing elements (for more details, see Appendix A: Device Characterization). Both UV and IR incident light beams were modulated (at two separate frequencies) and were measured simultaneously with two lock-in amplifiers. This approach allows measurements using any desired combination of UV and IR illumination. A series of UV and IR measurements was performed on the 1547 detector. First, the IR response was measured without UV incident onto the detector as shown in Fig. 6.18 (a) (solid line). Then the UV response without IR incident on the device was measured as shown in Fig. 6.18 (a) (solid line). The dual response of the detector was measured in two different scanning modes; 1) The full range IR response when 4 μW of 300 nm UV radiation is incident on the detector, 2) The full range UV response when 7.5 nW of 10.5 μm IR radiation is incident on the detector. As shown in Fig. 6.18 (a), the IR response decreased with the presence of 300 nm UV radiation, while on the other hand, the UV response did not change when 10.5 μm radiation was incident on the detector as shown in Fig. 6.18 (b).

The 10.5 μm IR response with the simultaneously measured UV response of the detector and the UV intensity when the UV region is scanned are shown in Fig. 6.19. In the 200-240 nm wavelength region, there is no UV response shown due to an optical window used in the setup, blocking almost all of the incident UV radiation as can be seen from the UV intensity curve, and the IR response is at a constant level. However, when the window starts to transmit UV radiation, the 10.5 μm FIR response starts to decrease. When the UV response reaches zero above 360 nm, the IR response starts to increase, however, the

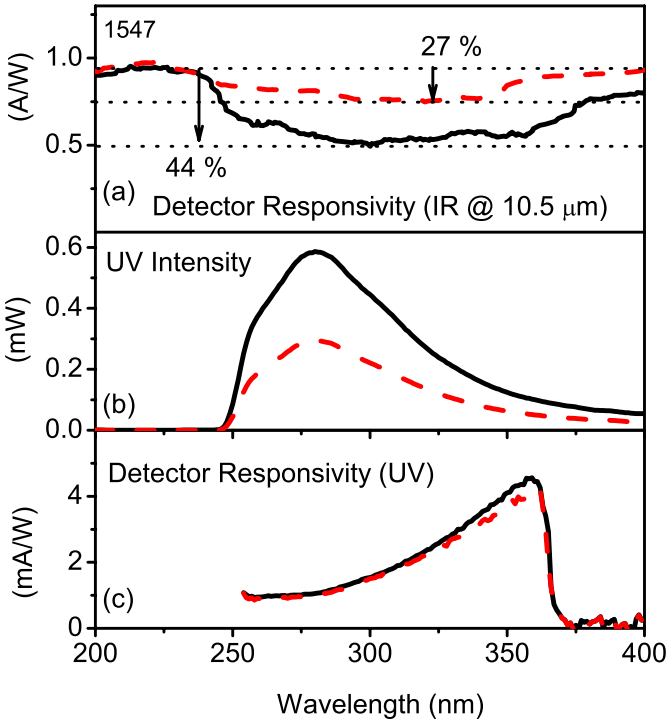

Figure 6.19: (a) The IR response of the detector at 10.5 μm measured simultaneously with the UV response (c) when the UV response was scanned in the range 200-400 nm. (b) The UV intensity incident on the detector. The IR power incident on the detector was 7.5 nW, while the peak UV power was 4 μW for the solid curve and 1.5 μW for the dashed curve. Both UV and IR spectra were measured simultaneously.

signal does not reach the initial level as the window is still transmitting UV radiation even though the device does not respond to this wavelength UV radiation. The observed drop of the IR response due to UV photogeneration for a 4 μW peak UV power is about 44%. When the peak UV power is reduced to 1.5 μW, the drop is reduced to 27%. Based on these experimental results on simultaneous measurements, there are three effects that appear to be occurring: 1. the UV illumination produces a persistent reduction in the IR response from the impurities, but not from the free carriers; 2. the UV illumination produces a reduction in the IR at all wavelengths which lasts only while the illumination is occurring; and 3. the IR radiation does not cause a decrease in the UV response.

While the dual-band detectors detect both UV/NIR and IR radiation, the two components of the photocurrent generated by UV/NIR and IR radiation cannot be separated out without using external optical filters. External optical components reduce the incident radiation intensity, and hence decrease the performance of the device. As the response for the two processes originate at different locations, it will be possible to design a device that is capable of separately measuring both components of the photocurrent simultaneously. The idea is to use three contacts to measure the two separate currents simultaneously, and then from these currents to separate the UV and IR contributions. The processed device structure and the conduction/valence band profile for the proposed design are shown in Figs. 6.20 and 6.21, respectively. The expected wavelength thresholds in the UV and IR regions are 350 nm and 14 μm, respectively. The photocurrent generated by IR radiation can be measured with the middle- and bottom-contacts (IR active region) under both forward and reverse bias. The UV skin-depth (see Fig. 6.3 (c)) is smaller than the combined

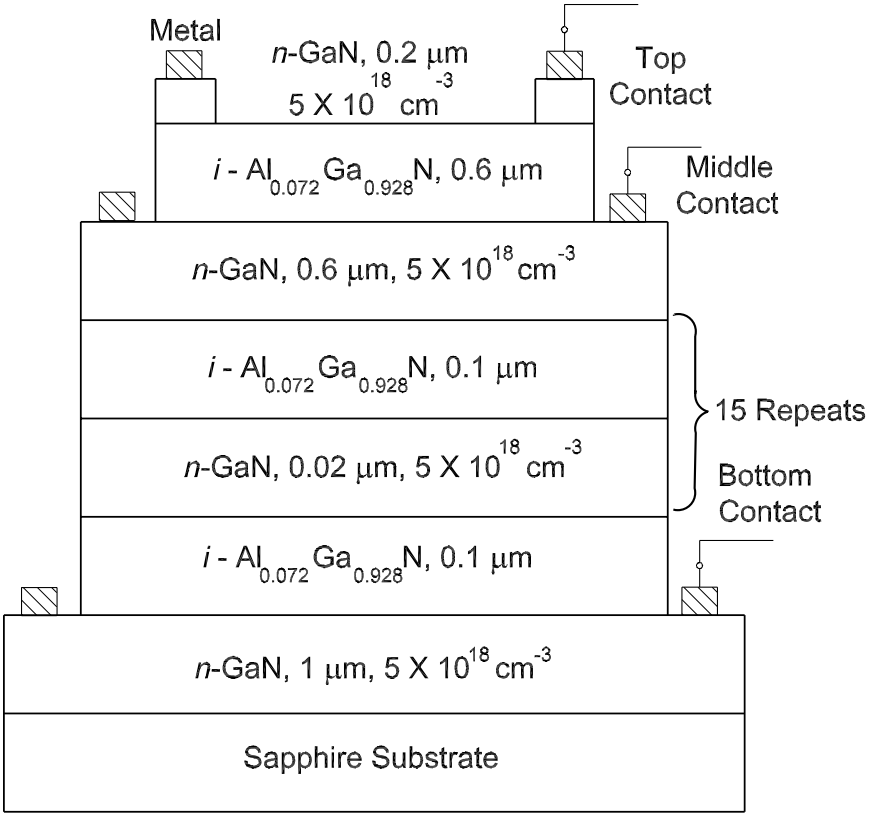

Figure 6.20: Schematic diagram of a processed GaN/AlGaN HEIWIP detector structure designed for simultaneous measurement of the two components of the photocurrent generated by UV and IR radiation.

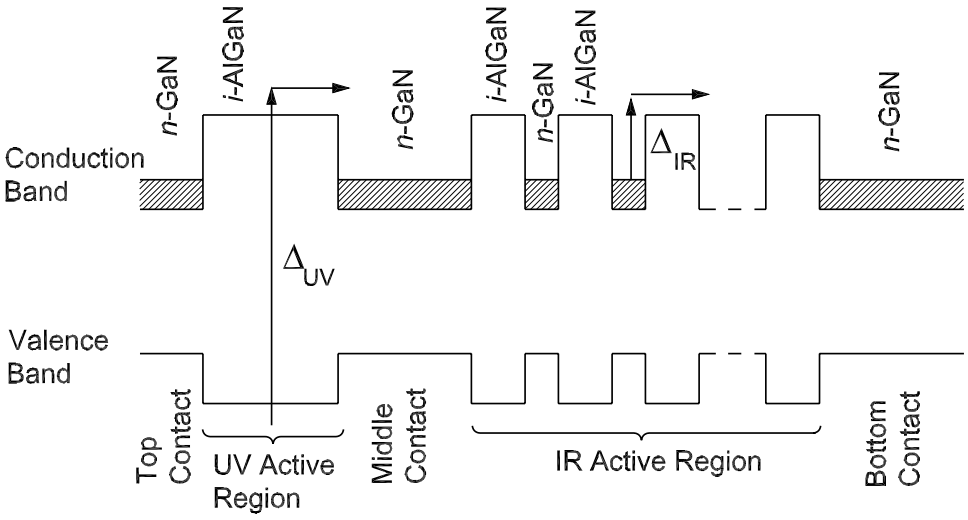

Figure 6.21: Conduction and valence band profile of the proposed device structure designed for simultaneous measurement of the two components of the photocurrent generated by UV and IR radiation.

thickness of the UV active region, and hence the intensity of UV radiation incident onto the IR active region is insignificant. As a result, UV absorption does not take place in the IR active region. The component of the photocurrent generated by UV radiation can be measured with top- and middle-contacts. Since the top-contact is etched out leaving only a ring-contact, there is no effective emitter-barrier junction when the top-contact is negatively biased. Therefore, under this configuration, there is no free carrier generated IR photocurrent expected in the UV active region. The structure was grown, processed, and tested for UV/IR simultaneous measurements. Preliminary results demonstrate the potential UV and IR simultaneous detection capability of three-contact detectors.

6.13 Conclusion

GaN/AlGaN UV/IR dual-band HEIWIP detectors responding in the UV (200-360 nm) and IR (8-14, 3-13, and 20-70 μm) regions. The UV response is based on interband transitions in the barrier, while the IR response is due to intraband transitions in the emitter followed by photoemission across emitter/barrier interface. The responses of two detectors in the 8-14 and 3-8 μm ranges are due to free carrier absorption in the structure, while the response at 54 μm (5.5 THz) is based on 1s-2p$\pm$ transition of Si donor atoms in GaN. Some minor response contributions associated with impurity states in the system were also observed. By adjusting the material or the alloy fraction, the threshold of the interband and intraband responses can be tailored. Based on theoretical models and experimental results, the transitions leading to each band are explained. This work also demonstrates how detectors responding in several wavelength regions can be made by using different

Sample	Structure Type	$\lambda_P(\mu m)$ $[\Delta\lambda/\lambda(\%)]$	R_P (mA/W) @ T (K)	$\eta \times g$ (%)	D* (Jones)	T_{max} (K)
1388	DWELL	6.25 [28]	120 @ 80	2.8	1.4×10^9	80
		10.5 [22]	125 @ 80	1.8	1.5×10^9	80
		23.3 [39]	40 @ 80	0.4	4.6×10^8	80
MG386	T-QDIP	6.2 [10]	620 @ 80	12	1.2×10^{10}	300
		17 [37]	150 @ 300	1.1	1×10^7	300
MG764	T-QDIP	50 [66]	6 @ 80	0.02	5×10^7	150
MG593	Bi-QDIP	5.5 [6]	19 @ 80	0.43	3×10^9	140
		23.3 [13]	9 @ 80	0.05	1.2×10^9	140
Sample	Structure Type	λ_{Range} (μm)	R_P (A/W) @ T (K)	$\eta \times g$ (%)	D* (Jones) @ T (K)	T_{max} (K)
RU003	GaAs-HIWIP	up to 0.82	8 @ 20	120	6×10^9	20
		5-70	7 @ 20	16	5×10^9	20
79	Si-HIWIP	up to 1	0.3 @ 30	46	6.7×10^8	30
		5-40	1.4 @ 30	7	3.1×10^9	30
1158	GaN-HEIWIP	up to 0.36	0.015 @ 300	5.2	-	300
		8-14	0.8 @ 5.3	7.6	2.5×10^{10}	80
		54	6.5 @ 5.3	15	5.8×10^{10}	5.3

Table 6.1: A summary of selected detectors demonstrated in this work along with their specifications. λ_P, λ_{Range}, $\Delta\lambda/\lambda$, R_P, g, η, D*, T, and T_{max} stand for peak wavelength, response wavelength range, FWHM, peak responsivity, photoconductive gain, quantum efficiency, detectivity, operating temperature, and maximum reported operating temperature, respectively.

material systems. The weak UV response of the detector is due to the high absorption of UV radiation in the top-contact layer, which does not contribute to photocurrent. By etching out the top-contact layer, it is shown that the UV response of the detector can be enhanced. It is also possible to design a dual-band detector that can be used to measure the two components of the photocurrent generated by UV and IR radiation simultaneously. Moreover, this design allows the optimization of UV and IR responses independently. By adjusting the material or the alloy fraction, the threshold wavelength of the interband and intraband responses can be tailored to the selected wave bands.

The properties of selected detectors reported in this work are listed in Table 6.1. Each detector shows responses in two or three wavelength bands and has both advantages and disadvantages over the other detectors. Based on an analysis, it is apparent that QD-based detectors and HIWIP/HEIWIP detectors can be categorized into two groups. QD based detectors exhibit narrow response peaks, which can be represented by peak wavelength (λ_P) and full-width at half maximum (FWHM) ($\Delta\lambda/\lambda$), whereas the HIWIP/HEIWIP detectors respond in a broad wavelength region, which can be presented by the response wavelength range (λ_{Range}) or λ_0. QD-based detectors have lower conversion efficiency (product of quantum efficiency and gain) than that of HIWIP/HEIWIP detectors. This is attributed to the strong quantum confinement in QD-based detectors. On the other hand, the high conversion efficiency in HIWIP/HEIWIP detectors is partly associated with photoconductive gain in the structure. The QD-based detectors show the capability of high temperature operation. However, it is important to note that the operating temperature is associated with the operating wavelength.

This work demonstrate the feasibility of multi-band detectors that are based on different detector architectures and concepts. These detectors can be employed in numerous multi-band as well as single-band applications, as explained in Chapter 1. The primary advantage of terahertz T-QDIP and HIWIP/HEIWIP FIR detectors over the thermal detectors such as bolometers and TGS detectors is their fast response. T-QDIPs and HIWIP/HEIWIP detectors are photon detectors and do not use the slower thermalization processes, which is the primary detection mechanism in bolometers or TGS detectors. In comparison with the Si BIB detectors, the main advantage will be in the increased operating temperature, greatly reducing the cooling requirements. This is an important feature for space-based applications where moving from 20 K to higher temperatures is a major advantage. The selection of the most suitable detector has to be made based on its performance, operation conditions, and the nature of the application.

Bibliography

[1] D. A. Fay, A. M. Waxman, M. Aguilar, D. B. Ireland, J. P. Racamato, W. D. Ross, W. W. Streilein, and M. I. Braun, IEEE Proceedings of the Third International Conference on Information Fusion 2000 **1**, (2000).

[2] P. M. Alsing, D. A. Cardimona, D. H. Huang, T. Apostolova, W. R. Glass, and C. D. Castillo, Infrared Physics & Technology **50**, 89 (2007).

[3] Arnold Goldberg, Parvez N. Uppal, Michael Winn, Infrared Physics & Technology **44**, 427 (2003).

[4] C. J. Chen, K. K. Choi, W. H. Chang, and D. C. Tsui, Appl. Phys. Lett. **72**, 7 (1998).

[5] D. A. Fay, P. Ilardi, N. Sheldon, D. Grau, R. Biehl, and A. M. Waxman, SPIE Proc. **5802**, 154-165 (2005).

[6] David B. Law, Edward M. Carapezza, Christina J. Csanadi, Gerald D. Edwards, Todd M. Hintz, and Ronald M. Tong, SPIE **2938**, 288 (1997).

[7] Filip Neele, SPIE Proc. **5787**, 134 (2005).

[8] P. H. Siegel, IEEE Transaction on Microwave Theory and Techniques **50**, 910-928 (2002).

[9] Fabio Durante P. Alves, G. Karunasiri, N. Hanson, M. Byloos, H. C. Liu, A. Bezinger, and M. Buchanan, Infrared Physics & Technology **50**, 182 (2007).

[10] Sanjay Krishna, Darren Forman, Senthil Annamalai, Philip Dowd, Petros Varangis, Tom Tumolillo, Jr, Allen Gray, John Zilko, Kathy Sun, Mingguo Liu, Joe Campbell, and Daniel Carothers, Appl. Phys. Lett. **86**, 193501 (2005).

[11] Antoni Rogalski, Progress in Quantum Electronics **27**, 59 (2003).

[12] J. Urayama, T. B. Norris, J. Singh, and P. Bhattacharya, Phys. Rev. Lett. **86**, 4930 (2001).

[13] E. Kim, A. Madhukar, Z. Ye, and J. C. Campbell, Appl. Phys. Lett. **84**, 3277 (2004).

[14] B. Aslan, H. C. Liu, M. Korkusinski, S. J. Cheng, and P. Hawrylak, Appl. Phys. Lett. **82**, 639 (2003).

[15] B. Kochman, A.D. Stiff-Roberts, S. Chakrabarti, J.D. Phillips, S. Krishna, J. Singh and P. Bhattacharya, IEEE. J. Quant. Electron. **39**, 459-467 (2003).

[16] H. C. Liu, M. Gao, J. McCaffrey, Z. R. Wasilewski, and S. Fafard, Appl. Phys. Lett. **78**, 79-81 (2001).

[17] L. Jiang, Sheng S. Li, Nien-Tze Yeh, Jen-Inn Chyi, C. E. Ross, and K. S. Jones, Appl. Phys. Lett. **82**, 1986-1988 (2003).

[18] S. Raghavan, P. Rotella, A. Stintz, B. Fuchs, S. Krishna, C. Morath, D. A. Cardimona, and S.W. Kennerly, Appl. Phys. Lett. **81**, 1369-1371 (2002).

[19] S. Krishna, G. von Winckel, S. Raghavan, A. Stintz, G. Ariyawansa, S.G. Matsik, and A. G. U. Perera, Appl. Phys. Lett. **83**, 2745 (2003).

[20] S. D. Gunapala, S. V. Bandara, C. J. Hill, D. Z. Ting, J. K. Liu, S. B. Rafol, E. R. Blazejewski, J. M. Mumolo, S. A. Keo, S. Krishna, Y. -C. Chang, and C. A. Shott, Infrared Physics & Technology **50**, 149 (2007).

[21] S. Tsao, H. Lim, W. Zhang, and M. Razeghi, Appl. Phys. Lett. **90**, 201109 (2007).

[22] V. Ryzhii, Semicond. Sci. Technol. **11**, 759 (1996).

[23] R. Leon, G. M. Swift, B. Magness, W. A. Taylor, Y. S. Tang, K. L. Wang, P. Dowd, and Y. -H. Zhang, Appl. Phys. Lett. **76**, 2074 (2000).

[24] B. Aslan, H. C. Liu, M. Korkusinski, S. -J. Cheng, and P. Hawrylak, Appl. Phys. Lett. **82**, 630 (2002).

[25] D. Pal, L. Chen, and E. Towe, Appl. Phys. Lett. **82**, 4634 (2003).

[26] A. Sergeev, V. Mitin, M. Stroscio, Physica B **316**, 369 (2002).

[27] Zhengmao Ye, Joe C. Campbell, Zhonghui Chen, Eui-Tae Kim, and Anupam Madhukar, J. Appl. Phys. **92**, 7462 (2002).

[28] J. Phillips, K. Kamath, and P. Bhattacharya, Appl. Phys. Lett. **72**, 2020 (1998).

[29] S. Maimon, E. Finkman, and G. Bahir, Appl. Phys. Lett. **73**, 2003 (1998).

[30] D. Pan, E. Towe, and S. Kennerly, Appl. Phys. Lett. **73**, 1937 (1998).

[31] H. Lim, S. Tsao, W. Zhang, and M. Razeghi, Appl. Phys. Lett. **90**, 131112 (2007).

[32] Mary R. Matthews, Robert J. Steed, Mark D. Frogley, Chris C. Phillips, Ram S. Attaluri and Sanjay Krishna, Appl. Phys. Lett. **90**, 103519 (2007).

[33] C. -H. Lin, C. -Y. Yu, C. -Y. Peng, W. S. Ho, and C. W. Liu, J. Appl. Phys. **101**, 033117 (2007).

[34] S. Tong, Hyung-Jun Kim, and Kang L. Wang, Appl. Phys. Lett. **87**, 081104 (2005).

[35] Dongho Cha, Masaaki Ogawa, Christopher Chen, Seongku Kim, Jooyoung Lee, Kang L. Wang, Jiayu Wang, and Thomas P. Russell, Journal of Crystal Growth **301-302**, 833 (2007).

[36] A. Vardi, N. Akopian, G. Bahir, L. Doyennette, M. Tchernycheva, L. Nevou, F. H. Julien, F. Guillot and E. Monroy, Appl. Phys. Lett. **88**, 143101 (2006).

[37] A. Babinski, G. Ortner, S. Raymond, M. Potemski, M. Bayer, W. Sheng, P. Hawrylak, Z. Wasilewski, S. Fafard, and A. Forchel, Phys. Rev. B **74**, 075310 (2006).

[38] R. J. A. Hill, A. Patané, P. C. Main, L. Eaves, B. Gustafson, M. Henini, S. Tarucha and D. G. Austing, Appl. Phys. Lett. **79**, 3275 (2001).

[39] G. Ariyawansa, A. G. U. Perera, G. S. Raghavan, von Winckel, G. A. Stintz, and S. Krishna, IEEE Photon. Technol. Lett. **17**, 1064-1066 (2005).

[40] S. Krishna, S. Raghavan, G. von Winckel, P. Rotella, A. Stintz, D.Le, C. Morath and S.W. Kennerly, Appl. Phys. Lett. **82**, 2574 (2003).

[41] R. S. Attaluri, S. Annamalai, K. T. Posani, A. Stintz, and S. Krishna, Appl. Phys. Lett. **99**, 083105 (2006).

[42] A. Amtout, S. Raghavan, P. Rotella, G. von Winckel, A. Stintz, and S. Krishna, J. Appl. Phys. **96**, 3782-3786 (2004).

[43] B. F. Levine, J. Appl. Phys. **74**, R1 (1993).

[44] David M. -T. Kuo and Yia-Chung Chang, Physical Review B **67**, 035313-1 (2003).

[45] V. Apalkov, J. Appl. Phys. **100**, 076101 (2006).

[46] H. Jiang and J. Singh, Phys. Rev. B **56**, 4696 (1998).

[47] A. G. U. Perera, W. Z. Shen, S. G. Matsik, H. C. Liu, M. Buchanan, and W. J. Schaff, Appl. Phys. Lett. **72**, 1596-1598 (1998).

[48] P. Bhattacharya, X. H. Su, S. Chakrabarti, G. Ariyawansa, and A. G. U. Perera, Appl. Phys. Lett. **86**, 191106 (2005).

[49] B. Aslan, H. C. Liu, J. A. Gupta, Z. R. Wasiewski, G. C. Aers, S. Raymond, and M. Buchanan, Appl. Phys. Lett. **88**, 043103 (2006).

[50] X. H. Su, J. Yang, P. Bhattacharya, G. Ariyawansa, and A. G. U. Perera, Appl. Phys. Lett. **89**, 031117 (2006).

[51] X. Su, S. Chakrabarti, P. Bhattacharya, G. Ariyawansa, and A. G. U. Perera, IEEE J. Quantum Electron. **41**, 974 (2005).

[52] S. Chakrabarti, A. D. Stiff-Roberts, X. Su, P. Bhattacharya, G. Ariyawansa, and A. G. U. Perera, J. Phys D. Appl. Phys **38**, 2135-2141 (2005).

[53] F. Pulizzi, D. Walker, A. Patan, L. Eaves, M. Henini, D. Granados, J. M. Garcia, V. V. Rudenkov, P. C. M. Christianen, J. C. Maan, P. Offermans P. M. Koenraad, G. Hill, Phys. Rev. B **72**, 085309 (2005).

[54] E. Anemogiannis, N. Glytsis, T. K. Gaylord, IEEE. J. Quant. Electron. **33**, 742 (1997).

[55] K. K. Choi, B. F. Levine, R. J. Malik, J. Walker, and C. G. Bethea, Phys. Rev. B **35**, 4172-4175 (1987).

[56] K. K. Choi, B. F. Levine, C. G. Bethea, J. Walker, and R. J. Malik, Phys. Rev. Lett. **59**, 4172 (1987).

[57] A. Carbone and P. Mazzetti, J. Appl. Phys. **80(3)**, 1559 (1996).

[58] R. Rehm, H. Schneider, C. Schöonbein, M. Walther, Physica E **7**, 124 (2000).

[59] Y. Paltiel, N. Snapi, A. Zussman, and G. Jung, Appl. Phys. Lett. **87**, 231103 (2005).

[60] E. E. Haller, Infrared Phys. **35**, (1994).

[61] M. Suzuki and M. Tonouchi, Appl. Phys. Lett. **86**, 163504-3 (2005).

[62] H. C. Liu, C.Y. Song, A. J. Spring Thorpe, and J. C. Cao, Appl. Phys. Lett. **84**, 4068 (2004).

[63] M. B. M. Rinzan, A. G. U. Perera, S. G. Matsik, H. C. Liu, Z. R. Wasilewski, and M. Buchanan, Appl. Phys. Lett. **86**, 071112 (2005).

[64] D. G. Esaev, M. B. M. Rinzan, S. G. Matsik, A. G. U. Perera, H. C. Liu, B. N. Zhonkov, V. I. Gavrilenko, and A. A. Belyanin, J. Appl. Phys. **95**, 512 (2004).

[65] H. Luo, H. C. Liu, C. Y. Song, and Z. R. Wasilewski, Appl. Phys. Lett. **86**, 231103 (2005).

[66] M. Grundmann, O. Stier, and D. Bimberg, Phys. Rev. B **52**, 11969 (1995).

[67] S. Chakrabarti, X. H. Su, P. Bhattacharya, G. Ariyawansa, and A. G. U. Perera, IEEE Photon. Technol. Lett. **17**, 178 (2005).

[68] W. Z. Shen, A. G. U. Perera, H. C. Liu, M. Buchanan, and W. J. Schaff, Appl. Phys. Lett. **71**, 2677 (1997).

[69] D. G. Esaev, S. G. Matsik, M. B. M. Rinzan, A. G. U. Perera, H. C. Liu, and M. Buchanan, J. Appl. Phys. **93**, 1879 (2003).

[70] H. C. Liu, P. H. Wilson, M. Lamm, A. G. Steele, Z. R. Wasilewski, Jianmerng Li, M. Buchanan, and J. G. Simmonsa, Appl. Phys. Lett. **64**, 475 (1994).

[71] H. C. Liu, C. Y. Song, A. Shen, M. Gao, Z. R. Wasilewski, and M. Buchanan, Appl. Phys. Lett. **77**, 2437 (2000).

[72] M. P. Touse, G. Karunasiri, K. R. Lantz, H. Li, and T. Mei, Appl. Phys. Lett. **86**, 093501-1 (2005).

[73] K. K. Choi, P. G. Newman, P. A. Folkes and G. J. Iafrate, Appl. Phys. Lett. **54**, 359 (1989).

[74] A. G. U. Perera, H. X. Yuan, and M. H. Francombe, J. Appl. Phys. **77**, 915 (1995).

[75] S. Adachi, *GaAs and Related Materials* in (WorldScientific, Singapore, 1994).

[76] M. D. Sturge, Physical Review **127**, 768 (1962).

[77] G. Ariyawansa, M. B. M. Rinzan, D. G. Esaev, S. G. Matsik, A. G. U. Perera, H. C. Liu, B. N. Zvonkov, and V. I. Gavrilenko, Appl. Phys. Lett. **86**, 143510-3 (2005).

[78] James E. Huffman, A. G. Crouse, B. L. Halleck, T. V. Downes, and Terry L. Herter, J. Appl. Phys. **72**, 273-275 (1992).

[79] A. G. U. Perera, W. Z. Shen, H. C. Liu, M. Buchanan, M. O. Tanner, and K. L. Wang, Appl. Phys. Lett. **72**, 2307 (1998).

[80] F. Merlet, B. Pajot, Ph. Arcas, and A. M. Jean-Louis, Phys. Rev. B **12**, 3297 (1975).

[81] P. J. Dean, Y. Yafet, and J. R. Haynes, Phys. Rev. **184**, 837 (1969).

[82] F. Raissia, and N. A. Sheenib, Sensors and Actuators A **104**, 117 (2003).

[83] Aaron R. Hawkins, Thomas E. Reynolds, Derek R. England, Dubravko I. Babic, Mark J. Mondry, Klaus Streubel, and John E. Bowers, Appl. Phys. Lett. **68**, 3692 (1996).

[84] M. D. Petroff, M. G. Stapelbroek, and W. A. Kleinhans, Appl. Phys. Lett. **51**, 406 (1987).

[85] R. F. Kirkman, R. A. Stradling, and P. J. Lin-Chung, J. Phys. C **11**, 419 (1978).

[86] A. Onton, P. Fisher, and A. K. Ramdas, Phys. Rev. **163**, 686703 (1967).

[87] J. Li, K. K. Choi, and D. C. Tsui, Appl. Phys. Lett. **86**, 211114 (2005).

[88] Z. Mi, P. Bhattacharya, and S. Fathpour, Appl. Phys. Lett. **86**, 153109 (2005).

[89] R. Katterloher, L. Barl, J. Beeman, E. Czech, D. Engemann, O. Frenzl, N. Haegal, E. E. Haller, Th. Henning, L. Hermans, G. Jakob, M. Konuma, and G. Pilbratt, Proc. of SPIE **3354**, 57 (1998).

[90] Sarath D. Gunapala, Sumith V. Bandara, John K. Liu, Sir B. Rafol, and Jason M. Mumolo, Proc. SPIE **5234**, 272 (2004).

[91] M. Asif Khan, J. N. Kuznia, D. T. Olson, M. Blasingame, and A. R. Bhattarai, Appl. Phys. Lett. **63**, 2455 (1993).

[92] D. Walker, X. Zhang, P. Kung, A. Saxler, S. Javadpour, J. Xu, and M. Razeghi, Appl. Phys. Lett. **68(15)**, 2100 (1996).

[93] Madalina Furis, A. N. Cartwright, Hong Wu, and William J. Schaff, Appl. Phys. Lett. **83**, 3486 (2003).

[94] S. K. Zhang, W. B. Wang, I. Shtau, F. Yun, L. He, H. Morko, X. Zhou, M. Tamargo, and R. R. Alfano, Appl. Phys. Lett. **81**, 4862 (2002).

[95] J. P. Zhang, X. Hu, Yu. Bilenko, J. Deng, A. Lunev, M. S. Shur, R. Gaska, M. Shatalov, J. W. Yang, and M. A. Khan, Appl. Phys. Lett. **85**, 5532 (2004).

[96] V. D. Jovanovic, D. Indjin, Z. Ikonic, and P. Harrison, Appl. Phys. Lett. **84**, 2995 (2004).

[97] N. Biyikli, T. Kartaloglu, O. Aytur, I. Kimukin, and E. Ozbay, MRS Internet J. Nitride Semicond. Res. **8**, (2003).

[98] Claire Gmachl, Hock M. Ng, and Alfred Y. Cho, Appl. Phys. Lett. **77**, 334 (2000).

[99] G. Ariyawansa, M. B. M. Rinzan, M. Alevli, M. Strassburg, N. Dietz, A. G. U. Perera, S. G. Matsik, A. Asghar, I. T. Ferguson, H. Luo, A. Bezinger, and H. C. Liu, Appl. Phys. Lett. **89**, 091113 (2006).

[100] A.G.U. Perera, G. Ariyawansa, M.B.M. Rinzan, M. Stevens, M. Alevli, N. Dietz, S. G. Matsik, A. Asghar, I. T. Ferguson, H. Luo, A. Bezinger, H. C. Liu, Infrared Physics & Technology **50**, 142 (2007).

[101] G. Ariyawansa, M. B. M. Rinzan, S. G. Matsik, G. Hastings, A. G. U. Perera, H. C. Liu, M. Buchanan, G. I. Sproule, V. I. Gavrilenko, and V. P. Kuznetsov, Appl. Phys. Lett. **89**, 061112 (2006).

[102] David Starikov, Chris Boney, Rajeev Pillai, and Abdelhak Bensaoula, SlconlO4- Senson for Industry Conference , 36 (2004).

[103] S. G. Matsik, M. B. M. Rinzan, D. G. Esaev, A. G. U. Perera, H. C. Liu, and M. Buchanan, Appl. Phys. Lett. **84**, 3435 (2004).

[104] Takahiro Kawashima, Hisashi Yoshikawa, Sadao Adachi, Shunro Fuke, and Kohji Ohtsuka, J. Appl. Phys **82**, 3528 (1997).

[105] A. B. Djurisic and E. Herbert Li, Appl. Phys. Lett. **73**, 868 (1998).

[106] Ü. Özgür, G. Webb-Wood, H. O. Everitt, F. Yun, and H. Morkoç, Appl. Phys. Lett. **79**, 4103 (2001).

[107] D. G. Esaev, M. B. M. Rinzan, S. G. Matsik, and A. G. U. Perera, J. Appl. Phys. **96**, 4588 (2004).

[108] O. Katz, V. Garber, B. Meyler, G. Bahir, and J. Salzman, Appl. Phys. Lett. **80**, 347 (2002).

[109] V. Bougrov, M. Levinshtein, S. Rumyantsev, and A. Zubrilov, *Gallium Nitride (GaN)* in edited by (edited by M. E. Levinshtein, S. L. Rumyantsev, M. S. Shur, John Wiley & Sons, Inc., NY, 2001).

[110] M. Sumiya, K. Yoshimura, K. Ohtsuka, and S. Fuke, Appl. Phys. Lett. **76**, 2098 (2000).

[111] P. Bogusławski, E. L. Briggs and J. Bernholc, Appl. Phys. Lett. **69(2)**, 233 (1996).

[112] Y. J. Wang, R. Kaplan, H. K. Ng, K. Doverspike, D. K. Gaskill, T. Ikedo, I. Akasaki, and H. Amono, Appl. Phys. Lett. **79**, 8007 (1977).

[113] W. J. Moore, J. A. Freitas, Jr., and R. J. Molnar, Appl. Phys. Lett. **56**, 12 073 (1997).

[114] A. G. U. Perera, W. Z. Shen, H. C. Liu, M. Buchanan, and W. J. Schaff, ECS Proc. **98-21**, 194 (1999).

[115] A. G. U. Perera, W. Z. Shen, M. Ershov, H. C. Liu, M. Buchanan, S. D. Gunapala, S. V. Bandara, J. K. Liu, H. H. Ye and W. J. Schaff, J. Vac. Sci. Tech. A **18**, 597 (2000).

Appendix A

Device Characterization

A.1 I-V-T and C-V-T Measurements

The devices are mounted on chip carriers with silver epoxy and individual devices are wire bonded to separate leads of the carriers. These structures are then mounted in a variable temperature liquid He cryostat. The I-V-T characteristics are measured with a Keithley 2400 Source Meter. Up to 10 mesas can be mounted and a computer controlled Keithley Switch System is used to connect one mesa at a time to the source meter, as shown in Fig.A.1. The setup is controlled using an inhouse software program. Measurements are made for both bias polarities, where a positive bias denotes a positive polarity on the top-contact. For measurements under dark conditions, the device is wrapped with a shielding material (several layers of Aluminum foil) and another 77 K cold shield is also used. A KRS window is used for 300 K background photocurrent measurements and the detector is open to the 300 K background. Data, which consist of voltage and current under a given temperature, are automatically saved in Excel files. For C-V-T measurements, an HP

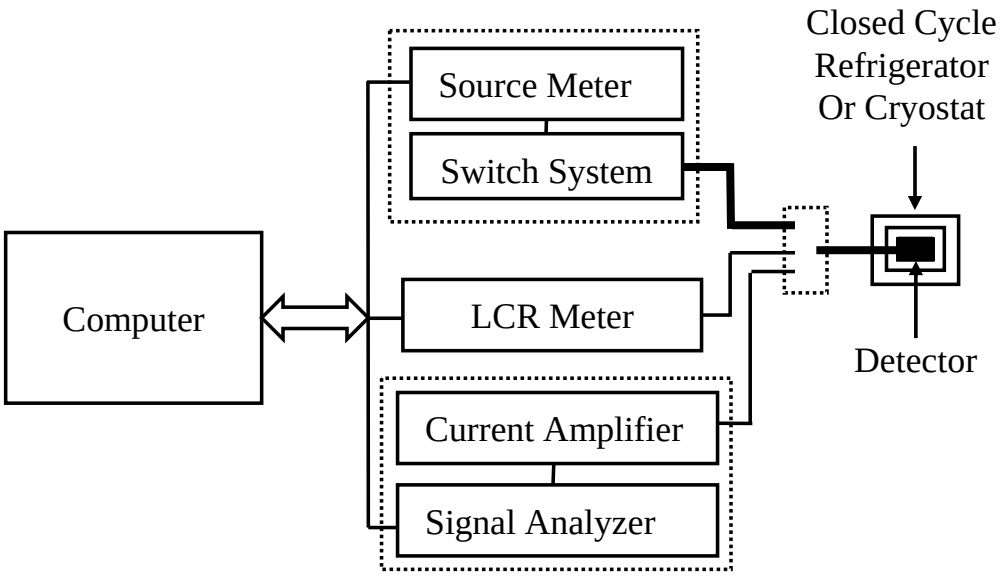

Figure A.1: Block diagram of the experimental setup for I-V-T (source-meter/switch-system), C-V-T (LCR-meter), and noise measurements (current-amplifier/signal-analyzer).

4284A high precision LCR Meter is used and a block diagram of the setup is also shown in Fig.A.1. Data collection is carried out using an inhouse software program and the data file contains voltage, capacitance, frequency, inductance, and resistance.

The BLIP temperature is determined based on the dark- and photocurrents (300 K background). The BLIP temperature is the temperature at which the dark current starts to dominate the photocurrent for a given bias voltage.

A.2 Spectral Response Measurements and Calibration

The spectral response of the device under test and a Si composite bolometer with a known sensitivity, are measured with a Perkin Elmer System 2000 Fourier Transform Infrared (FTIR) Spectrometer. The two spectra are obtained concurrently with the same combination of optical windows, beamsplitter, and filters, so that the optical path is identical. This can be effectively done using a modified dewar setup in which two detectors are mounted, as shown in Fig. A.2. The calibration process includes several steps as discussed below.

The device spectrum (I_d) is then divided by the bolometer spectrum (I_b) and multiplied by the bolometer sensitivity (S_0) to obtain the voltage responsivity of the device:

$$R(V/W) = \frac{GS_0 I_d}{I_b}. \tag{A.1}$$

Here G is a geometrical factor which corrects for differences in the radiation-incident-area of the detector and the bolometer. To obtain the current responsivity, the voltage responsivity is divided by the effective resistance. As the detector and the load resistor act as a voltage divider for the photocurrent, the effective resistance R_e is the parallel combination of the

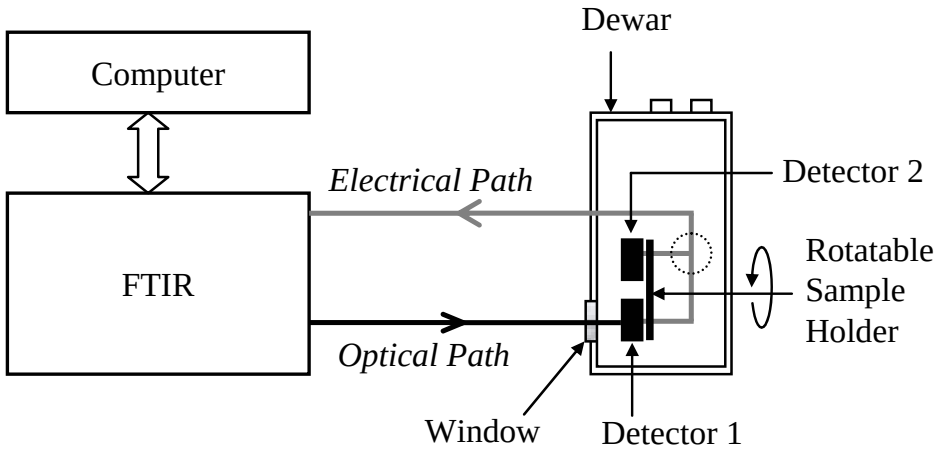

Figure A.2: Diagram of the experimental setup for IR spectral measurements. Optical and electrical paths are denoted by dark and light arrows, respectively. Two detectors (detector 1 and detector 2) can be mounted in the dewar and one detector is chosen at a time to measure the spectral response. By this way, the spectral responses of both the device under test and the bolometer can be measured concurrently so that the optical path for both is the same.

load R_l and the detector dynamic resistance $R_d = dV/dI$, yielding $R_e = R_l R_d/(R_l + R_d)$. The final current responsivity is given by

$$R(A/W) = \frac{GS_0 I_d(R_l + R_d)}{(I_b R_l R_d)}. \tag{A.2}$$

A.3 Noise Measurements and Detectivity

The specific detectivity (D^*) of the devices at different temperatures and applied biases is obtained from the measured peak responsivity (R_p), noise current density (S_i), and the illuminated area of the detector (A). The latter are measured with a dual channel Fast Fourier Transform (FFT) signal analyzer and a SR570 low noise current pre-amplifier, as shown in Fig. A.1. A thick copper plate at the device temperature is used as the radiation block to provide the dark conditions for the measurements. The value of D^* is calculated from

$$D^*(\text{Jones}) = \frac{R_p A^{1/2}}{S_i^{1/2}}, \tag{A.3}$$

with $S_i = i_n^2/\Delta f$, where i_n is the noise current, and Δf is the noise band width.

The quantum efficiency is given by

$$\eta = \frac{hcR_p}{gq\lambda}, \tag{A.4}$$

where h is the Planck constant, c is the speed of light, g is the photoconductive gain, q is the electron charge, and λ is the wavelength.

The photoconductive gain (g) can be defined as the ratio of the total collected carriers to the total excited carriers by both thermal and photo excitations. For QDIPs, assuming carrier emission and capture are due to the generationrecombination process, g

can be derived experimentally from[15]

$$g = \frac{S_i}{4qI_d} + \frac{1}{2N}, \tag{A.5}$$

where I_d is the measured dark current and N is the number of QD layers.

For HIWIPs and HEIWIPs, this can be expressed as,

$$g = \frac{S_i}{4qI_d}. \tag{A.6}$$

A.4 UV/IR Dual-Band Spectrometer

A typical UV spectrometer setup consists of a UV source, a grating monochromator, an optical chopper, a lock-in amplifier, and focusing elements. The UV signal is modulated by the chopper, and the photocurrent is then measured using the lock-in amplifier. The monochromator and lock-in amplifier are both computer controlled. The system is calibrated by use of a photomultiplier tube and a standard calibration lamp. In order to perform simultaneous response measurements for UV and IR radiation, a UV-IR dual response spectrometer setup was built using two monochromators, two sources (UV and IR), two lock-in amplifiers, and UV and IR focusing elements as shown in Fig. A.3. Both UV and IR incident light beams were modulated (at two separate frequencies) and were measured simultaneously with two lock-in amplifiers. This approach allows measurements using any desired combination of UV and IR illumination. The dual response of the detector can be measured in two different scanning modes; i) the full range IR response is measured when UV response at a constant wavelength is measured with time, ii) the full range UV response is measured when IR response at a constant wavelength is measured with time.

Different versions of Lab View programs (see Appendix B) are used to control the setup. The calibration of the spectra uses the same procedure explained in the previous section, however, in the UV region, a photomultiplier tube with known sensitivity is used instead of the bolometer.

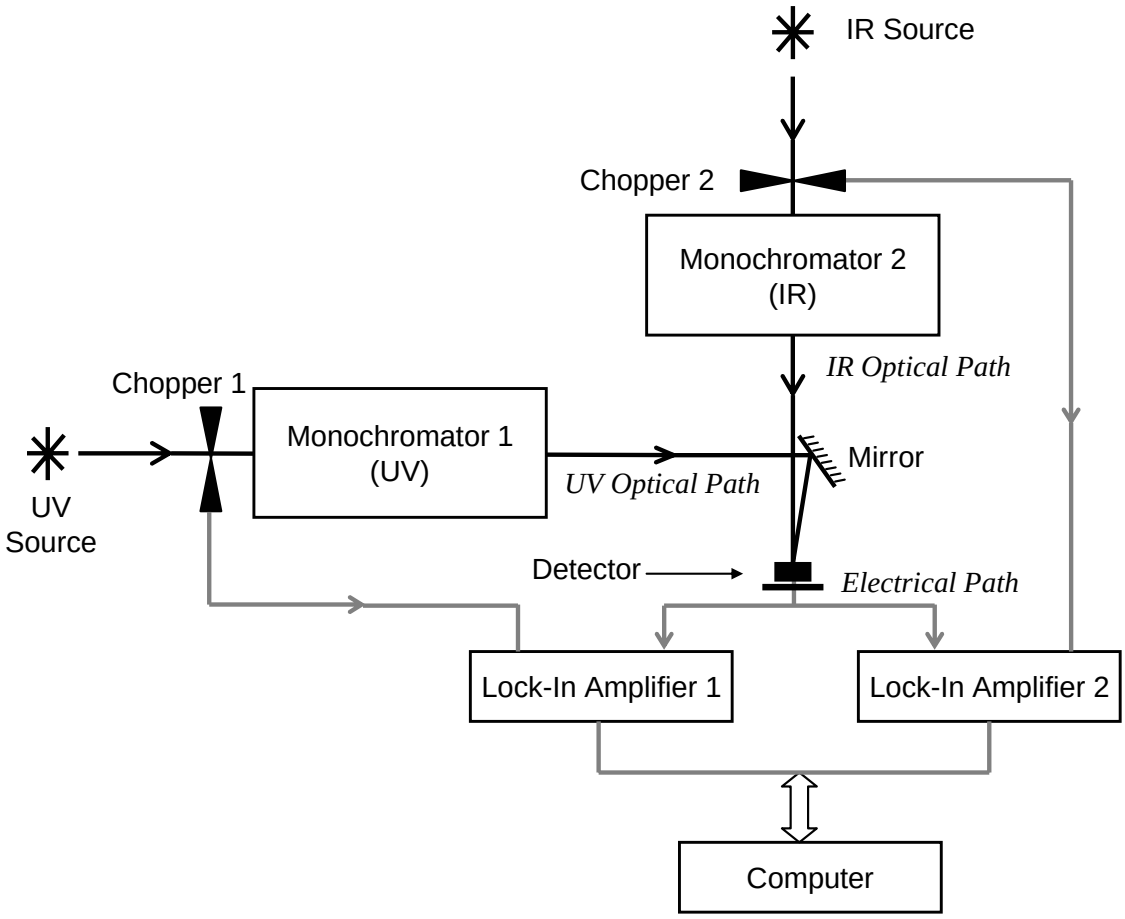

Figure A.3: The experimental setup for measuring the UV and IR responses simultaneously. The dark lines indicate the light paths, while the light lines indicate the electrical path. The two monchromators and lock-in amplifiers are separately controlled by the computer to obtain both responses.

Appendix B

Software Development with LabView 7.1: UV/IR Dual-Band Spectrometer

The dual-band spectrometer is controlled using an inhouse software program developed with LabVIEW 7.1. The main front panel and its functions are explained in following figures. The setup is a combination of UV and IR spectrometers. The UV and IR components are controlled simultaneously. Also the UV and IR response curves are visualized in two panels. There are two scanning modes that user has to select; (i) detector response with changing wavelength, and (ii) detector response with time. In general, when one component of the response is scanned over the wavelength, the other component is scanned over the time. Before starting the scan, all the parameters have to be set properly. Although only two major panels are shown in this section, there are a number of sub-VIs (virtual-interfaces) and popup windows, which provide sufficient instructions during the runtime, linked with the main front panel.

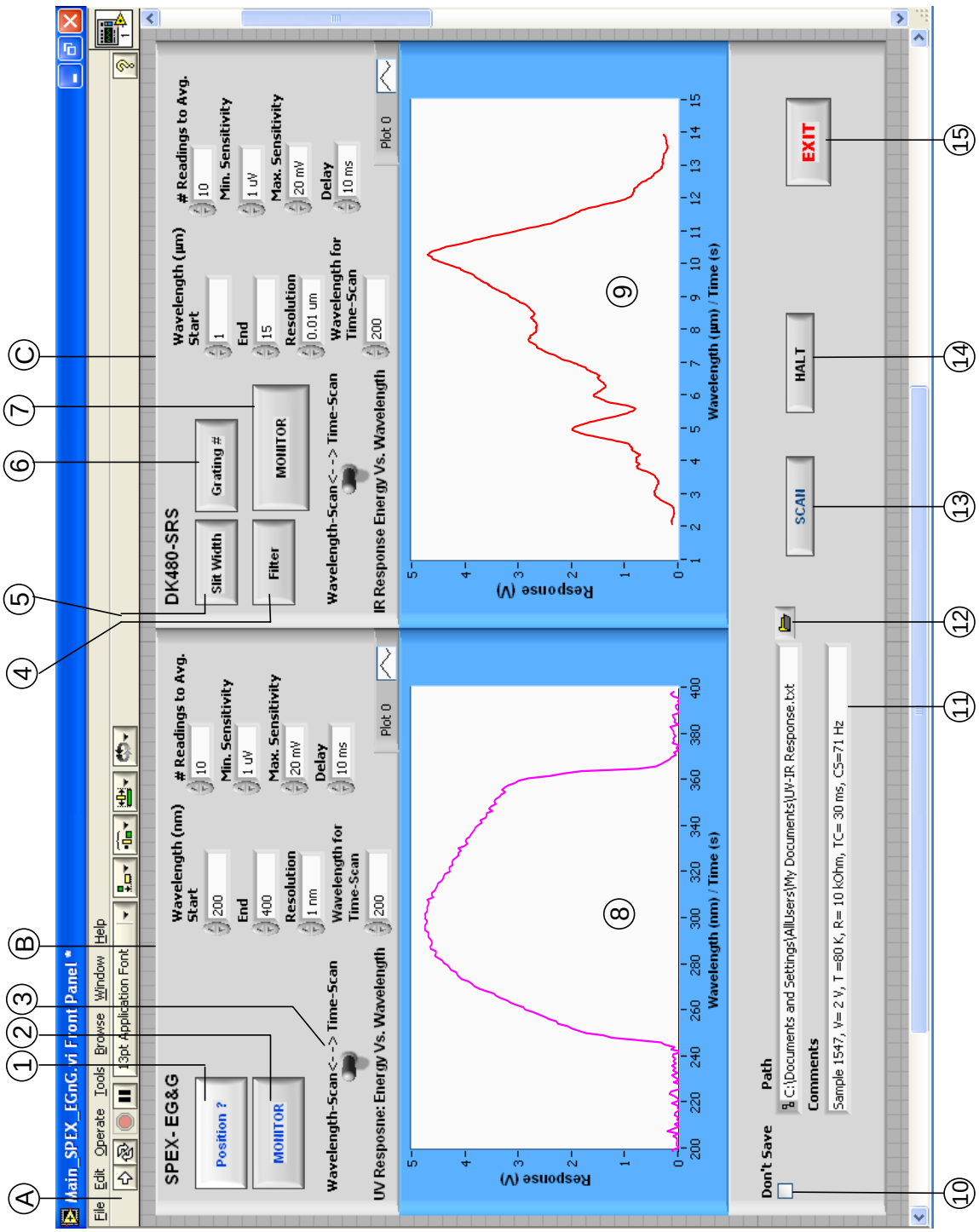

The main front panel of the UV/IR dual-band spectrometer software.

Ⓐ	LabVIEW menu bar.	⑧	Graph for UV response (Response Vs Wavelength OR Response Vs time).
Ⓑ	UV spectrometer control panel: SPEX monochromator and EG&G lock-in amplifier.	⑨	Graph for IR response (Response Vs Wavelength OR Response Vs time).
Ⓒ	UV spectrometer control panel: DK480 monochromator and SRS lock-in amplifier.	⑩	Check if you don't need the data to be saved.
①	Check/Record the current position in the SPEX monochromator.	⑪	Comments related to the scan (sample number, scan parameters, etc.).
②	Monitor the variation of the detector response at a given wavelength with time.	⑫	Specify the location for data files.
③	Select the scan-mode: Response against wavelength OR variation with time at a given wavelength (specify in "Wavelength for time-scan").	⑬	Start the scan.
④	Select a filter in DK480.	⑭	Stop the scan.
⑤	Set the entrance and exit slit widths in DK480.	⑮	Exit the program. Note: stop the scan in progress before exciting.
⑥	Select the grating in DK480 (UV, VIS-NIR, or MIR).		
⑦	Monitor the variation of the detector response at a given wavelength with time.		

Functions of sub-modules and scan parameters to be set in the main front panel of the UV/IR dual-band spectrometer software.

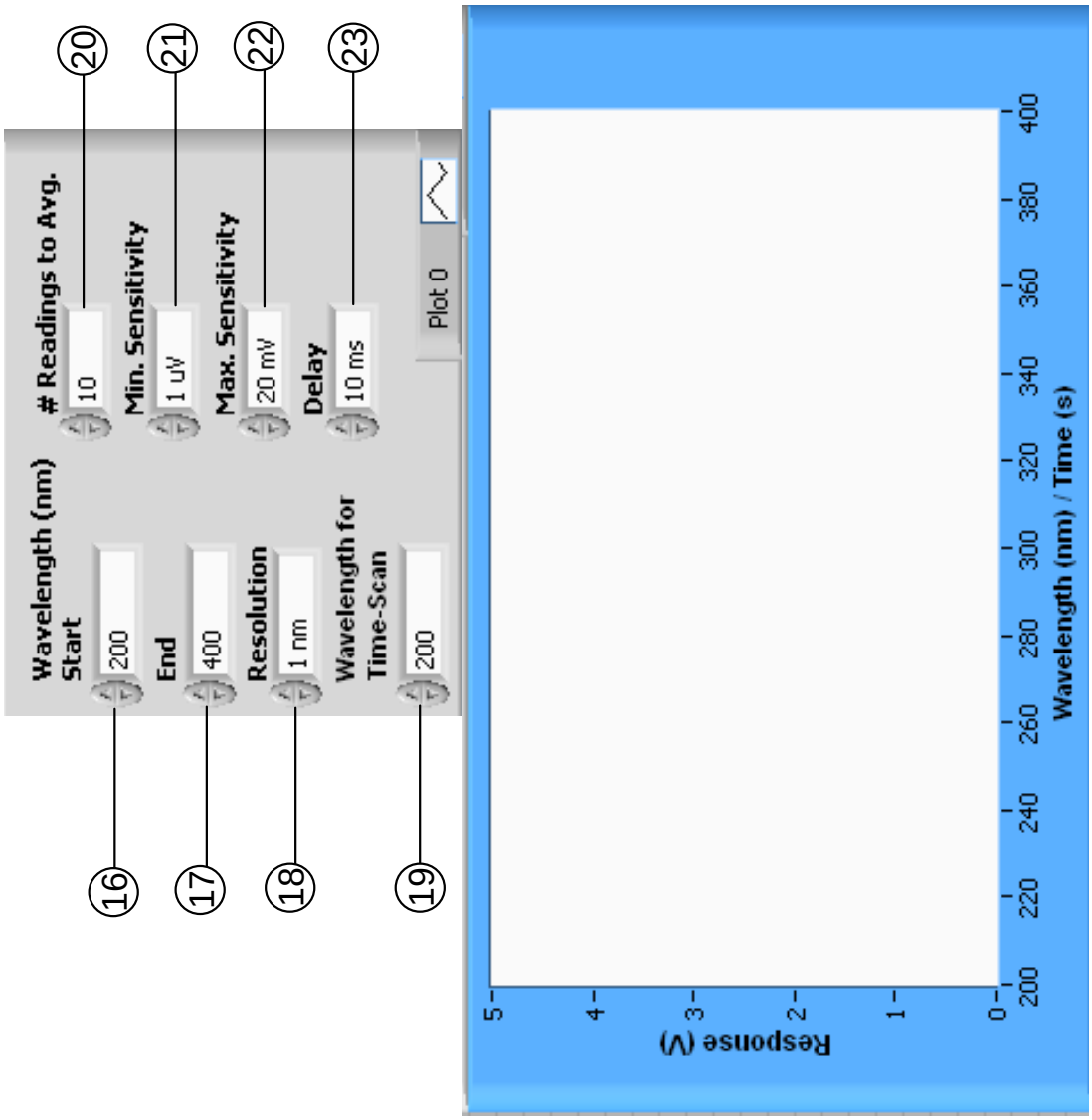

Expanded view of the front panel of the UV/IR dual-band spectrometer software, showing scan parameters to be set.

⑯	Specify the starting wavelength in the scan.	⑳	Specify the number of readings to average. Averaging is done with a gradient check.
⑰	Specify the ending wavelength in the scan.	㉑	Specify the minimum sensitivity allowed in the lock-in amplifier.
⑱	Specify the step wavelength (resolution).	㉒	Specify the maximum sensitivity allowed in the lock-in amplifier.
⑲	Specify the wavelength to be fixed for "Time-Scan".	㉓	Specify the time delay between two measurements (note: the chopper speed has to be considered).

Scan parameters to be set in the main front panel of the UV/IR dual-band spectrometer software.

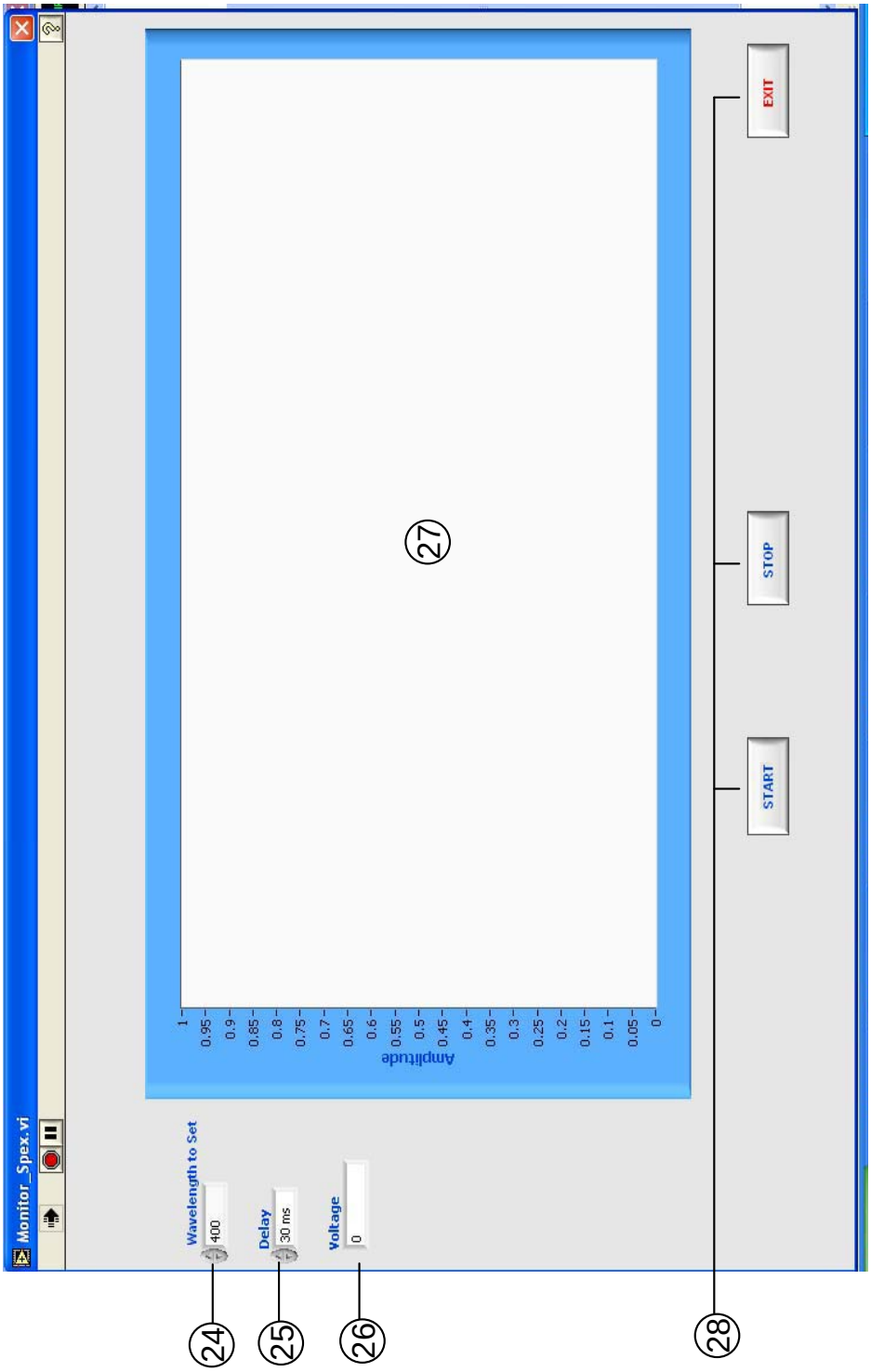

"Monitor" popup window in the UV/IR dual-band spectrometer software.

㉔	Specify the wavelength to be set.	㉖	Response of the detector in Volts.
㉕	Specify the delay between measurements.	㉗	Graph showing the variation of the response (in Volts) with time.
㉘	Start, stop monitoring, and exit the sub program.		

Parameters to be set in the "Monitor" popup window in the UV/IR dual-band spectrometer software.

Appendix C

Programs Developed with MATLAB 6.5.1

C.1 Transfer Matrix Method

In this section, implementation of a model developed to find the solutions for the energy levels and transmission probability in a quantum heterostructure is given. The model was proposed by Anemogiannis et al.[54] The program can be used to obtain the possible energy states in a 2-D quantum structure, the lifetime and transmission probability corresponding to each energy state. A basic description of the model and some results obtained using this program are given in Section 3.2. In order to use the program, all the parameters (layer thickness, potential energy, and effective electron mass) needed to construct the band diagram (see Fig. 3.2 (b)) are required.

This program is compatible with MATLAB Version 6.5.1 or higher.

```
%*************************************************************************
% ****** Calculation of Transmission Probability in a 2D Quantum Heterostructure*******
%*************************************************************************

hbar=3.29e-4; %h bar divided by 2 in eV ps

%-------------------------------------------------------------------------------------------------------

%Potential@ 0 V Bias
Eofs=[0,0.11811, -0.1919, 0.11811, -0.46571, 0.11811, -0.1919, 0.11811, 0];

% Layer thickness
d=1e-9*[1,3.0, 2.5, 3.0, 2.0, 3.0, 3.5, 3.0, 4];

m* = m0 x m
m=[0.067, 0.0919, 0.07011, 0.0919, 0.05974, 0.0919, 0.07011, 0.0919, 0.067]; %

%-------------------------------------------------------------------------------------------------------

max=9;
Bias=-0.200; %eV

Eres1=0.188; %0.2
Ew=Eres1;     % Input

% ---------------------- Calculation of the Band Diagram under Bias V -----------------------------

th=d/1e-10;
dd = zeros(1,max);
Vofs = zeros(1,max);
Eqd=zeros(1,2);

sum=0;

          for count=1:max,
             dd(count)=sum+th(count)/2;
             sum=sum+th(count);
          end

PE = zeros(1,sum);
z = zeros(1,sum);


EF=Bias/sum;
```

```
count=1;

        for q=1:max,
           for s=1:th(q),
              z(count)=count-1;
              PE(count)=EF*(sum-count-1)+Eofs(q);
              count=count+1;
           end
        end

        count=1;
        for q=1:sum,
           if count<=max
              if q>=dd(count)
                 Vofs(count)=PE(q);
                 count=count+1;
              end
            end
end

% ------------------------- Calculating the Transmission Probability -------------------------------
% Vofs is the potential matrix under bias V
V=Vofs;

index=max;

   fileno=1;
   na=num2str(fileno);
   name = strcat('T_E_Design',na,'.txt'); % Output file for T(E)
   fid1 = fopen(name,'w');

   name = strcat('DarkCurrent.txt'); % Output file for dark current
   fid2 = fopen(name,'w');

              m0= 9.109e-31; %kg 510998.903 eV
              e0= 1.6e-19; % electron charge
              h= 6.626e-34; % SI %4.135667e-15; %eV
              Nd=5e14; %m-2
              sigma=0.040/2.3; %meV
              Lp=sum*1e-8; %in cm
              weteffm=m(4)*m0;
              bareffm=m(2)*m0;
              kb=8.61738573e-05; %eV
```

```
            Te=77; %K  % Input
            Area= p1*0.03^2; % cm^2

   E=-1.0;

   for q=1:2000,

            k=5.125e9*sqrt(m.*(E-V)); %m

            for c=1:index-1,
               m11(c)=0.5*(1+k(c+1)*m(c)/m(c+1)/k(c))*exp(-i*k(c)*d(c));
               m12(c)=0.5*(1-k(c+1)*m(c)/m(c+1)/k(c))*exp(-i*k(c)*d(c));
               m21(c)=0.5*(1-k(c+1)*m(c)/m(c+1)/k(c))*exp(i*k(c)*d(c));
               m22(c)=0.5*(1+k(c+1)*m(c)/m(c+1)/k(c))*exp(i*k(c)*d(c));
            end

            m1 = [m11(1),m12(1);m21(1),m22(1)];
            m2 = [m11(2),m12(2);m21(2),m22(2)];
            m3 = [m11(3),m12(3);m21(3),m22(3)];
            m4 = [m11(4),m12(4);m21(4),m22(4)];
            m5 = [m11(5),m12(5);m21(5),m22(5)];
            m6 = [m11(6),m12(6);m21(6),m22(6)];
            m7 = [m11(7),m12(7);m21(7),m22(7)];
            m8 = [m11(8),m12(8);m21(8),m22(8)];

            M=m1*m2*m3*m4*m5*m6*m7*m8;

            t=1/M(1,1);
            T=(k(index)*m(1)/k(1)/m(index))*abs(t)^2;

            fprintf(fid1, '%12.8f\t%12.8e\n', E,abs(T));  % Printing T(E)

% ---------------------------- Calculating the dark current at bias V ----------------------------

            Fermi=(V(3)+V(5))/2-0.088;  % Input

            Eqd(1)=Eres1-1.240/10; % Input

            Nqd=2*Nd/(Lp*2.5066*sigma)*exp(-(E-Eqd(1))^2/(2*sigma^2));

            temp=th(1)+th(2)+th(3);
            Ec=PE(temp);

            if (E-Ew)>=0
```

```
    Nw=4*pi*weteffm/(Lp*h^2)*1e-19;
  else
    Nw=0;
  end

  if (E-Ec)>=0
    Nb=8*pi*1.4142*bareffm^1.5/h^3*sqrt((E-Ec)*1.6e-19)*1e-19;
  else
    Nb=0;
  end

  f=1/(exp((E-Fermi)/(kb*Te))+1);

  N=(Nqd+Nw+Nb)*1e-6;

  Nem=N*f*T;

 mu=1000; %cm2 V-1 s-1
 Vs= 1e7; %cm/s
 v = mu*F/(sqrt(1+(mu*F/Vs)^2));

 Id = e0 * v * Nem * Area % Dark current at bias V

 fprintf(fid2, '%12.8f\t%12.8e\n', E,Id);  % Printing Id at field EF;

% Note: In order to obtain the total current, Id sould be % integrated over E, using standard
% integration function (Eg: Origin).


  E=E+0.001; %eV
 end

 F=EF*1e8; %V/cm

fclose(fid);
```

```
%*************************************************************************
% ********************** Calculation of the Wavefunction *******************
%*************************************************************************


V=[0, 0.09033, 0, -0.46571, 0, 0.11811, -0.0919, 0.11811, 0]; % Potential at V
d=1e-9*[4.0, 4.0, 4.0, 2.0, 1.0, 3.0, 5.0, 3.0, 40.0]; % Layer thickness
m=[0.067, 0.0753, 0.067, 0.04822, 0.067, 0.0919, 0.07702, 0.0919, 0.067]; % m*= m x m0


index=9; %1..7
mm(:,:,:)=0;

E=0.0108; %meV

na=num2str(1);
name = strcat('Design1WF',na,'.txt'); % Output file name
fid = fopen(name,'w');

k=5.125e9*sqrt(m.*(E-V)); %m

                for c=1:index-1,
                   m11(c)=0.5*(1+k(c+1)*m(c)/m(c+1)/k(c))*exp(-i*k(c)*d(c));
                   m12(c)=0.5*(1-k(c+1)*m(c)/m(c+1)/k(c))*exp(-i*k(c)*d(c));
                   m21(c)=0.5*(1-k(c+1)*m(c)/m(c+1)/k(c))*exp(i*k(c)*d(c));
                   m22(c)=0.5*(1+k(c+1)*m(c)/m(c+1)/k(c))*exp(i*k(c)*d(c));
                end

                for c=1:index-1,
                   mm(c,1,1) = m11(c);
                   mm(c,1,2) = m12(c);
                   mm(c,2,1) = m21(c);
                   mm(c,2,2) = m22(c);
                end

      A=zeros(1,index);
      B=zeros(1,index);
      A(1)=1;
      B(1)=0;

                for c=1:index-1,
                   b=[A(c);B(c)];
                   MM=[mm(c,1,1), mm(c,1,2); mm(c,2,1), mm(c,2,2)];
                   x=inv(MM)*b;
```

```
                A(c+1)=x(1);
                B(c+1)=x(2);
            end

        sum=0;
        for q=1:index
            sum=sum+d(q);
        end

 step=0.01e-9;
 max=round(sum/step);

 dd=zeros(1,index);
dd(1)=d(1);

        for c=2:index,
            dd(c)=dd(c-1)+d(c);
        end

 z=0;
 c=1;
temp=round(dd(1)/step);

        for q=1:temp,
            si=A(c)*exp(i*k(c)*(z-dd(1)))+B(c)*exp(-i*k(c)*(z-dd(1)));
            fprintf(fid, '%6.2e\t%12.8f\n', z,si);
            z=z+step;
        end

 c=2;
        for q=1:(max-temp),

            if z>=dd(c)
                c=c+1;
            end

            si=A(c)*exp(i*k(c)*(z-dd(c-1)))+B(c)*exp(-i*k(c)*(z-dd(c-1)));
            fprintf(fid, '%6.2e\t%12.8f\n', z/1e-10,si); % Printing the wavefunction data
            z=z+step;
        end

fclose(fid);
```

C.2 Calculation of Physical Constants for Hexagonal GaN and UV Responsivity

In this section, implementation of a model developed to obtain physical constants for hexagonal GaN are given. The model was proposed by Kawashima et al.[104] A basic description of the model and some results obtained using this program is given in Section 6.3. In order to calculate the UV responsivity, the program first calculates the dielectric function and the absorption coefficient. Then the UV responsivity is calculated using the model in Ref. [69]

This program is compatible with MATLAB Version 6.5.1 or higher.

```
%*************************************************************************
% ********** Calculation of Physical Constants for Hexagonal GaN**********
%*************************************************************************

e_in=0.426;
A=41.251; %eV

B1=[0.778,0.103,0.920]; %eV
Bx1=[2.042,1.024,1.997]; %eV
Tau00=0.287; %eV
Tau11=[0.743,0.428,0.440]; %eV
a0=1.241;
a1=[0.240,0.011,0.005];
G2D1=[0.0003,0.356,1.962]; %eV
E0=3.750; %eV
E1=[6.010,8.182,8.761]; %eV
Aex0=0.249; %eV
G3D0=0.030; %eV

% e = dielectric constant
% l = wavelength in nm, lmin-lmax = wavelength range
% E = Energy

lmin=130;
lmax=600;
index=lmax+1-lmin;
l = zeros(1,index);
E = zeros(1,index);

        for t = 1:index,
           l(t) = lmin-1+t; %nm
           E(t) = 1240.0/l(t); %eV
        end

%Calculation of epsilone0

Tau0=Tau00*exp(-a0*((E-E0)/Tau00).^2);
X0=zeros(index);
X0=(E+i*Tau0)/E0;
e0 = zeros(index);
e0 = A*E0.^-1.5.*X0.^-2.*(2-(1+X0).^0.5-(1-X0).^0.5);

%Calculation of epsilone0E (exiton of E0)
```

```
e0E = zeros(1,index);

        for m=1:100,
            e0E = e0E + (Aex0./(m^3*(E0-(G3D0/m^2)-E-i*Tau0)));
        end

%Calculation of epsilone1 (other CPs)

Tau1 = zeros(3,index);
Tau1 = [Tau11(1)*exp(-a1(1)*((E-E1(1))/Tau11(1)).^2); Tau11(2)*exp(-a1(2)*((E-
E1(2))/Tau11(2)).^2); Tau11(3)*exp(-a1(3)*((E-E1(3))/Tau11(3)).^2)];
X1 = zeros(3,index);
X1 = [(E+i*Tau1(1,:))/E1(1);(E+i*Tau1(2,:))/E1(2);(E+i*Tau1(3,:))/E1(3)];

e1 = zeros(1,index);

        for m=1:3,
            e1 = e1 + (-B1(m)*X1(m,:).^-2.*log(1-X1(m,:).^2));
        end

%Calculation of epsilone1E (exiton of other CPs)

e1E = zeros(1,index);

        for p=1:3,
           for q=1:100,
            e1E = e1E + Bx1(p)./((2*q-1)^3*(E1(p)-(G2D1(p)/(2*q-1)^2)-E-i*Tau1(p,:)));
           end
        end


%Total dielectric constant

e = e0 + e0E + e1 + e1E + e_in;
%e = 2+i*zeros(1,index);
% ep1 = real(e);
% ep2 = imag(e);
n = zeros(0,index);
n = sqrt(e);
%n = sqrt((sqrt(real(e).^2+imag(e).^2)+real(e))/2);
K = zeros(0,index);
K = sqrt((sqrt(real(e).^2+imag(e).^2)-real(e))/2);
abcoeff = zeros(0,index);
abcoeff=4*pi*K./(l*1e-7);
```

```
Ref = zeros(0,index);
Ref = ((n-1).^2 + K.^2)./((n+1).^2 + K.^2);

plot(E,imag(e),E,abs(real(e))); % Plotting imaginary/real parts of the dielectric constant
plot(E,K);


% **********Transfer Matrix Method and Calculating UV Responsivity ***************

k = E/1.24/1e-4; % cm^-1

n0 = ones(1,index);
n1 = n;
n2 = n;
n3 = n;
n4=2.22724-0.00279*l+6.68807e-6*l.^2-7.65017e-9*l.^3+4.01177e-12*l.^4-7.70215e-
16*l.^5;
%n4 = ones(1,index);
n5 = ones(1,index);
d=[2.29e-4,0.6e-4,0.7e-4,500e-4,500e-4]; %cm
W = 1.5; %micron

        for t=1:index,

           x1=n0(t)/n1(t);
           x4=n3(t)/n4(t);

           T1 = 0.5*[1+(n0(t)/n1(t)),1-(n0(t)/n1(t));1-(n0(t)/n1(t)),1+(n0(t)/n1(t))];
           T2 = 0.5*[1+(n1(t)/n2(t)),1-(n1(t)/n2(t));1-(n1(t)/n2(t)),1+(n1(t)/n2(t))];
           T3 = 0.5*[1+(n2(t)/n3(t)),1-(n2(t)/n3(t));1-(n2(t)/n3(t)),1+(n2(t)/n3(t))];
           T4 = 0.5*[1+(n3(t)/n4(t)),1-(n3(t)/n4(t));1-(n3(t)/n4(t)),1+(n3(t)/n4(t))];
           T5 = 0.5*[1+(n4(t)/n5(t)),1-(n4(t)/n5(t));1-(n4(t)/n5(t)),1+(n4(t)/n5(t))];

           D1 = [exp(i*2*pi*k(t)*n1(t)*d(1)),0;0,exp(-i*2*pi*k(t)*n1(t)*d(1))];
           D2 = [exp(i*2*pi*k(t)*n2(t)*d(2)),0;0,exp(-i*2*pi*k(t)*n2(t)*d(2))];
           D3 = [exp(i*2*pi*k(t)*n3(t)*d(3)),0;0,exp(-i*2*pi*k(t)*n3(t)*d(3))];
           D4 = [exp(i*2*pi*k(t)*n4(t)*d(4)),0;0,exp(-i*2*pi*k(t)*n4(t)*d(4))];
           D5 = [exp(i*2*pi*k(t)*n5(t)*d(5)),0;0,exp(-i*2*pi*k(t)*n5(t)*d(5))];


           Q=T4*D3*T3*D2*T2*D1*T1;

           detQ=Q(1,1)*Q(1,2)-Q(2,1)*Q(2,2);
```

```
            R(t) = (abs(Q(2,1)/Q(2,2)))^2; % Calculating reflection
            T(t) = (abs(x1*x4/Q(2,2)))^2; % Calculating transmission

            RR(t) = Q(2,1)/Q(2,2);

        End

Abs = 1-R-T; % Calculating Absorption

        for t=1:index,

            T1 = 0.5*[1+(n0(t)/n1(t)),1-(n0(t)/n1(t));1-(n0(t)/n1(t)),1+(n0(t)/n1(t))];
            D1 = [exp(i*2*pi*k(t)*n1(t)*d(1)/2),0;0,exp(-i*2*pi*k(t)*n1(t)*d(1)/2)];

            QQ=D1*T1;
            EF0=[1.0;-RR(t)];
            EFF0(t)=1-RR(t);
            EF00(t)=abs(EF0(1)+EF0(2));
            Epm=QQ*EF0;
            Eout(t)=abs(Epm(1)+Epm(2));
            Res(t)=4*3.14*imag(e(t))*Eout(t)^2*W/1.24;
        end


plot(l,Abs); % Plotting  absorption
plot(l,Res); % Plotting  responsivity
```